OSAKA UNIVERSITY
DEPARTMENT OF EARTH AND SPACE SCINECE

Molecular Dynamics of Pressure-Induced Structural Transformations and Elastic Stability in Oxide Minerals.

Thesis submitted for the degree of
"Doctor of Philosophy"

CANDIDATE
Taku Tsuchiya

SUPERVISOR
Prof. Takamitsu Yamanaka

— January 2000 —

Index

Chapter 1

Introduction

1.1 Motivation

High-pressure structural transition of materials considered as components of the Earth is the most fundamental and important phenomenon to understand the bulk structure of the Earth. The idea that the observed gaps of seismological wave velocity result from the density changes of Earth's constituents with their pressure-induced transitions is widely accepted (Ringwood 1991). Based on this concept, a number of high-pressure experiments have been executed energetically to investigate thermodynamical phase relations of possible Earth's interiors and their analogue materials. The accumulation of this knowledge enables us to draw the entire picture of the Earth's static structure (see Appendix A).

Nowadays it is significantly important to understand the Earth's dynamics. Comparing seismological observations of mantle anisotropy with the measured or predicted anisotropy of candidate mantle minerals can elucidate the geometry of the Earth's mantle flow. The most precise and informative observations of the bulk of the Earth are from its elastic properties. The phase transition in the subducting slab affects on its rheology. Mechanical stability of homogeneous crystals has been a subject of understanding of their transition mechanisms. From these points of view, the elasticity of materials at high pressure and temperature is one of substantial physical and geological interests. M. Born initiated the systematic study of crystal stability under load, which is well known as Born's stability condition. Although a great number of experimental studies about

thermodynamical and elastic properties has been performed even for recent years (Upadhyay and Kumar 1995, Chopelas 1996, Shinogeikin and Bass 1999), the temperature and pressure ranges studied by these experiments have all been limited to narrow area near ambient condition by difficulties of technological aspects. Theoretical and computational investigations are very powerful tools for this research field. One of the most efficient simulation techniques for atomistic level structure and physical property is molecular dynamics (MD) method.

The first attempt to understand crystalline structures microscopically was made by V. M. Goldschmidt and a little later by L. Pauling before 1930's. They introduced a notion of the ionic radius (or crystal radius), which is nowadays still very useful for understanding and roughly predicts the structure of ionic crystals. It is, however, that only one parameter per one atom is insufficient to describe a variety of materials and their properties such as the elastic properties. Interatomic potentials were introduced from this viewpoint.

The idea that the structure of materials is determined by the interatomic potentials is still a highly simplified picture if compared with the full problem of solving the Schrödinger equations containing both nuclei and electrons. However, the interatomic potential is definitely an important starting point of microscopic treatment of material structures.

There are some levels of simplification for the interatomic potentials. The most simplified and common version is so-called effective pairwise potentials, which are made to depend only on the interatomic distance between two atoms. Many simple ionic crystals are known to be simulated rather well with pair potentials (Tosi 1964). The parameters contained in the potential function are usually determined empirically so that experimental results are reproduced (Fig. 1.1a). An obvious extension is to employ three-body interactions which depend on the bond angles among three atoms. This type of potential

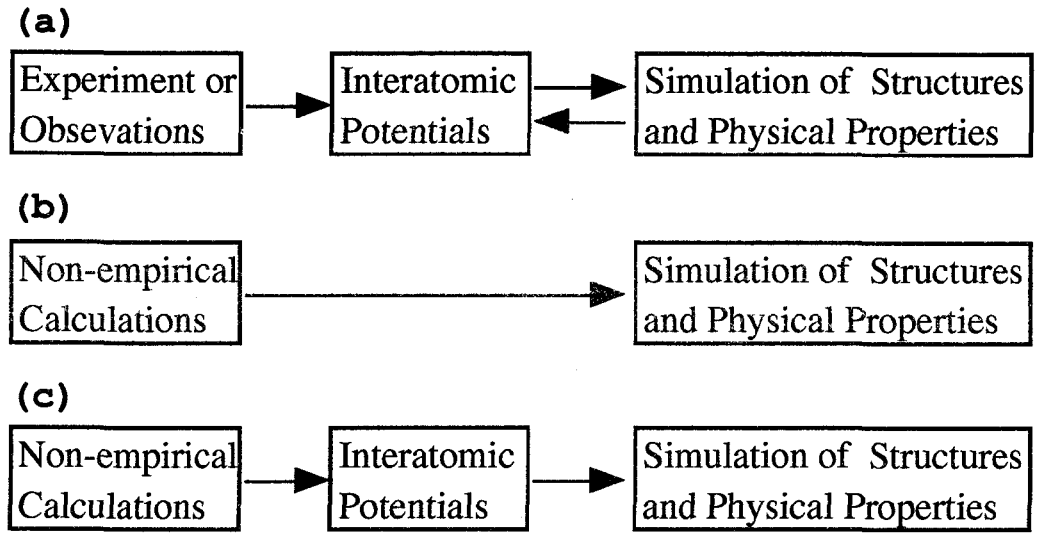

Figure 1.1 Three different procedures for the simulation of material structures and their physical properties.

is needed to simulate covalent materials such as pure silicon (Stillinger and Weber 1985; Biswas and Hamann 1987). If we further want to reproduce the phonon dispersion and elastic constant tensor very precisely, the many-body potentials are known to be necessary. One of them is the shell-model potentials, which take account of the distortion and polarization of electron distribution by floating ionic shells (Catlow et al. 1982). As the level of sophistication increases, the degree of freedom (the number of potential parameters) to specify the interatomic potentials is doomed to increase, so that we cannot expect from the interatomic potentials much ability to predict unknown properties of materials as far as we stick to empirical determination of potential parameters. Such inefficiency of interatomic potentials is partially due to the difficulty in deriving them from macroscopic information obtained by experiments.

The molecular dynamics (MD) technique is one of the efficient methods to simulate temperature and pressure behavior of physical properties of solid and melt. By empirical fitting to experimental results including crystal structures, dielectric and elastic properties and phonon dispersion, many of the effective interatomic potentials used in

such calculations have been determined. Although these empirical potentials have been applicable for ionic solids and melts, the reliability of the calculated results are limited by the selection of the interatomic potential functions and parameters. The application of simulation techniques for complex systems demands accurate knowledge of the interatomic interactions. Modeling dynamics as well as static properties of perfect and defective lattices severe requirements on the accuracy of the potentials and also derivatives. Nowadays it is possible to study the structure of materials using non-empirical electronic structure calculations (Fig 1.1b). There exist well-known examples of such an approach by M. L. Cohen and his co-workers (Yin and Cohen 1980; Cohen 1989 and references therin). Using density functional theory (DFT) (Hoenberg and Kohn 1964), they successfully obtained the most stable structure of crystalline silicon. In these studies, a certain atomic configuration is firstly assumed, the electronic structure is calculated non-empirically, the forces working on each atom at the position are derived, and then the atoms are moved to obtain the optimum configuration. The simulated annealing method (the so-called *ab initio* molecular dynamics method) developed by Car and Parrinello (1985) would give a more efficient approach along this line.

Although such a non-empirical approach would in principle be more desirable, there are many difficulties left as future problems. The most serious one is the huge amount of computational time and memories required for the calculation, which limit the number of atoms and electrons in the unit cell of the crystal. Thermal effects are also difficult to be taken into account. Such limitations are serious even for the simulation of such a common material as silica (SiO_2) which has many similarity to GeO_2 going to discuss in the thesis.

Two approaches to the simulation of atomic configurations have been mentioned; the simulation using empirical interatomic potentials and the simulation by no-empirical calculations of electronic structure. Although the latter has more predictability, so far it

is not feasible in many cases. The former approach has also been favored in using several kinds of simulation techniques such as the lattice dynamics or the molecular dynamics where empirical potentials are employed. However it is evidently more desirable to derive the non-empirical potentials which are then provided into the molecular dynamics.

From this point of view, in the present thesis, these two approaches to investigate the structural and elastic properties of complex crystals have been combined, that is, interatomic potentials were derived from the first-principles electronic structure calculation and applied to the molecular dynamics simulation of crystals (Fig. 1.1c). It is known that the crystal structure at absolute zero depends on the minimum condition of the total energy, and its elastic moduli depend on the second derivatives of the potential with respect to the structural parameters. Lassaga and Gibbs (1987), Tsuneyuki et al. (1988) and Kramer et al. (1991) determined parameters of interatomic potential from *ab initio* Hartree-Fock (HF) calculations using clusters such as H_4SiO_4. However, their potentials were derived from the calculation results of the cluster and it is not clear that the interatomic potential obtained from the cluster calculation can be applied to crystalline systems with sufficient accuracy. Allan and Mackrodt (1994) applied DFT and calculated the interatomic potential of the Mg^{2+} and O^{2-} pair. It, however, may also be less accurate when it is applied to crystalline systems, especially in the case of those having strong covalency. SiO_2 should be considered as a special case such that the cluster model seems to be valid because of the large rigidity of the SiO_4 tetrahedron. The bulk modulus of α-quartz calculated by Newton et al. (1980) agrees well with the experimental value in spite of assuming rigid regular SiO_4 tetrahedra in their calculations.

Gale et al. (1992) directly determined interatomic potentials for Al_2O_3 which were represented by the following Buckingham form,

$$\phi_{ij} = \frac{q_i q_j}{r_{ij}} + A_{ij} \exp(-r_{ij}/\rho_{ij}) - C_{ij} {r_{ij}}^{-6}, \qquad (1.1)$$

by fitting to the energy surface obtained from the periodic HF calculation. Their successful result indicates that interatomic potentials derived from HF level calculation are more accurate than empirically derived ones. It is suggested that in the ionic systems as this, dispersion forces play a minor role in determining crystal structure since the HF scheme does not include electron correlation differing from DFT. However, authors pointed out a lack of this model related to short-range attractive C parameters between cations. One can infer that unphysically large values of them are caused by the highly correlated nature of the parameters in the fixed functional form of potentials. Recently, Kamiya (1996) developed a more sophisticated model using multiple exponential terms for the non-Coulombic contribution in order to avoid the restriction from the fixed form of the potential function. He successfully reproduced the crystal structure, its bulk modulus and optic properties of MgO by the fitting procedure in a wide volume range. However, since his potential belongs to the two-body approximation, it cannot reproduce the deviation from the Cauchy relation and thus fails to estimate the shear elastic modulus correctly. In order to reproduce the elasticity and its pressure and temperature dependence correctly beyond limitations of pair potentials using an efficient and inexpensive way, new methods noted in the next chapter was applied in this study.

The materials chosen as a target of our simulation are MgO, CaO, GeO_2 and $MgGeO_3$, whose high-pressure transitions have physical, geophysical and mineralogical significance summarized as follows:

1. The cosmic abundance of nonvolatile elements is listed in Table II (Anders and Grevesse 1989). If it is assumed that the Earth accreted from nebula of a solar composition and takes the core composition to be roughly Fe, the composition of the terrestrial mantle can be estimated from these cosmic abundance as

shown in Table I. Since MgO (periclase) easily reacts with SiO_2 (silica), the dominant phases of the Earth's crust and mantle are magnesium silicate $MgSiO_3$ and Mg_2SiO_4. Considering that silica and periclase are as a basic module of the crystal structure of magnesium silicate, these oxides and silicates are most significant materials of the Earth. As well-known, GeO_2 (germania), CaO (lime) and $MgGeO_3$ (germanate) are also of importance as good analogue materials of structural and physical properties. However, few theoretical and computational studies of these materials have been carried out.

2. These oxides have long been of interest as typical cases for understanding bonding in ionic and covalent oxides. These are also one of most fundamental materials for industrial sciences. From the crystal chemical points of view, their structural and elastic properties and the structural transitions are quite interesting problems to confirm whether these are reproduced with common interatomic potentials. Mizushima et al. (1994) stated in their computational study of Si that mechanical instability gave the bound on the limit of stability of ideal crystal lattices. The relations between elasticity and transition are quite interesting themes for solid-state physics.

TABLE I Cosmic abundance of nonvolatile elements (relative to 1000 atoms of Si) (Anders and Grevesse 1989).

Mg	1074
Al	84.9
Si	1000
Ca	61.1
Ti	2.4
Fe	900

TABLE II Constitution of the model Earth (wt. %).

Crust+Mantle	
MgO	25.6%
SiO_2	38.5%
Core	
Fe	35.5%

1.2 Mechanical stability of lattices

According to thermodynamics, the low-pressure phase will coexist with the high-pressure phase at a pressure where the Gibbs free energy, $G = E + PV - TS = H - TS$, of the two structures are equal. It is well known that the equilibrium phase boundary is given by this definition. To estimate the thermodynamical transition pressure using MD method, free energy difference ΔG is approximately substituted ΔH for since MD method can not calculate entropy directly and roughly speaking, in typical oxide minerals at about room temperature, it can be thought that there is no significant difference between ΔH and ΔG. However macroscopic thermodynamics provides no information about mechanisms of the phase transition from the atomistic point of view. Mechanical stability of lattice is rather of importance for the crystal chemical and the crystallographic understanding of phase transitions. Dynamical theory of crystal lattices is described in detail in a textbook

written by M. Born and K. Huang (1954). For a lattice to be mechanically stable, the energy density must be a positive definite quadratic form so that the energy is raised by any small strains ϵ. For lattices, the variation given by the homogeneous deformation is equal directly to the strain-energy function

$$\frac{1}{2}\sum_{\rho\sigma} c_{\rho\sigma}\epsilon_\rho\epsilon_\sigma, \tag{1.2}$$

where $c_{\rho\sigma}$ is the corresponding elastic stiffness constants in the Voigt notation, defined as coefficients in a stress (σ)-strain (ϵ) linear response relation so-called Hook's law $c_{ij} = \partial\sigma_i/\partial\epsilon_j$. When we arrange the elastic constants in the form of a matrix,

$$\begin{pmatrix} c_{11} & c_{12} & c_{13} & c_{14} & c_{15} & c_{16} \\ c_{21} & c_{22} & c_{23} & c_{24} & c_{25} & c_{26} \\ c_{31} & c_{32} & c_{33} & c_{34} & c_{35} & c_{36} \\ c_{41} & c_{42} & c_{43} & c_{44} & c_{45} & c_{46} \\ c_{51} & c_{52} & c_{53} & c_{54} & c_{55} & c_{56} \\ c_{61} & c_{62} & c_{63} & c_{64} & c_{65} & c_{66} \end{pmatrix}, \tag{1.3}$$

then, (according to a well-known theorem in algebra,) the quadratic form of Eq. (1.2) is positive definite if the determinants of the matrices of successive orders as marked out above (the principle minors) are all positive. For a cubic lattice which has three independent elastic constants c_{11}, c_{12} and c_{44}, the principle minors are

$$c_{44},\ c_{44}^2,\ c_{44}^3,\ c_{11}c_{44}^3,\ (c_{11}^2 - c_{12}^2)c_{44}^3,\ (c_{11} - c_{12})^2(c_{11} + 2c_{12})c_{44}^3. \tag{1.4}$$

For these to be positive, only the three following conditions are need to be fulfilled:

$$c_{11} + 2c_{12} > 0,\ c_{44} > 0,\ c_{11} - c_{12} > 0, \tag{1.5}$$

which are connected to the bulk, shear and tetragonal moduli, respectively, and are referred to as spinodal, shear and Born criteria, respectively. By the same way, for a trigonal lattice belonging to point groups 32, $3m$ or $\bar{3}m$ which has six independent components c_{11}, c_{33}, c_{44}, c_{12}, c_{13} and c_{14} in the elastic tensor, the stability conditions are written as

follows,

$$c_{11} - |c_{12}| > 0,\ (c_{11} + c_{12})c_{33} - 2c_{13}^2 > 0,\ (c_{11} - c_{12})c_{44} - 2c_{14}^2 > 0. \qquad (1.6)$$

For a tetragonal lattice belonging to $4mm$, $\bar{4}2m$, 422 or $4/mmm$ which has six independent components c_{11}, c_{33}, c_{44}, c_{66}, c_{12} and c_{13}, the stability conditions are written as follows,

$$c_{11} - c_{12} > 0,\ c_{44} > 0,\ c_{66} > 0,\ (c_{11} + c_{12})c_{33} - 2c_{13}^2 > 0. \qquad (1.7)$$

If all conditions are fulfilled in each crystal class, the lattice is mechanically stable. These conditions are also valid under hydrostatic pressure if elastic constants are estimated in Eulerian coordinates. This exactly corresponds to applying strains to the cell after equilibration at definite T and P condition in the Hook's law. In the present thesis, the crystal stability under high-pressure is discussed by means of these conditions from the viewpoint of elasticity.

Some phase transitions that occurs when these stability conditions are broken on cooling have been observed: e.g. *sym*-triazine (hexagonal-monoclinic transition at 198 K, Dove et al. 1983) and HCN (tetragonal-orthorhombic transition at 170 K, Mackenzie and Pawley 1979). These phase transitions are called ferroelastic. However, only a few case which this concept can be applied is known in the pressure-induced structural transitions.

1.3 Historical survey of pressure-induced structural transitions of oxide minerals

MgO and CaO

As well known, MgO and CaO have the rock-salt (NaCl) structure (cubic symmetry, space group $Fm\bar{3}m$ and formula unit $z = 4$) at ambient condition. These phases are called the B1-type phase. It has been experimentally reported by Richet et al. (1988) that CaO was thermodynamically stable in the CsCl-type structure called the B2-type phase over 55 GPa at room temperature. On the other hand, the B2-type phase of MgO

has never observed experimentally in spite of a search over a quite high-pressure, 200 GPa. The elasticity of alkaline-earth metal oxides MgO and CaO at high pressure and temperature is of substantial physical and geological interest for several reasons. These oxides have long been of interest as a typical case for understanding bonding in ionic oxides and are also one of most fundamental materials for material sciences. MgO is particularly important as the end-member of a hypothesized major lower mantle phase, (Mg,Fe)O magnesiowüstite, because the most precise and informative observations of the bulk of the Earth are from its elastic properties. Comparing seismological observations of mantle anisotropy with the measured or predicted anisotropy of candidate mantle minerals can elucidate the geometry of the Earth's mantle flow. Although a great number of experimental and theoretical studies about thermodynamical and elastic properties of MgO have been performed even for recent years (Upadhyay and Kumar 1995, Chopelas 1996, Karki et al. 1997, Shinogeikin and Bass 1999), the temperature and pressure ranges studied by these experiments have all been limited to narrow area near ambient condition and the quantum mechanical method can be calculate only zero temperature (static) situation. Moreover there is no systematic comprehension including each elastic constant of these materials at high pressure and temperature considered to be extremely important.

The elasticity of solids yields the substantial insight into the nature of bonding. Especially, deviations from the following high-pressure Cauchy relation (Brazhkin and Lyapin 1997) of elastic moduli,

$$c_{12} - c_{44} - 2P = 0, \tag{1.8}$$

are a direct measure of the importance of noncentral forces in crystals (Grimsditch et al. 1986, Ercolessi et al. 1988) where P represents pressure value. Values of c_{44}/c_{12} ratio at ambient condition were reported as 1.6 (Sinogeikin and Bass 1999) and 1.3 (Oda et al. 1992) for MgO and CaO, respectively and decrease with increase atomic number. This

systematic change seems to relate the differences of bonding nature of these materials. The very recent high pressure measurement of the elasticity of MgO up to 18.6 GPa (Sinogeikin and Bass 1999) showed that the deviation increases with pressure in qualitative concordance with a theoretical study using the pseudopotential method (Karki et al. 1997), which could not include temperature effect.

Another interesting physical property about elasticity is the acoustic wave velocity and its temperature and pressure dependence. Sinogeikin and Bass (1999) reported that an anisotropy of the elastic wave of MgO decreases with pressure. Karki et al. (1997) reported that this anisotropy increased again after once it vanished. We will discuss a physical meaning of this behavior.

Recently Matsui (1998) investigated temperature and pressure dependence of elasticity of MgO and CaO using the breathing shell model with empirically determined potentials. Although the deviation from the Cauchy relation was reproduced successfully, this model significantly overestimated the compressibility of MgO at high-pressure. It may be considered that the empirical procedure and restriction of the too simple fixed form of potential function cause this failure.

GeO_2

GeO_2 has polymorphic relationships similar to the geologically important SiO_2. Two stable polymorphs of GeO_2 are experimentally known; one of them is the α-quartz-type structure (trigonal symmetry, $P3_221$, $z = 3$) which contains fourfold-coordinated germanium ions, and the other is the rutile-type structure (tetragonal symmetry, $P4_2/mnm$, $z = 2$) which contains sixfold-coordinated germanium ions. Phase-equilibrium studies of GeO_2 polymorphs (Hill and Chang 1968, Akaogi et al. 1993) show that the rutile-type structure is stable under ambient conditions (see Appendix B). Although the stable region is over 1280 K, the quartz-type polymorph can exist at ambient condition. In the

quartz-type structure, the GeO_4 tetrahedra, linked to each other by sharing the corner oxygen ions, construct the three-dimensional framework. In general, a compressibility mechanism of the framework structure can approximately be explained by cooperative tilting of tetrahedra (Hazen and Finger 1982). This concept was supported by high pressure experimental results for SiO_2 and GeO_2 (Jorgensen 1978; Yamanaka and Ogata 1991) and an *ab initio* molecular orbital calculation for the $H_6Si_2O_7$ molecule (Newton et al. 1980). The bulk modulus of α-quartz calculated by Newton et al. (1980) agrees well with the experimental value in spite of assuming rigid regular SiO_4 tetrahedra in their calculations. However under more compression, the distortion of tetrahedra comes to be negligible. It was reported that oxygen atoms tended to arrange themselves in body-centered cubic (bcc) sublattice (Sowa 1988) or in closest packed layer parallel to (1 $\bar{2}$ 0) (Hazen et al. 1989). The amorphization of the quartz-type structures is likely to be plastic lattice deformation (Yamanaka et al. 1997).

In general, crystalline states have higher density than amorphous states, like quenched glasses from their melts. It is often observed experimentally that low-density glasses transforms to crystal forms under high pressure by modes of crystallization. However many materials that crystalline states transform to denser amorphous states have been discovered under their compression processes. A group of α-quartz and its related structures is one of the famous examples of pressure-induced amorphization transition. Hemley et al. (1988) reported the pressure-induced amorphization of SiO_2, α-quartz, and α-cristbalite at about 22 GPa. Yamanaka et al. (1992), Wolf et al. (1992), and Kawasaki et al. (1994) reported that the amorphization pressure of quartz-type GeO_2 was 6.5–7 GPa at room temperature by both of X-ray diffraction and spectroscopic measurements. Itie et al. (1989) and Kawasaki (1996) investigated the pressure-induced amorphization of quartz-type GeO_2 by the extended X-ray absorption fine structure (EXAFS) method and reported an increase of the coordination number of cations with amorphization. This in-

crease of the cation coordination is the most remarkable property of the pressure-induced amorphization; because of this structural change, differing from rapid cooled glass, the pressure-induced amorphous state has a higher density than the low pressure crystalline state.

Kingma et al. (1993) reported in their electron and optical microscopy study of amorphous SiO_2 quenched from high pressure that mixed phases of amorphous and crystalline lamellae existed, and proposed that nonhydrostatic stresses played an important role in the amorphization process. Gillet et al. (1995) showed in their experimental study on the high-pressure behavior of α-$AlPO_4$ that the stresses were of a fundamental importance in the crystal-to-amorphous phase transition of this material. Moreover, Wolf et al. (1992) observed the small rutile-type structured cluster (crystallite) in the amorphous GeO_2 by means of the electron microscope and implied that the quartz-to-rutile transformation could occur microscopically even under the thermally underactive room temperature. However the mechanism of the quartz-to-rutile or the amorphous-to-rutile transition have never become clear.

Comprehension of the mechanisms of the amorphization processes is an important and interesting theme from not only crystal chemical but also of glassy industrial points of view. However, experimental results of amorphization mechanisms under pressure are limited because the amorphous phase is a macroscopically disordered state. Atomic level computer simulation techniques can be very important complementary to experiments. Especially, molecular dynamics (MD) calculation method can provide much significant information for the atomistic structural property and the dynamical mechanism of the transition.

Previous theoretical studies of α-quartz by Tse and Klug (1991) and Binggeli et al. (1994) proposed that the amorphization transition of α-quartz under high pressure, together with the inhibition of thermal activation, resulted from a mechanical instability

of the crystal lattice. Tse and Klug stated that the relevant instability was the bulk instability, but Binggeli et al. contradictorily reported that the shear instability caused the transition. Chaplot and Sikka (1993) and Watson and Parker (1995) calculated by quasi-harmonic lattice dynamical calculations that a zone-boundary phonon softening occurred prior to the amorphization transition, and concluded that shear stresses may make an important contribution to the instabilization of the quartz structure. Badro et al. (1996), moreover, reported in their MD study of α-quartz that the mean transition pressure could be effectively lowered under uniaxial nonhydrostatic conditions, and structural changes under shear stressed conditions are also interesting.

Although studies of the origin of amorphization in quartz-type GeO_2 and the amorphous structure attract great interest because of their isostructural relation with silica, no MD simulation of GeO_2 polymorphs has ever been studied for their dynamic and atomistic implication in high-pressure transformations. In this study, we investigated that pressure-induced structural changes of quartz-type GeO_2 under hydrostatic and nonhydrostatic compression in more detail. We report structural properties of the high-pressure state, especially the mechanism of increased coordination number at transition to amorphization and an abrupt collapse in volume of the quartz-type structure at 7.4 GPa. Moreover, effects of shear stress to the amorphization, and a new prediction of a possible quartz-to-rutile phase transition mechanism under nonhydrostatic conditions are reported. This transition may be related to the result of the electron microscope observation of pressure-induced amorphous GeO_2 by Wolf et al. (1992).

In general, based on systematics of AX_2-type compounds, it has been believed that rutile structure may directly transform into an eightfold-coordinated fluorite structure as found in some fluoride. Many experimental attempts have been made to find a further high pressure polymorph of GeO_2. The crystal structure of a post-rutile phase has attracted a great deal of interest. A few types of structure have been proposed as a possible structure

from high pressure experiments. Hexagonal Fe_2N-type GeO_2 was synthesized above 1000 °C and 25 GPa using static compression (Liu et al. 1978). A certain orthorhombic crystal was reported at 1000 °C and 28 GPa (Ming and Manghnani 1983). The in situ X-ray diffraction experiment (Tsuchida and Yagi 1989) and theoretical calculations (Cohen 1992; Matsui and Tsuneyuki 1992) reported a transition of SiO_2 stishovite to $CaCl_2$-type phase. A pressure-induced rutile-to-$CaCl_2$ transition of GeO_2 was predicted by Tsuchiya et al. (1998) by MD calculations. Furthermore, by recent in-situ Raman spectroscopic measurements of SiO_2 and GeO_2 by Kingma et al. (1995) and Haines et al. (1998), respectively, it was found that the B_{1g} optic phonon mode of the rutile-type phase softened up to the transition pressure and then became a hard A_g mode of $CaCl_2$-type phase.

$MgGeO_3$

$MgGeO_3$ has similar polymorphic relationships to the geologically extremely important $MgSiO_3$ which is a hypothetical major component of the Earth's mantle (see Appendix B). Four polymorphs of $MgGeO_3$ have been known from previous experimental studies. The two pyroxene-type polymorphs, namely high-pressure-clinoenstatite-type (monoclinic, space group $C2/c$) and the orthoenstatite-type (orthorhombic, $Pbca$) phase, are low-pressure polymorphs. Ozima and Akimoto (1983) stated that the clino-type form is stable at higher pressure and lower temperature than ortho-type form, in their study of high pressure and temperature experiment. Yamanaka et al. (1985) studied detail crystal structures of the clino- and the ortho-type form of $MgGeO_3$ by the single-crystal x-ray diffraction technique and noted that the $C2/c$ and the $Pbca$ structure contained a crystarographically unique corner-linked tetrahedra chain and two type chains, respectively. In the $C2/c$ high-pressure-clinoenstatite-type structure, germanium and magnesium ions sit in $8f$ and $4e$ site in the Wyckoff notation, respectively. Oxygen anion occupies at $8f$ site. As the same as the general pyroxene-type structure, oxygen ions are arranged

into the distorted cubic-closed-packed (ccp) state, and fourfold- and sixfold-coordination cation sites in the ccp oxygen lattice are occupied by germanium and magnesium ions, respectively. High-pressure-clinoenstatite-type $MgGeO_3$ has attention since it was reported that unquenchable high density clinoenstatite of $MgSiO_3$ might also have the same structure (Angel et al. 1992).

The ilmenite-type (rhombohedral, $R\bar{3}$) and the $LiNbO_3$-type (rhombohedral, $R3c$) phase are high-pressure polymorphs of $MgGeO_3$, in which structures both magnesium and germanium ions are surrounded by six oxygen ions. The ilmenite-type structure was investigated by Kirfel et al. (1978). The oxygen ions configuration in this structure is the almost complete hexagonal-close packing (hcp). Ito and Matsui (1979) found a rhombohedral phase of $MgGeO_3$ which was 1.8 % denser than the ilmenite-type phase. Later this phase was assigned the lithium niobate structure (Lienenweber et al. 1994). This structure also contains octahedral-coordinated magnesium and germanium cations. Difference between the ilmenite-type and the $LiNbO_3$-type structure is only the way of cation distribution. The MgO_6 and GeO_6 octahedra layers which are normal to c axis are found in the ilmenite-type structure whereas the Mg octahedron and the Ge octahedron locate alternately in the (001) plane of the $LiNbO_3$ structure.

According to an *in-situ* high-pressure X-ray observation using a diamond-anvil-cell (DAC) (Nagai et al. 1995), high-pressure-clino-type $MgGeO_3$ transformed to a high-pressure phase at ca. 23 GPa under room temperature. The diffraction pattern of the high pressure phase showed that the product after the transition had a different structure from the ilmenite-type and the $LiNbO_3$-type structure. The crystal structure has never been analyzed experimentally because of significant broadening of diffraction peaks after the transition.

Chapter 2

Methods of calculation

2.1 Molecular dynamics

2.1.1 Periodic boundary conditions

When using periodic boundary conditions (PBC), particles are enclosed in a box, and this box is replicated to infinity by rigid translation in all the three Cartesian directions, completely filling the space. If one of our particles is located at position $\mathbf{r}$ in the box, we assume that this particle really represents an infinite set of particles located at

$$\mathbf{r} + \ell\mathbf{a} + m\mathbf{b} + n\mathbf{c} \ , \ (\ell, m, n = -\infty, \infty), \tag{2.1}$$

where ℓ, m, n are integer numbers, and $\mathbf{a}, \mathbf{b}, \mathbf{c}$ are the vectors corresponding to the edges of the box. All these "image" particles move together, and in fact only one of them is represented in calculations. Apparently, the number of interacting pairs increases enormously as an effect of PBC. By the minimum image criterion, this complexity is reduced to the minimum level. It is supposed that when separated by a distance equal or larger than a cutoff distance R_c, two particles do not interact with each other. It is also supposed that an MD basic box whose size is larger than $2R_c$ along each Cartesian direction is chosen. When these conditions are satisfied, it is obvious that it at most one among all the pairs formed by a particle i in the box and the set of all the periodic images of another particle j will interact.

2.1.2 The Velret time integration algorithm

In molecular dynamics, the Verlet algorithm (Verlet 1967) is used as time integration algorithm. The basic idea is to write two third-order Taylor expansions for the positions $\mathbf{r}(t)$, one forward and one backward in time:

$$\begin{aligned} \mathbf{r}(t+\Delta t) &= \mathbf{r}(t) + \mathbf{v}(t)\Delta t + (1/2)\mathbf{a}(t)\Delta t^2 + (1/6)\mathbf{b}(t)\Delta t^3 + O(\Delta t^4), \\ \mathbf{r}(t-\Delta t) &= \mathbf{r}(t) - \mathbf{v}(t)\Delta t + (1/2)\mathbf{a}(t)\Delta t^2 - (1/6)\mathbf{b}(t)\Delta t^3 + O(\Delta t^4), \end{aligned} \quad (2.2)$$

where $\mathbf{v}$, $\mathbf{a}$ and $\mathbf{b}$ are the velocities, the accelerations, and the third derivatives of $\mathbf{r}$ with respect to t, respectively. Adding the two expressions gives

$$\mathbf{r}(t+\Delta t) = 2\mathbf{r}(t) - \mathbf{r}(t-\Delta t) + \mathbf{a}(t)\Delta t^2 + O(\Delta t^4). \quad (2.3)$$

This is the basic form of the Verlet algorithm. Since we are integrating Newton's equations, $\mathbf{a}(t)$ is just the force divided by the mass, and the force is in turn a function of the positions $\mathbf{r}(t)$:

$$\mathbf{a}(t) = -(1/m)\nabla V\left(\mathbf{r}(t)\right). \quad (2.4)$$

This algorithm is simple to implement, accurate and stable, explaining its large popularity among molecular dynamics simulators. The velocities are computed from the positions by using

$$\mathbf{v}(t) = \frac{\mathbf{r}(t+\Delta t) - \mathbf{r}(t-\Delta t)}{2\Delta t}. \quad (2.5)$$

An even better implementation of the same basic algorithm is the velocity Verlet scheme, where positions, velocities and accelerations at time $t + \Delta t$ are obtained from the same quantities at time t in the following way;

$$\begin{aligned} \mathbf{r}(t+\Delta t) &= \mathbf{r}(t) + \mathbf{v}(t)\Delta t + (1/2)\mathbf{a}(t)\Delta t^2, \\ \mathbf{v}(t+\Delta t/2) &= \mathbf{v}(t) + (1/2)\mathbf{a}(t)\Delta t, \end{aligned}$$

$$\begin{aligned} \mathbf{a}(t+\Delta t) &= -(1/m)\nabla V\left(\mathbf{r}(t+\Delta t)\right), \\ \mathbf{v}(t+\Delta t) &= \mathbf{v}(t+\Delta t/2) + (1/2)\mathbf{a}(t+\Delta t)\Delta t. \end{aligned} \tag{2.6}$$

2.1.3 Temperature

The average potential energy V is obtained by averaging its instantaneous value, which is usually obtained straightforwardly at the same time as the force computation is made. For instance, in the case of two-body interactions,

$$V(t) = \sum_{i}^{N} \sum_{j>i}^{N} \phi\left(|\mathbf{r}_i(t) - \mathbf{r}_j(t)|\right), \tag{2.7}$$

where N is the number of particles. Using the instantaneous particle velocity, the instantaneous kinetic energy is given by

$$K(t) = \frac{1}{2} \sum_{i}^{N} m_i [v_i(t)]^2. \tag{2.8}$$

The instantaneous temperature $T(t)$ is directly related to the kinetic energy by the well-known equipartition formula, assigning an kinetic energy $k_B T/2$ per degree of freedom:

$$K(t) = \frac{3}{2} N k_B T(t). \tag{2.9}$$

An estimate of the average temperature is obtained by averaging its instantaneous value.

2.1.4 Pressure

The measurement of the pressure in a molecular dynamics simulation is based on the Clausius virial function

$$W(\mathbf{r}_1, \ldots, \mathbf{r}_N) = \sum_{i=1}^{N} \mathbf{r}_i \cdot \mathbf{F}_i^{\mathrm{TOT}}, \tag{2.10}$$

where $\mathbf{F}_i^{\mathrm{TOT}}$ is the total force acting on atom i. Its statistical average $\langle W \rangle$ will be obtained, as an average over the molecular dynamics trajectory:

$$\langle W \rangle = \lim_{t \to \infty} \frac{1}{t} \int_0^t d\tau \sum_{i=1}^{N} \mathbf{r}_i(\tau) \cdot m_i \ddot{\mathbf{r}}_i(\tau), \tag{2.11}$$

where use has been made of Newton's law. By integrating by parts,

$$\langle W \rangle = -\lim_{t\to\infty} \frac{1}{t} \int_0^t d\tau \sum_{i=1}^{N} m_i |\dot{\mathbf{r}}_i(\tau)|^2. \tag{2.12}$$

This is twice of the average kinetic energy, therefore by the equipartition law of statistical mechanics,

$$\langle W \rangle = -DNk_BT, \tag{2.13}$$

where D, N and k_B are the dimensionality of the system (2 or 3), the number of particles, and the Boltzmann constant, respectively.

The total force acting on a particle as composed of two contributions:

$$\mathbf{F}_i^{\mathrm{TOT}} = \mathbf{F}_i + \mathbf{F}_i^{\mathrm{EXT}}, \tag{2.14}$$

where $\mathbf{F}_i$ is the internal force (arising from the interatomic interactions), and $\mathbf{F}_i^{\mathrm{EXT}}$ is the external force exerted by the container's walls. If the particles are enclosed in a parallelepiped container of sides L_x, L_y, L_z, volume $V = LxLyLz$, and with the coordinates origin on one of its corners, the part $\langle W^{\mathrm{EXT}} \rangle$ due to the container can be evaluated using the definition (2.10):

$$\langle W^{\mathrm{EXT}} \rangle = L_x(-PL_yL_z) + L_y(-PL_xL_z) + L_z(-PL_xL_y) = -DPV, \tag{2.15}$$

where $-PLyLz$ is, for instance, the external force F_x^{EXT} applied by the yz wall along the x directions to particles located at $x = Lx$, etc. Eq. (2.13) can then be written as

$$\left\langle \sum_{i=1}^{N} \mathbf{r}_i \cdot \mathbf{F}_i \right\rangle - DPV = -DNk_BT \tag{2.16}$$

or

$$PV = Nk_BT + \frac{1}{D} \left\langle \sum_{i=1}^{N} \mathbf{r}_i \cdot \mathbf{F}_i \right\rangle. \tag{2.17}$$

This result is known as the virial equation. All the quantities except the pressure P are easily accessible in a simulation, and therefore Eq. (2.17) constitutes a way to measure P.

In the case of pairwise interactions via a potential $\phi(r)$, Eq. (2.17) becomes

$$PV = Nk_BT - \frac{1}{D}\left\langle \sum_i \sum_{j>i} r_{ij} \left.\frac{d\phi}{dr}\right|_{r_{ij}} \right\rangle . \tag{2.18}$$

This expression has the additional advantage over Eq. (2.17) to be naturally suited to be used when periodic boundary conditions are present: it is sufficient to take them into account in the definition of r_{ij}.

Parrinello and Rahman (1980, 1981) developed a variant where the shape of the parallelepiped box can vary as well as the volume. This is achieved by introducing h-matrix having nine new degrees of freedom instead of one: the components of the three vectors spanning the MD basic cell. Each of them is a new dynamical variable, evolving accordingly to equation of motion derived from an appropriate Lagrangian. This scheme allows to simulate the constant enthalpy-isobaric ensemble (NHP) and to study structural phase transitions as a function of pressure. And the $\alpha\beta$ component of pressure tensor is consequently noted as follows,

$$P_{\alpha\beta} = V^{-1}\left[\sum_i m_i v_{i\alpha} v_{i\beta} + \left\langle \sum_i \sum_{j>i} (F_{ij}/r_{ij}) r_{ij\alpha} r_{ij\beta} \right\rangle\right] . \tag{2.19}$$

Another very important ensemble is the canonical ensemble (NVT). In a method developed by Nosé (1984) and Hoover (1985), this is achieved by introducing a time-dependent frictional term, whose time evolution is driven by the imbalance between the instantaneous kinetic energy and the average kinetic energy $(3N/2)k_BT$. These methods are generally called the extended Lagrangian method. By combining these methods, the most practical isothermal-isobaric ensemble (NTP) can be simulated. In the MD calculations in the present thesis, for controls of temperature and pressure, the scaling algorithm which is a simplified version of these extended Lagrangian methods is employed.

2.1.5 Running coordination number

One of most practical ways to analyze the local structure from the calculated particle distribution is the so-called running coordination number $N_{ij}(r)$ which is the coordination number as a function of distance. This function is calculated as follows,

$$N_{ij}(r_m) = \frac{1}{N_i} \sum_{n=1}^{m} n_{ij}(r_n), \tag{2.20}$$

where N_i and $n_{ij}(r_n)$ are the number of particles of i species and the number of the particle pairs of i and j species existing in the spherical shell centered at particles i and having the radius $r_n - \Delta r/2 < r_n < r_n + \Delta r/2$.

2.1.6 QEq method

Standard approaches to interatomic potentials for minerals and oxides use fixed charges, three-body potentials or valence terms, which may not be appropriate for describing phase transitions, where the coordination environment and structure may change dramatically. Electrostatics plays an essential role in determining the structure and properties of minerals. Since the charges may depend on the distances, angles and coordination environment, it should be considered that the charge must be allowed to readjust to the instantaneous geometric configuration of the atoms.

The electrostatic energy E_{es} of a set of interacting atoms with charges q_i is given by the sum of the atomic energies E_i, and the electrostatic interaction between all pairs of atoms $J_{ij}(r_{ij}; q_i, q_j)$,

$$E_{\mathrm{es}} = \sum_i E_i(q_i) + \sum_i \sum_{j>i} J_{ij}(r_{ij}; q_i, q_j). \tag{2.21}$$

The local atomic energy E_i can be expressed approximately to second order as $E_i(q_i) = E_i(0) + \chi_i^0 q_i + 1/2 J_{ii}^0 q_i^2$ (Mortier et al. 1986, Rappé and Goddard 1991). Here, the expansion coefficients χ_i^0 and J_{ii}^0 correspond physically to the electronegativity and hardness

of the isolated atom, and are obtained from valence-averaged atomic ionization potential (IP) and electron affinity (EA) as $\chi_i^0 = (\mathrm{IP}_i + \mathrm{EA}_i)/2$ and $J_{ii}^0 = (\mathrm{IP}_i - \mathrm{EA}_i)$. Applying this expression of the atomic energy, the electrostatic energy is written as

$$E_{\mathrm{es}} = E_0 + \sum_i q_i \chi_i + \sum_i \sum_{j \geq i} q_i q_j J_{ij}(r_{ij}). \tag{2.22}$$

Based on the electronegativity equalization principle (Sanderson. 1951), it is required that the electronegativity χ_i of each atom must be equal on all ions in equilibrium state. This principle was explained from the density functional viewpoint and applied to the classical system (Parr et al. 1978). From the definition that $\chi_i \equiv \partial E_{\mathrm{es}}/\partial q_i$, χ_i is described as a function of the charges on all of atoms in the system containing N atoms,

$$\chi_i(q_1, q_2, \cdots, q_N) = \chi_i^0 + \sum_j J_{ij}(r_{ij}) q_j. \tag{2.23}$$

Rappeé and Goddard took $J_{ij}(r_{ij})$ to be the Coulomb integral between Slater orbitals centered on each atomic site,

$$J_{ij}(r_{ij}) = \int d\mathbf{r}_i d\mathbf{r}_j |\phi_{n_i}(\mathbf{r}_i)|^2 \frac{1}{|\mathbf{r}_i - \mathbf{r}_j - \mathbf{r}_{ij}|} |\phi_{n_j}(\mathbf{r}_j)|^2. \tag{2.24}$$

Here, ϕ is the Slater $1s$-like orbital given by

$$\phi_{n_i}(\mathbf{r}) = A_i r^{n_i - 1} e^{-\zeta_i r}. \tag{2.25}$$

and is characterized by a principal quantum number n_i and an exponent ζ_i. This function has the asymptotic behavior as

$$J_{ij}(r) = \begin{cases} 1/r & \text{as } r \to \infty \\ J^0 & \text{as } r \to 0 \end{cases}. \tag{2.26}$$

Thus, J_{ij} describes simple Coulomb for large separations, but it is shielded for short distances. In the present study, to save calculational time, this shielded Coulomb interaction was simplified by the function having the same asymptotic behavior,

$$J_{ij}(r_{ij}) = \frac{\tanh(\zeta_{ij} r_{ij})}{r_{ij}} \tag{2.27}$$

and ζ_{ij} related to the shielding distance was represented by $\left[1/(2J_{ii}^0) + 1/(2J_{jj}^0)\right]^{-1}$.

N first-order equations with respect to the charges q_i are derived from the electronegativity equalization condition $\chi_1 = \chi_2 = \cdots \chi_N$, and the total charge neutrality condition $\sum_i q_i = 0$. The charges are determined by solving the equations set. This algebraic procedure is equivalent to the electrostatic energy minimization with respect to the charges subject to the constraint of the total charge neutrality condition. Since the average electronegativity can be related to the chemical potential of valence electron system μ_i as $\chi_i = -\mu_i$, the electronegativity equalization condition corresponds to the chemical potential equalization condition. The way to calculate the effective charges of ions and their fluctuation using this procedure is called the charge-equilibration (QEq) method by Rappé and Goddard. MD calculations using the QEq method (QEq-MD) were recently executed by Rick et al. (1994) and Demiralp et al. (1999). This method is a functional many-body potential approach in the ionic approximation. In QEq-MD, as the atomic charges were renewed at each calculation step, the interatomic potential can respond to changes of environment (P, T, atomic configuration, etc.). Therefore the deviation from the Cauchy relation in cubic systems can be successfully reproduced by this method. In this study, the original QEq-MD code has been written and is applied for monoxides. To extend for periodic system, Ewald method (Ewald 1921) was applied. The simultaneous equation was solved by the LU decomposition.

However, using this procedure to estimate charges, computational time increases in proportion to N^3 order to solve the equations set. This difficulty prevents from applying QEq method to larger particle systems. As one of more sophisticated techniques, a dynamical model using the extended Lagrangian method should be developed (see Appendix C).

2.2 Ab initio calculation

2.2.1 LMTO

In FP-LMTO method, electronic states are described by linear-muffin-tin-orbitals (LMTO). The crystal space is partitioned into muffin-tin-spheres (MTS) centered at every atomic position and the interstitial region, which is named for the region outside the MTS. Here, the overlap of MTS's is not considered. In the interstitial region, the electronic state is described by the Hankel functions, which are the solutions of the Helmholtz's equation:

$$(-\Delta - \epsilon) f(\mathbf{r}) = 0, \tag{2.28}$$

in which the region is set at atomic position $\mathbf{R} + \mathbf{t}$, where $\mathbf{R}$ is the position of the atom in the unit cell and $\mathbf{t}$ is the translation vector. The Hankel functions are taken with some fixed energy $\epsilon = \kappa^2$. Inside the MTS, the radial part of the electronic state is described by the linear combination of $\phi_{RL}(\mathbf{r}_R - \mathbf{t}, \epsilon_{\kappa Rl})$ and its energy derivative $\dot{\phi}_{RL}(\mathbf{r}_R - \mathbf{t}, \epsilon_{\kappa Rl})$, where ϕ is the solution of the one-electron Schrödinger (or Dirac) equation inside MTS with the spherically symmetric part of the potential for the energy $\epsilon_{\kappa Rl}$ which is taken with the center of interest, L denotes the combined index for lm, and $\mathbf{r}_R = \mathbf{r} - \mathbf{R}$. The coefficients of the linear combination are determined with the condition of smooth augmentation to the Hankel function, $K_{\kappa L}(\mathbf{r}_R - \mathbf{t})$, at the boundary of MTS centered at $\mathbf{R} + \mathbf{t}$. Inside any other MTS centered at $\mathbf{R}' + \mathbf{t}'$, the electronic states are also described by linear combination of ϕ and $\dot{\phi}$, and the coefficients are determined as follows. The tail of the Hankel function is expanded in terms of Bessel functions, which are also the solutions of Eq. (2.28):

$$K_{\kappa L}(\mathbf{r}_R - \mathbf{t}) = \sum_{L'} J_{\kappa L}(\mathbf{r}_R - \mathbf{t}) S_{R'L',RL}(\mathbf{t}' - \mathbf{t}, \kappa), \tag{2.29}$$

where $S_{R'L',RL}$ is the structure constants in direct space. The coefficients of ϕ and $\dot{\phi}$ centered at $\mathbf{R}' + \mathbf{t}'$ are determined with the condition of smooth augmentation to the each

Bessel functions in Eq. (2.29). Here, the following definitions are used:

$$K_{\kappa l}(r) = -\frac{i(\kappa\omega)^{l+1}}{(2l-1)!!}h_l(\kappa r), \tag{2.30}$$

$$J_{\kappa l}(r) = \frac{1}{2}\frac{(2l-1)!!}{(\kappa\omega)^l}j_l(\kappa r), \tag{2.31}$$

where $h_l = j_l - in_l$ are the spherical Hankel functions and j_l, n_l are the spherical Bessel and Neumann functions, respectively, and ω is the MTS radius. The phase factor of spherical harmonics Y_L to be used is defined after Condon and Shortley (1951), and $f_L \equiv i^l Y_L f_l$, where f is K, J, ϕ, $\dot{\phi}$ and so on. The expression for the structure constant is

$$S_{R'L',RL}(\mathbf{t},\kappa) = \sum_{L''}\frac{8\pi(2l''-1)!!}{(2l'-1)!!(2l-1)!!}C^{L''}_{LL'}(\kappa\omega)^l(\kappa\omega')^{l'}(\kappa\omega'')^{-l''} \times K_{\kappa l''}(|\mathbf{t}-\mathbf{R}'+\mathbf{R}|)(-i)^{l''}Y^*_{L''}(\mathbf{t}-\hat{\mathbf{R}}'+\mathbf{R}), \tag{2.32}$$

where $C^{L''}_{LL'}$ is Gaunt coefficients:

$$C^{L''}_{LL'} = \int d\hat{\mathbf{r}}Y_L(\hat{\mathbf{r}})Y^*_{L'}(\hat{\mathbf{r}})Y_{L''}(\hat{\mathbf{r}}). \tag{2.33}$$

The last step is to perform the Bloch sum of the LMTO's centered at different sites, and finally obtained as in the form

$$\chi^{\mathbf{k}}_{\kappa RL}(\mathbf{r}) = \Phi^K_{\kappa RL}(\mathbf{r}_R)\delta_{RR'} + \sum_{L'}\Phi^J_{\kappa R'L'}(\mathbf{r}_{R'})S^{\mathbf{k}}_{R'L',RL}(\kappa) \quad \text{for } |\mathbf{r}-\mathbf{R}'| < s_{R'} \tag{2.34}$$

$$= \sum_{\mathbf{t}} e^{i\mathbf{kt}}K_{\kappa L}(\mathbf{r}_R - \mathbf{t}) \quad \text{for } \mathbf{r} \text{ at the interstitial region} \tag{2.35}$$

where s_R is the MTS radius for the atom included in the sublattice 'R' and

$$S^{\mathbf{k}}_{R'L',RL}(\kappa) = \sum_{\mathbf{t}\neq 0} e^{i\mathbf{kt}}S_{R'L',RL}(\mathbf{t},\kappa). \tag{2.36}$$

The functions $\Phi^K_{\kappa RL}(\mathbf{r}_R)$ and $\Phi^J_{\kappa RL}(\mathbf{r}_R)$ are the linear combination of ϕ_{RL} and $\dot{\phi}_{RL}$, in which the functions match smoothly to Hankel and Bessel functions at the MTS boundary respectively as described above.

In the present calculations, lattice Fourier transformation is performed to get the numerical values of the Hankel functions in the interstitial region. To improve the

convergence with respect to the number of reciprocal lattice vectors, the solution of the following equation is used instead of the Hankel function $K_{\kappa L}(\mathbf{r})$:

$$(-\Delta-\kappa^2)f(\mathbf{r}) = \frac{4\pi\left(\frac{\xi^2}{\pi}\right)^{\frac{3}{2}}(2\xi^2)^l\omega^{l+1}e^{\kappa^2/(2\xi)^2}}{(2l-1)!!}r^l e^{-(\xi r)^2}i^l Y_L(\hat{\mathbf{r}}), \tag{2.37}$$

where the Gaussian damping parameter is defined by the following relation,

$$\frac{(\omega\xi_l^2)^{l+2}e^{-(\omega\xi_l^2)^2}}{(G_{cut}/2\xi_l^2)^l e^{-(G_{cut}/2\xi_l^2)^2}} = \text{const.} \tag{2.38}$$

In Eq. (2.38), the right hand side is set as 0.5 in the present work and G_{cut} is the absolute value of maximum reciprocal lattice vector to be used, which is defined by numerical and computational conditions.

2.2.2 Hamiltonian and overlap matrix

With the LMTO basis set defined in Eq. (2.34) and (2.35), the wave functions $\psi_{\mathbf{k}\lambda}(\mathbf{r})$ for valence electrons, where λ denotes the bands, are represented as linear combinations of LMTO's with the coefficients $A^{\mathbf{k}\lambda}_{\kappa RL}$ obtained from the variational principle. For the one-electron Hamiltonian given by LDA, they are found from the generalized eigenvalue problem:

$$\begin{aligned}&\sum_{\kappa RL}\left[<\chi^{\mathbf{k}}_{\kappa'R'L'}|-\Delta+V^{MT}(\mathbf{r})+V^{NMT}(\mathbf{r})|\chi^{\mathbf{k}}_{\kappa RL}> -\epsilon_{bfk\lambda}<\chi^{\mathbf{k}}_{\kappa'R'L'}|\chi^{\mathbf{k}}_{\kappa RL}>\right]A^{\mathbf{k}\lambda}_{\kappa RL}\\ \equiv\ &\sum_{\kappa RL}(H^{\mathbf{k}}_{\kappa'R'L',\kappa RL}-\epsilon_{\mathbf{k}\lambda}O^{\mathbf{k}}_{\kappa'R'L',\kappa RL})A^{\mathbf{k}\lambda}_{\kappa RL}=0,\end{aligned} \tag{2.39}$$

where $V^{MT}(\mathbf{r})$ and $V^{NMT}(\mathbf{r})$ stand for the spherical and the nonspherical parts of potential, respectively.

2.2.3 Density and potential

The valence density is calculated as follows:

$$n^v(\mathbf{r}) = 2\sum_{\mathbf{k}\lambda}\sum_{\kappa RL}\sum_{\kappa'R'L'}A^{\mathbf{k}\lambda*}_{\kappa'R'L'}A^{\mathbf{k}\lambda}_{\kappa RL}\chi^{\mathbf{k}*}_{\kappa'R'L'}(\mathbf{r})\chi^{\mathbf{k}}_{\kappa RL}(\mathbf{r}). \tag{2.40}$$

The electronic density inside MTS is expressed as

$$\hat{n}_R(\mathbf{r}) = \sum_L \hat{n}_{RL}(r) i^l Y_L(\hat{\mathbf{r}}), \tag{2.41}$$

where the core electron density is included in $L = 0$ term. The electronic density in the interstitial region is expressed as

$$\tilde{n} = \sum_{\mathbf{G}} \tilde{n}(\mathbf{G}) e^{i\mathbf{G}\cdot\mathbf{r}}. \tag{2.42}$$

The Hartree potential is calculated by solving Poisson's equation for the total charge density ρ. The auxiliary charge Γ is introduced to compensate the multipole moments of charge densities in MTS under the following condition:

$$\int_0^{s_R} \left[\hat{n}_{LR} + \sqrt{4\pi} n_R^N(r)\delta_{l,0} - \Gamma_{RL}(r)\right] r^{l+2} dr = 0, \tag{2.43}$$

where $n_R^N(r)$ denotes the nuclear charge density. If Eq. (2.43) is fulfilled, the densities inside MTS can not produce an electrostatic field outside its own sphere. The influence of the charges in the given MTS on the rest of the crystal is completely described by the field produced by the Γ, which is added to the ρ to be canceled out. Poisson's equation for $\tilde{n} + \Gamma$ is solved by Fourier transformation. The auxiliary density Γ must be localized inside MTS and be smooth enough to ensure a fast convergence of the Fourier series. The Gaussian type auxiliary density is used in the present calculations,

$$\Gamma_{RL}(\mathbf{r}) = d_{RL} r^l e^{-(\xi_{RL} r)^2} i^l Y_L(\hat{\mathbf{r}}), \tag{2.44}$$

where the damping constant ξ is also defined by Eq. (2.38) with the following condition:

$$G_{cut}^{\text{orbit.}} \leq G_{cut}^{\text{dens.}}, \tag{2.45}$$

and the coefficient d_{RL} is defined by the condition Eq. (2.43).

The Hartree potential in MTS is written as

$$\hat{V}^H(\mathbf{r}) = \sum_L \hat{V}_{RL}^H(r) i^l Y_L(\hat{\mathbf{r}}), \tag{2.46}$$

where

$$\begin{aligned}\hat{V}^H_{RL}(r) &= \frac{8\pi}{2l+1}\left[\frac{1}{r^{l+1}}\int_0^r x^{l+2}\hat{\rho}_{RL}(x)dx\right. \\ &\quad +r^l\int_r^{s_R} x^{1-l}\hat{\rho}_{RL}(x)dx \\ &\quad \left.+r^l\sum_{\mathbf{G}} 4\pi Y^*_L(\hat{\mathbf{G}})G\,{-1}s_R^{1-l}j_{l-1}(Gs_R)[\tilde{n}(\mathbf{G})+\Gamma(\mathbf{G})]\right] \qquad (2.47)\end{aligned}$$

and

$$\hat{\rho}_{RL}(x) = \hat{n}_{RL}(r) + \sqrt{4\pi}n^N_R(r)\delta_{l,0}. \qquad (2.48)$$

In the interstitial region,

$$\tilde{V}^H(\mathbf{r}) = \sum_{\mathbf{G}}\frac{8\pi}{G^2}[\tilde{n}(\mathbf{G})+\Gamma(\mathbf{G})]e^{i\mathbf{G}\cdot\mathbf{r}}. \qquad (2.49)$$

In MTS, the exchange-correlation potential within LDA is written as

$$\hat{v}^{xc}(\mathbf{r}) = \sum_L \hat{v}^{xc}_{RL}(r)Y_L(\hat{\mathbf{r}}). \qquad (2.50)$$

For $r > 0.03Z^{1/3}a_0$, where Z is the atomic number and a_0 is Bohr radius, the numerical integration is performed to obtain the L component:

$$\hat{v}^{xc}_{RL}(r) = \int d\hat{\mathbf{r}}v^{xc}[\hat{n}_R(\mathbf{r})]\left(i^lY_L(\hat{\mathbf{r}})\right)^*. \qquad (2.51)$$

For $r \leq 0.03Z^{1/3}a_0$, a Taylor expansion is performed: the spherical (MT) part of the density is taken as a large part and the non-spherical (NMT) part as a small part:

$$\begin{aligned}\hat{v}^{xc}_{RL=0}(r)/\sqrt{4\pi} &= v^{xc}[n^{MT}(r)] + \frac{1}{4\pi}\frac{1}{2}v^{xc\prime\prime}[n^{MT}(r)]\sum_{L'>0}(\hat{n}_{RL'}(r))^2, \\ \hat{v}^{xc}_{RL>0}(r) &= v^{xc\prime}[n^{MT}(r)]\hat{n}_{RL}(r) + \frac{1}{2}\sum_{L',L''>0} v^{xc\prime\prime}[n^{MT}(r)]\hat{n}_{RL'}(r)\hat{n}_{RL''}(r)C^{L''}_{LL'},\end{aligned} \qquad (2.52)$$

where $v^{xc\prime}$ and $v^{xc\prime\prime}$ are the first and second derivative of v^{xc} with respect to the density.

In the interstitial region, the exchange-correlation potential is represented as a Fourier sum. The coefficients are determined via a three-dimensional numerical integration over the unit cell:

$$\tilde{v}^{xc}(\mathbf{G}) = \frac{1}{\Omega_{cell}}\int d\mathbf{r}v^{xc}[\tilde{n}(\mathbf{r})]e^{-i\mathbf{G}\cdot\mathbf{r}}. \qquad (2.53)$$

2.2.4 Total energy

The total energy is divided into following parts:

$$E_{\rm tot} = E_{\rm kin} + E_{\rm H} + E_{\rm xc}. \tag{2.54}$$

The kinetic energy part is written as

$$\begin{aligned} E_{\rm kin} &= \sum_{\mathbf{k}\lambda} f_{\mathbf{k}\lambda}\epsilon_{\mathbf{k}\lambda} + \sum_{iR} f_{iR}\epsilon_{iR} \\ &- \sum_{R}\int_{\rm MTS} d\mathbf{r}\hat{\rho}_R(\mathbf{r})\hat{V}_R(\mathbf{r}) - \sum_{\mathbf{G}}\tilde{n}^*(\mathbf{G})\sum_{\mathbf{G}'}\tilde{V}(\mathbf{G}')\int_{\rm INT} d\mathbf{r}e^{i(\mathbf{G}'-\mathbf{G})\cdot\mathbf{r}}, \end{aligned} \tag{2.55}$$

where $f_{\mathbf{k}\lambda}$ is the weight of $\mathbf{k}$-points sampling and f_{iR} is an occupation number for i-th core level, ϵ_{iR}.

Coulomb energy part is written as

$$\begin{aligned} E_{\rm H} &= \frac{1}{2}\sum_{R}\int_{\rm MTS} d\mathbf{r}\hat{\rho}_R(\mathbf{r})\hat{V}_R^H(r) \\ &+\frac{1}{2}\sum_{\mathbf{G}}\tilde{n}^*(\mathbf{G})\sum_{\mathbf{G}'}\tilde{V}^H(\mathbf{G}')\int_{\rm INT} d\mathbf{r}e^{i(\mathbf{G}'-\mathbf{G})\cdot\mathbf{r}}. \end{aligned} \tag{2.56}$$

For $r > 0.03Z^{1/3}a_0$ and in the interstitial region, the exchange-correlation energy is calculated in usual procedures. For $r \leq 0.03Z^{1/3}a_0$, this energy is evaluated by the Taylor expansion up to the second order.

2.3 Determination of interatomic potentials

2.3.1 Ab initio energy surfaces

Nowadays one of most sophisticated way simulating static behavior of materials in solid-state physics is density functional theory (DFT). Dependence of the total energy of two alkaline earth oxides on cell parameters and atomic positions were obtained by the following technique on the basis of DFT within the local density approximation (LDA) (Kohn and Sham 1965). The gradient corrected (GC) exchange-correlation potential (Perdew et al. 1996) was adopted. The *ab initio* full-potential linear muffin-tin-orbital (FP-LMTO) method (Weyrich 1988) and a multiple-κ MTO basis set (Methfessel et al. 1989) were adopted, where κ^2 is the kinetic energy of the envelope function. Three-κ for valence electrons were used: $\kappa^2 = -0.1$, -1.0 and -2.5 Ry were used for $2s$, $2p$ and $3d$ states for Mg and O, $3s$, $3p$ and $3d$ states for Ca, respectively. The core states were recalculated at each self-consistent iteration with relativistic effects.

Densities, potentials and the envelope functions inside the muffin-tin spheres (MTS) were expanded up to $l = 8$. Densities and potentials at the interstitial region were expanded in the Fourier series with the reciprocal lattice vectors **G**. About 14600 **G** and 12100 vectors for MgO and CaO were used, respectively. The envelope functions at the interstitial region were also expanded in **G**: s, p and d states were expanded in about 300, 600 and 1000 **G** vectors for both MgO and CaO. The tetrahedron method improved by Blöchl et al. (1994) were used for k points sampling. In the irreducible Brillouin zone, 16 k points were used. All of these parameters were settled for the total energy convergence within 0.5 mRy per atom and for charge density within 1.0×10^{-5} e/a.u.^{3}. Throughout all FP-LMTO calculations in this study, the MTS radii were settled in 1.7653 and 1.6346 for Mg and O in MgO, 2.2721 and 1.7278 a.u. for Ca and O atoms in CaO, respectively.

First, the total energies of alkaline earth oxide crystals with the rock-salt (B1)

structure were calculated with various cell parameters with the cubic symmetry. Next, the total energy variations were calculated in terms of cation displacements and lattice deformations with respect to typical cases of long wave-length limits of the optic (as shown in Fig. 2.1) and acoustic phonons (ϵ_1, ϵ_4) in the frozen phonon approximation, respectively. The cell deformations are considerably important to model elastic properties because the responses to them can be related to elastic constants and bulk sound velocities. Kamiya (1996) quite largely underestimated the B1-B2 (CsCl) transition pressure of MgO. This failure may be caused by no information about the cell deformations included in the parameterization procedure.

Multiple exponential functions were employed for interatomic potentials of the non-Coulombic contribution part between i-th and j-th ions following Kamiya (1996).

$$\varphi_{ij}(r_{ij}) = \sum_l A_{ij,l} \exp(-r_{ij}/\rho_{ij,l}), \tag{2.57}$$

where $A_{ij,l}$ and $\rho_{ij,l}$ are specific parameters for each ion pair. This representation of the

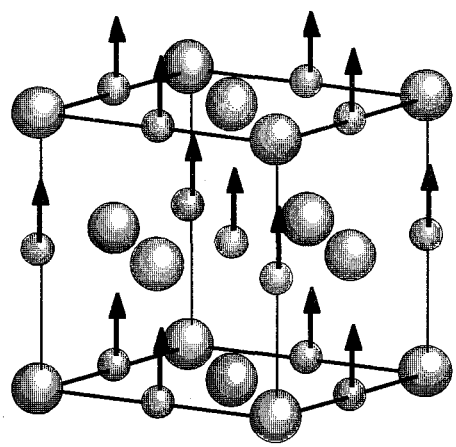

Fig.2.1 The calculated atomic displacement pattern for constructing potential energy surfaces of the B1 structure. The *large* and *small spheres* indicate anions and cations, respectively. This pattern corresponds to a typical displacement of optic phonons.

repulsion term corresponds to an expansion to a series of exponential functions and in a special case that $l = 1$, this term is equivalent to the repulsive part of Eq. (1.1). Because of flexibility by multiple terms from the restriction by the fixed functional form, *ab initio* potential surfaces can be precisely reproduced in the wide volume range. If a sufficiently large number of exponentials are included in Eq. (2.57), $\rho_{ij,l}$s can be fixed. Using these representations of the potential function, total lattice energy of a crystal U_{m} is described as a summation of the intra-atomic QEq energy and the interatomic energy,

$$U_{\mathrm{m}} = \sum_i \chi_i^0 q_i + \frac{1}{2} \sum_{i,j} \left(J_{ij} q_i q_j + \varphi_{ij}(r_{ij}) \right). \tag{2.58}$$

χ_i^0 and J_{ii}^0 are specific parameters for each atom and β_{ij} and r_{ij}^0 are ones for each ion pair. These parameters are determined by a least squares fitting procedure to the total energy calculated by the *ab-initio* method (U_{a}) by minimizing the following optimization function W.

$$W = \sum_s w_s (U_{\mathrm{a}}(s) - U_{\mathrm{m}}(s))^2, \tag{2.59}$$

where w_s is a weight factor and index s indicates a structure. Although a lot of parameter must be determined comparing to the simple form of Eq. (1.1), this never raise serious difficulty because the repulsive part comes to be a linear optimization problem by fixed $\rho_{ij,l}$. In this study, $\rho_{ij,l}$s were set to $1/0.75(1+l)$ $(l = 1, \cdots, n)$, where n was the number of terms included in Eq. (2.57). Dependence of n on convergence was examined and it was found that $n = 5$ was enough to obtain satisfied results as shown in the following section. At the beginning of the fitting procedure, χ_i^0 and J_{ii}^0 were assumed to the values calculated by Perdew et al. (1992) using the DFT method with GC. In this procedure, no repulsive interaction between magnesium cations was included since the ionic size of magnesium was small in comparison with other ions and then it can be regarded that their interaction was negligible. The optimized parameter are listed in Table III and IV. Fig. 2.2 for MgO and Fig. 2.3 for CaO show energy surfaces of FP-LMTO with variation

of volume, normal (ϵ_1), shear (ϵ_4) deformations and atomic displacement (u) with fitted results of the model potential function represented by Eq. (2.58).

TABLE III Optimized QEq parameters for MgO and CaO. Unit of the values is given in eV.

atom	χ^0 eV	J^0 eV
O	19.459	23.347
Mg	1.667	12.780
Ca	1.124	12.017

TABLE IV Optimized repulsive parameters $A_{ij,l}$ in Eq. (2.57) of each atom pair. Unit of the values is given in kJ/mol.

atom pair	$l=1$	2	3	4	5
O-O	-3.84852×10^2	9.04233×10^3	-2.20293×10^5	2.03867×10^6	-4.80861×10^6
Mg-O	1.17346×10^4	-2.11399×10^5	1.31867×10^6	-3.69644×10^6	4.02780×10^6
Ca-O	1.33794×10^3	-1.53944×10^4	4.83265×10^4	-9.52680×10^3	1.50253×10^5
Ca-Ca	4.87585×10^3	-2.67395×10^5	4.19283×10^6	-2.64784×10^7	5.92496×10^7

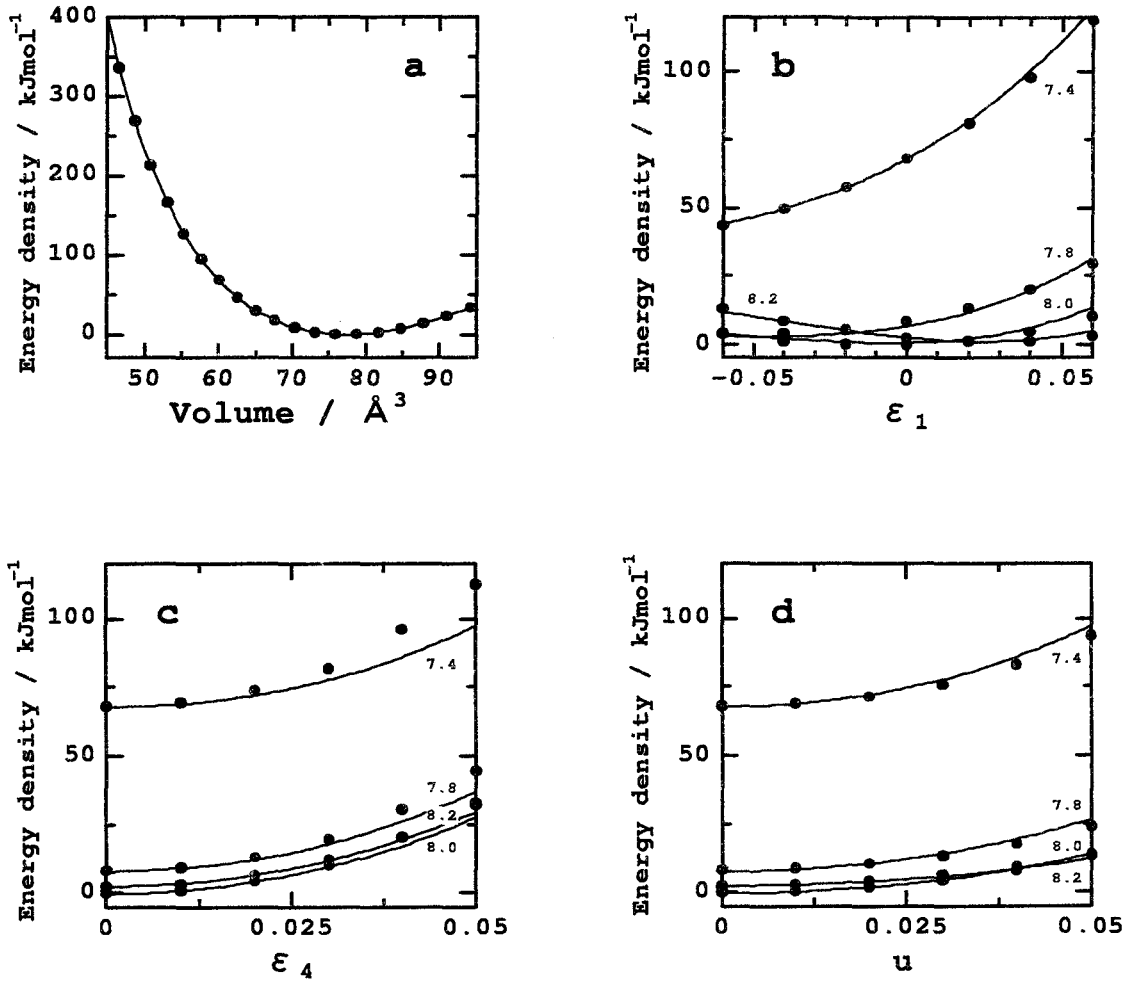

Figure 2.2 The optimized results of potential parameters to *ab initio* energy surfaces of MgO. The energy variation as a function of volume (**a**), strain ϵ_1 (**b**), ϵ_4 (**c**) and atomic displacement u (**d**). The *filled circles* are the calculated values of FP-LMTO and the *curves* are fitted results. The numbers in **b-d** are cell parameters at zero strains given in unit a.u.

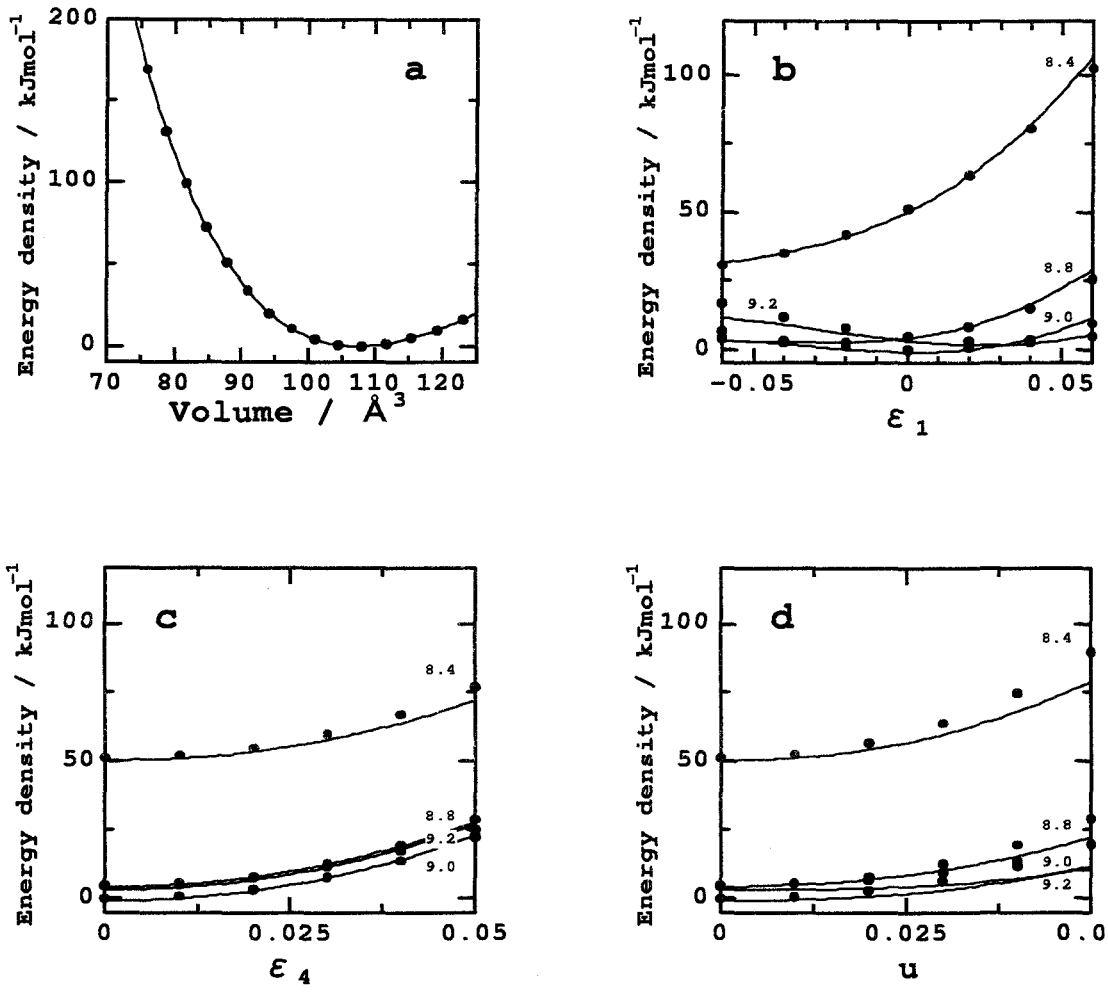

Figure 2.3 The optimized results of potential parameters to *ab initio* energy surfaces of CaO. The energy variation as a function of volume (**a**), strain ϵ_1 (**b**), ϵ_4 (**c**) and atomic displacement u (**d**). The *filled circles* are the calculated values of FP-LMTO and the *curves* are fitted results. The numbers in **b**-**d** are cell parameters at zero strains given in unit a.u.

2.3.2 Empirical techniques

MD calculation using the *ab initio* potential can give reliable results. In the present thesis, the interatomic potentials of GeO_2 and $MgGeO_3$ were, however, constructed by empirical ways written in this section owing to the limitation that *ab initio* calculations of these complicated structures still has computational difficulty. The functional form of the interatomic potentials employed in this study is expressed by Eq. (2.60) as a conventional Born-Mayer type partially ionic pairwise interaction model,

$$V_{ij}(r_{ij}) = \frac{q_i q_j}{r_{ij}} + f(B_i + B_j)\exp\left[\frac{A_i + A_j - r_{ij}}{B_i + B_j}\right] - \frac{C_i C_j}{{r_{ij}}^6}, \qquad (2.60)$$

where the terms represent Coulomb, van der Waals (Mayer 1933) and Gilbert-type repulsion (Gilbert 1968) energy, respectively. The term r_{ij} is the interatomic distance between i-th and j-th ion, f is a standard force constant 4.184 kJ/mol. The effective charge q, the repulsive radius A, the softness parameter B and the van der Waals coefficient C are the energy parameters. These parameters were empirically optimized to reproduce the crystal structures, bulk moduli and thermal expansivities of GeO_2 and $MgGeO_3$ polymorphs. The potential parameters used in the present study are listed in Table V for GeO_2 and Table VI for $MgGeO_3$ polymorphs. The static lattice energy minimization (WMIN) method (Busing and Matsui 1984) was applied to optimize the energy parameters from the observed crystal structure by minimizing the static total lattice energy expressed as $U_L(r_{ij}) = \sum_i \sum_{j>i} V(r_{ij})$. For GeO_2, a relation $q_{Ge} = 2q_O$ was assumed to conserve the total charge neutrality. The oxide GeO_2 has approximately similar structural and physical properties as SiO_2. The interatomic force between the germanium and the oxygen ion may be similar to that between the silicon and the oxygen ion. When starting to fit these parameters, each parameter was, therefore, referred to a SiO_2 potential model (TTAM) proposed by Tsuneyuki et al. (1988), which was derived from the *ab initio* Hartree-Fock calculations. For $MgGeO_3$, a relation $q_{Ge} + q_{Mg} = 3q_O$ was assumed to conserve the total

TABLE V Potential parameters for GeO_2 polymorphs.

atom	q / |e|	A / Å	B / Å	C / $Å^3 kJ^{1/2} mol^{-1/2}$
Ge	2.0	0.8680	0.034	47.876
O	−1.0	2.0330	0.172	144.243

TABLE VI Potential parameters for $MgGeO_3$ polymorphs.

atom	q / |e|	A / Å	B / Å	C / $Å^3 kJ^{1/2} mol^{-1/2}$
O	−1.298	1.7936	0.14	54.01
Ge	2.329	0.8603	0.04	–
Mg	1.565	0.8820	0.04	–

charge neutrality. Moreover the van der Waals coefficient C is applied only for oxygen.

2.4 Computational details in MD calculation

MD calculations were carried out in the isothermal-isobaric (NTP) condition to estimate pressure and temperature dependence of volume and investigate pressure-induced transitions. The scaling algorithms of particle velocities and basic cell parameters (Matsui and Kawamura 1987) were adopted to retain constant temperature T and pressure P (actually constant stress), respectively. To reproduce bulk situation, the three-dimensional periodic boundary condition was imposed. Here the Ewald sum method (Ewald 1921) was imposed with 230 reciprocal lattice vectors to converge the calculation of the Coulomb interaction efficiently. Newton's equation of motion was integrated numerically by Verlet algorithm with setting a time interval to 2.0 fs. To include the quantum contribution to the structural and thermodynamic properties, quantum corrections developed by Matsui (1989) were included. For MgO and CaO, ionic charges recalculated at every step using QEq method were treated as one of variables such as positions in the dynamical system.

An MD basic cell with 64 unit cells ($4\mathbf{a_1} \times 4\mathbf{a_2} \times 4\mathbf{a_3}$, containing 256 cations and 256 oxygen anions) was taken for MgO and CaO. MD basic cells with 100 unit cells (5a × 5a × 4c, containing 300 germanium and 600 oxygen ions) and 150 unit cells (5a × 5a × 6c, containing 300 germanium and 600 oxygen ions) were taken for quartz and rutile-type GeO_2. For $MgGeO_3$ polymorphs, MD basic cells with 16 unit cells ($2\mathbf{a} \times 2\mathbf{a} \times 4\mathbf{c}$, containing 128 magnesium, 128 germanium and 384 oxygen ions) for the clinopyroxene-type structure, with 8 ($1\mathbf{a} \times 2\mathbf{a} \times 4\mathbf{c}$, containing 128 magnesium, 128 germanium and 384 oxygen ions) for the orthopyroxene-type and 32 ($4\mathbf{a} \times 4\mathbf{a} \times 2\mathbf{c}$, containing 192 magnesium, 192 germanium and 576 oxygen ions) for both of the ilmenite-type and the $LiNbO_3$-type were taken. It was confirmed that these cell sizes gave no size effect to calculated results. In each run, the execution with a sufficiently long period of 3×10^3 steps (6 ps), reached an equilibrium state of the system under the desired P and T condition. After this procedure, in the typical case, the further subsequent period of 1×10^4 steps (20 ps) was carried out and the average of this data were regarded as calculated results.

The adiabatic elastic stiffness constants c_{ij} were calculated on the basis of the so-called Hook's law $\sigma_i = c_{ij}\epsilon_j$, which is a stress-strain linear response relation. In this procedure, a corresponding positive and negative strain of $\epsilon = \pm 0.01$ were given to equilibrated cells in the constant-cell adiabatic (NVE) condition after equilibration at each pressure and temperature. Shear modulus G is evaluated by the so-called Voigt-Reuss-Hill average, $G = 1/2(G_{\mathrm{V}} + G_{\mathrm{R}})$ where G_{V} and G_{R} are the Voigt average and the Reuss average, respectively.

2.5 Reproduction at ambient condition

Firstly, the calculated results of cell parameters, elastic moduli and thermal expansivities of MgO and CaO at ambient pressure are listed in Table VII with corresponding experimental results. The calculated lattice constants agree quite well with observed ones

within the deviations of 1.4%. The calculated bulk moduli and shear moduli also agree within the deviations of 8%, where bulk moduli and their derivatives were estimated by fourth-order least-square fits of calculated volume to the Birch-Murnaghan equation of state and shear moduli and their pressure derivatives were evaluated by second-order polynomial fits. The calculated elastic constants agree within 11%. The calculated thermal expansivities agree within 11%. These results indicate that the *ab initio* calculations are significantly plausible and the obtained energy surfaces have enough accuracy to applied to construct model effective potentials. Moreover, the new calculation method used in the present thesis can reproduce not only crystal structure but also several physical properties quite accurately. Especially, the deviations from the Cauchy relation evaluated by Eq. (1.8) are successfully reproduced. According to the experimental result of the resonance method by Oda et al. (1992), the thermal expansivity of CaO is smaller than that of MgO in spite of its larger compressibility. It intuitively seems curious since in oxides having the same crystal structure, the harder material generally has smaller thermal expansivity and vice versa. It is unlikely that CaO has a large region of negative thermal expansion at quite low temperatures as well as predictions about Si and AlAs by Pavone (1991). A very recent high-temperature X-ray diffraction measurement by Fiquet et al. (1999) gives a larger thermal expansion coefficient value of CaO. The present result is in concordance with the latter result.

The flexibility of the multiple exponential terms (Eq. (2.57)) enables to reproduce the volume compressibility of MgO under the very wide pressure range from ambient to 230 GPa. In fact, several previous calculations using empirical potentials could never reproduce the compression curve accurately at very high pressure because the functional form was too simple. Although the empirical optimization of a lot of potential parameters is a laborious task, using *ab initio* energy surfaces, little difficulty is needed to determine them and more accurate potentials can be constructed.

The simulated structural parameters for two structures of GeO_2, at ambient conditions, are given in Table VIII together with the observed values. No symmetrical constraints are applied on six lattice constants or the atomic position in MD simulation. Crystal symmetries solely depend on the nature of the interatomic potential model. There are, nevertheless, no significant differences between simulated values and experimental values. All the calculated cell parameters are in extremely good agreement with those observed for quartz- and rutile-type. In particular the differences in quartz-type cell parameters between experimental and calculated values are within 0.005 Å. The Ge-O interatomic distances, the O-Ge-O and the Ge-O-Ge bonding angles can also be reproduced fairly well. The largest error is that one of two Ge-O distances is subtly underestimated or that the Ge-O-Ge angle is overestimated by $\sim 4°$ in quartz-type. It is noted that this ionic interatomic potential can passably reproduce the Ge-O bond in quartz, including not a little covalency. Bulk moduli and their derivatives were estimated by third-order least-square fits of calculated volume to the Birch-Murnaghan equation of state. The calculated bulk moduli and thermal expansivities also agree considerably well with the experimental values. The calculated elastic constants of the quartz-type structure at ambient condition agree on the whole with the experimental results recently reported by Grimsditch et al. (1998). These results indicate that the c/a axial ratio of quartz-type increases with pressure, namely the crystal is stiffer in the c direction in spite that $c/a > 1$. This result is in agreement with experimental results (Glinnemann et al. 1992; Kawasaki et al. 1994). However, there are somewhat large errors between calculated and observed values of rutile-type GeO_2 although the trend of the variation of the c/a ratio as a function of pressure is correctly reproduced. The calculated enthalpies, expressed by $H = U_{pot} + U_{kin} + PV$, where U_{pot} and U_{kin} are the total potential energy and the kinetic energy given by time averages of values in Eq. (2.7) and Eq. (2.8), respectively, are also listed in Table VIII. The experimental energetical relation is correctly

reproduced.

MD calculations of four $MgGeO_3$ polymorphs, which have the high-pressure-clinoenstatite, the orthoenstatite, the ilmenite and the $LiNbO_3$-type phase, were carried out. The calculated results (lattice constants, densities ρ, bulk moduli K_0, their pressure derivatives K_0' and thermal expansivities α) at 0.1 MPa and 300 K are shown in Table IX with previous experimental observed values for comparison. The calculated densities of each polymorph at ambient condition agree quite well with experimental data and the largest discrepancy is only 0.07 g/cm^3 underestimation for the $LiNbO_3$-type phase. Bulk moduli and their derivatives were estimated by third-order least-square fits of calculated volume to the Birch-Murnaghan equation of state. The calculated K_0' values tends to be somewhat overestimated for three polymorphs. The calculated thermal expansivities are somewhat larger than observed ones and the largest discrepancy is 22% for the high-pressure-clino-type phase. No experimental data about the elastic and the thermodynamic properties of the $LiNbO_3$-type phase have ever reported in experimental studies. The bulk modulus and the thermal expansivity of the $LiNbO_3$-type phase are predicted somewhat larger and smaller than those of the ilmenite-type phase are, respectively. This result seems to be reasonable since the $LiNbO_3$-type phase is high-pressure phase of the ilmenite-type phase. In spite that the form of the interatomic potential is fairly simple, it had a high ability to reproduce all of four polymorphs transferably and then the calculated results using this interatomic potential are very convincing.

The significance of the $LiNbO_3$-type phase is that it implies the possible existence of a perovskite-type phase of $MgGeO_3$. Leinenweber et al. (1994) reported first in their in situ x-ray diffraction study, that an unquenchable perovskite-type polymorph was observed at 17.9 GPa. The calculation of perovskite-type $MgGeO_3$ was carried out using observed cell data by Leinenweber et al. and reported atomic positions in Mg-perovskite as the initial structural parameters of MD calculation. The perovskite-type structure was

preserved even at 0 GPa and the $LiNbO_3$-perovskite transition did not appear. Although the quenchable character differs from the experimental result, this result strongly suggests that the perovskite-form is likely to be stable even for $MgGeO_3$. The calculated structure data are also shown in Table IX.

2.6 Summary

- Methods of calculations and computational procedures are reported in detail. The newly developed QEq-MD method and the traditional empirical MD method successfully reproduce the several crystal structures at ambient condition.

- By QEq-MD with the interatomic potentials derived from first-principle calculations, the elastic properties of MgO and CaO including the deviations from the Cauchy relation are quite accurately reproduced, in spite that the potentials are determined with no optimization to experimentally observed data.

- By the traditional MD method with empirical pair potentials, the number of polymorphs of GeO_2 and $MgGeO_3$ are reproduced in spite of simplicity of the model potentials.

TABLE VII Calculated and observed structural and physical properties of B1 structured MgO and CaO. The cell parameters a, the bulk moduli K, shear moduli G and the thermal expansivities α at ambient condition are indicated. Observed cell lengths are from Fiquet et al. (1999). Observed bulk moduli and their derivatives are from MgO: Duffy et al. (1995); CaO: Richet et al. (1988). Observed shear moduli, their derivatives and elastic constants are from MgO: Sinogeikin and Bass (1999); CaO: Oda et al. (1992). Observed α are from the first array: Fiquet et al. (1999); the second array of MgO: Isaak et al. (1989); CaO: Oda et al. (1992).

Material	MgO		CaO	
Space group	$Fm\bar{3}m$		$Fm\bar{3}m$	
	Obs	QEq-MD	Obs	QEq-MD
Cell length				
a / Å	4.210	4.268	4.813	4.774
Bulk modulus				
K_0 / GPa	157	159.9	111	118.0
K_0'	4.3	3.5	4.2	4.7
K_0'	−0.022	−0.003	–	−0.060
Shear modulus				
G_0 / GPa	130.2	122.9	81.2	83.9
G_0'	2.4	1.8	–	1.7
G_0''	−0.04	−0.012	–	−0.016
Elastic constant				
c_{11} / GPa	297.9	296.0	219.2	228.0
c_{44}	154.4	138.9	80.0	73.3
c_{12}	95.8	85.3	56.3	50.8
c_{44}/c_{12}	1.61	1.63	1.42	1.44
Thermal expansivity				
α /10^{-5} K^{-1}	3.09	3.40	4.05	4.47
	3.12		3.04	

TABLE VIII Calculated and observed structural and physical properties of the two GeO_2 polymorphs at ambient condition. Observed structural data are from Qz-type: Smith and Isaacs (1964); Rt-type: Hazen and Finger (1981). Observed K_0 and K_0' are from Qz-type: Glinnemann et al. (1992); Rt-type: Hazen and Finger (1981). Observed α are derived from Qz-type: Murthy (1962); Rt-type: Rao et al. (1968). Observed c_{ij} are from Qz-type: Grimsditch et al. (1998); Rt-type: Wang and Simmons (1973).

Phase	Qz-type		Rt-type	
Space group	$P3_221$		$P4_2/mnm$	
	Obs	Calc	Obs	Calc
Cell length				
a / Å	4.987	4.990	4.396	4.421
c	5.652	5.647	2.863	2.830
Interatomic distance				
Ge-O / Å	1.737	1.744	1.871	1.879
Ge-O'	1.741	1.681	1.903	1.890
Bond angle				
O-Ge-O' / degree	113.1	113.3	80.2	82.3
O-Ge-O"	106.3	105.5	90.0	90.0
O'-Ge-O"'	110.4	110.4	90.0	90.0
O-Ge-O"'	107.7	109.0	90.0	90.0
Ge-O-Ge'	130.1	134.1	130.1	130.6
Bulk modulus				
K_0 / GPa	39.2	28.8	258	258.7
K_0'	3.8	4.6	7.0	4.7
Elastic constant				
c_{11} / GPa	64	55.1	337.2	381.3
c_{33}	118	123.0	599.4	482.2
c_{44}	37	26.2	161.5	153.8
c_{66}	–	–	258.4	155.1
c_{12}	22	18.1	188.2	151.6
c_{13}	32	22.2	187.4	165.0
c_{14}	2	−4.2	–	–
Thermal expansivity				
a /10^{-5} K^{-1}	2.49	2.65	2.03	2.37
Enthalpy				
H /kJmol^{-1}	–	−3593.3	–	−3631.2

TABLE IX Calculated and observed structural and physical properties of the $MgGeO_3$ polymorphs at ambient condition. Observed structural data are from HPCEn and OEn-type: Yamanaka et al. (1985); Ilm-type: Kirfel et al. (1978); $LiNbO_3$-type: Ito and Matsui (1979); Pv-type (17.9 GPa): Leinenweber et al. (1994). Observed K_0 and K_0' are from HPCEn-type: Nagai (1995); OEn-type: Ross and Navrotsky (1988); Ilm-type: Ashida et al. (1985); Pv-type: Leinenweber et al. (1994). Observed α are derived from HPCEn and OEn-type: Yamanaka et al. (1985); Ilm-type: Ashida et al. (1985). Observed lattice cell lengths of the Pv-type polymorph are at 17.9 GPa. Observed density and bulk modulus of the Pv-type polymorph are the expected values at 0 GPa from fitted Birch-Murnaghan equation of state.

Phase		HPCEn	OEn	Ilm	$LiNbO_3$	Pv
Space group		$C2/c$	$Pbca$	$R\bar{3}$	$R3c$	$Pbnm$
Cell length						
a / Å	Calc	9.668	19.01	4.949	4.968	4.951
	Obs	9.605	18.829	4.933	4.987	(4.832)
b	Calc	8.814	8.877	4.949	4.968	5.138
	Obs	8.940	8.952	4.933	4.987	(5.031)
c	Calc	5.18	5.402	13.702	13.396	7.363
	Obs	5.16	5.347	13.734	13.09	(7.022)
Cell angle						
α / deg	Calc	90.0	90.0	90.0	90.0	90.0
	Obs	90	90	90	90	(90)
β	Calc	99.6	90.0	90.0	90.0	90.0
	Obs	100.95	90	90	90	(90)
γ	Calc	90.0	90.0	120.0	120.0	90.0
	Obs	90	90	120	120	(90)
Density						
ρ_0 g/cm^3	Calc	4.423	4.224	4.968	5.043	5.14
	Obs	4.424	4.271	4.981	5.113	(5.12)
Bulk modulus						
K_0 / GPa	Calc	128.7	95.8	213.5	237.6	253.2
	Obs	127	115	195	–	(213)
K_0'	Calc	6.2	8.4	5.6	5.3	4.4
	Obs	4	4	3.6	–	–
Thermal expansivity						
α / 10^{-5} K^{-1}	Calc	4.42	4.89	3.71	3.48	3.82
	Obs	3.61	4.06	2.2	–	–

Chapter 3

Pressure-induced transitions under hydrostatic condition

3.1 Transitions with coordination change

3.1.1 Calculated P-V relations

Firstly, calculated equations of state of MgO and CaO are shown in Fig. 3.1 and 3.2 with corresponding experimental results, respectively. These results shows that both EOS of B1 (NaCl-type) phases calculated by QEq-MD with multiple exponential repulsion potentials are in quite accurately agreement with not only those of FP-LMTO but also those of the experimental results in wide pressure range. The calculated EOS of MgO is especially most accurate in the previous MD works and no transition occurred in the calculated pressure range as well as the observation. On the other hand, the B1 phase of CaO transformed into the B2 (CsCl-type) phase with abrupt volume reduction as the same as observations. The thermodynamical phase boundary at 300 K approximately estimated from the pressure variation of ΔH was about 40 GPa, which is in fairly good agreement with the observed one (~55 GPa). In spite that the interatomic potential of CaO was optimized only for the B1 structure, not only the EOS of the B2 phase but also the thermodynamical phase boundary were reproduced fairly accurately. These potentials were determined without the fitting procedure to the experimentally observed data. Note that the construction techniques of the interatomic potentials using the present thesis are significantly efficient for the classical MD simulation.

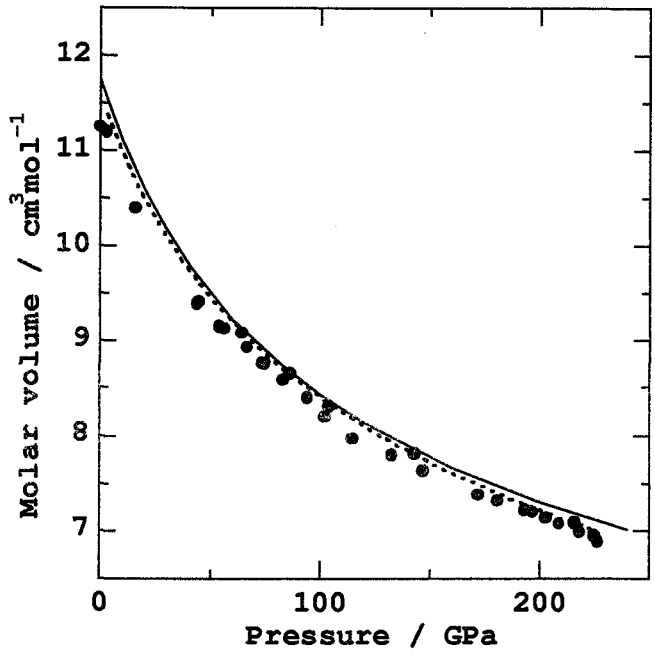

Figure 3.1 The equations of state of MgO. The solid and dotted curves are calculated results of QEq-MD at 300 K and FP-LMTO, respectively. The circle is the experimental result at room temperature under static compression (Mao and Bell 1988, Duffy et al. 1995).

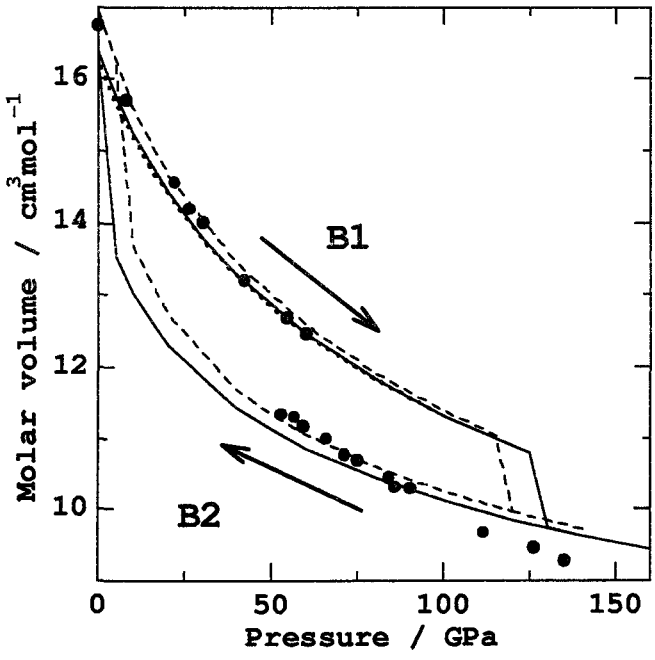

Figure 3.2 The equations of state of CaO polymorphs. The solid and dashed curves are calculated results of QEq-MD at 300 K and 1000 K, respectively. The dotted curve of the B1-type phase is the calculated result of FP-LMTO. The experimental result at room temperature under static compression plotted by the circle is from Richet et al. (1988).

The transition pressure of B1-type CaO under hydrostatic compression is 130 GPa, which is largely overestimated comparing to the thermodynamical phase boundary. Upon decompression of CaO, the back transition from the B2 to the B1 phase occurs at 0 GPa with abrupt volume increase, which is largely underestimated. Namely, there is a very large pressure hysteresis between the calculated B1-B2 transition. In these transitions, the discontinuous volume changes are associated with first-order transition. In general, it is recognized that MD method of an ideal defect-free crystal under homogeneous pressure over/underestimates its transition pressure because of computational limitations of MD method for sluggish nature of the transition. Therefore, at a glance, the large hysteresis is not intuitively curious result in the case of first-order structural transitions.

At 1000 K, the transition pressure of CaO from B1 to B2 lowers about 10 GPa as shown in Fig. 3.2. The back transition pressure increases about 5 GPa. These results mean that thermal energy activates the B1-B2 transition and makes the pressure hysteresis small. However, the experimentally observed hysteresis is only 10 GPa even at 300 K (the circles in Fig. 3.2). It is unlikely that temperature effect is a dominant factor for the transition kinetics in the perfect crystal. We can easily associate that the effects of extrinsic factors such as lattice defects, impurity, grain boundary and temperature and pressure homogeneity are important to study the transition kinetics. It is however noted that these factors are not essential for the B1-B2 transition since the transition itself can be reproduced even in the perfect crystal. This means that an intrinsic transition pathway with no mediation of the extrinsic factor exists between the B1 and B2 structures. It has, however, never been elucidated why they transform at 130 and 0 GPa. It can be considered that the calculated large supercompression/decompression is needed as thermodynamical driving force for the transition or that the energy barrier for the transition itself changes to zero at the calculated transition pressure. The latter case can be called as "mechanical instability."

One of features of QEq-MD method is that the charges of the individual atoms depend on their instantaneous environment. This leads to slightly different charges for the B1 and B2 phases, which change with temperatures and pressures as shown in Table X. Charges increase with pressure and decrease with temperature.

TABLE X Cation charges for different temperatures and pressures for B1 phase of MgO and B1 and B2 phases of CaO. Unit of values is given in e.

P / GPa	MgO-B1		CaO-B1		CaO-B2	
	300 K	1000 K	300 K	1000 K	300 K	1000 K
0	1.348	1.334	1.251	1.233	–	–
40	1.483	1.470	1.376	1.366	1.342	1.330
80	1.581	1.567	1.459	1.450	1.404	1.396
120	1.659	1.646	1.526	–	1.443	1.436
160	1.726	1.713	–	–	1.490	1.483
200	1.785	1.771	–	–	1.507	1.500

Next, calculated results of high-pressure transitions of quartz and enstatite are indicated. The calculated equations of state for two polymorphs of GeO_2 at 300 K are shown in Fig. 3.3 with experimental results for comparison. These calculated EOS agree well with the experimental data. Although the compressibility of quartz is somewhat overestimated compared with experimental results, the empirically determined interatomic potential for GeO_2 can reproduce the trend of compression of GeO_2 polymorphs accurately. Fig. 3.3 shows that quartz undergoes a discontinuous volume reduction resulting from a transition to a denser state at 7.4 GPa, which is the almost same pressure of the experimentally observed amorphization transition, 6.5–7 GPa (Wolf et al. 1992, Yamanaka et al. 1992). No further discrete volume change occur under more compression to 100 GPa, and no back transition to quartz was found upon release of pressure to 0 GPa as well as observations.

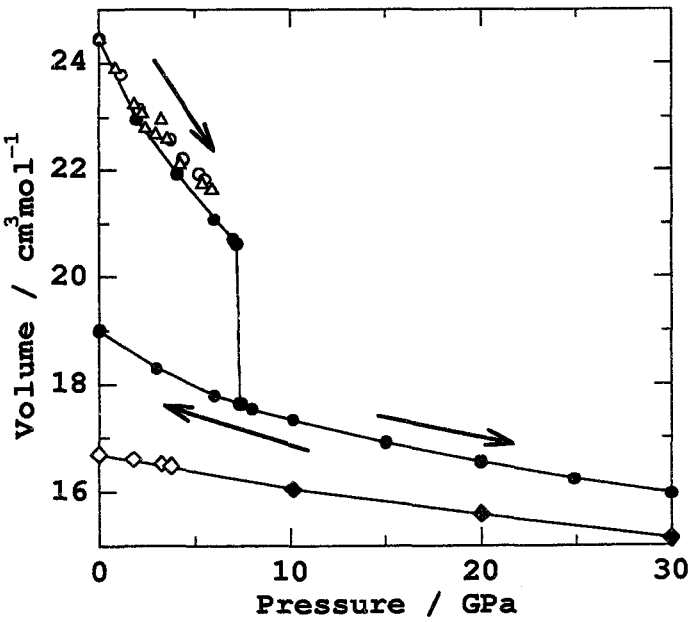

Figure 3.3 The equations of state of GeO_2 polymorphs. Present results of Qz- and Rt-type are shown by the filled circle and diamond, respectively. Experimental values for Qz-type plotted by the open circle and triangle are from Glinnemann et al. (1992) and Kawasaki et al. (1994), respectively. The experiment value for Rt-type plotted by the open diamond is from Hazen and Finger (1981).

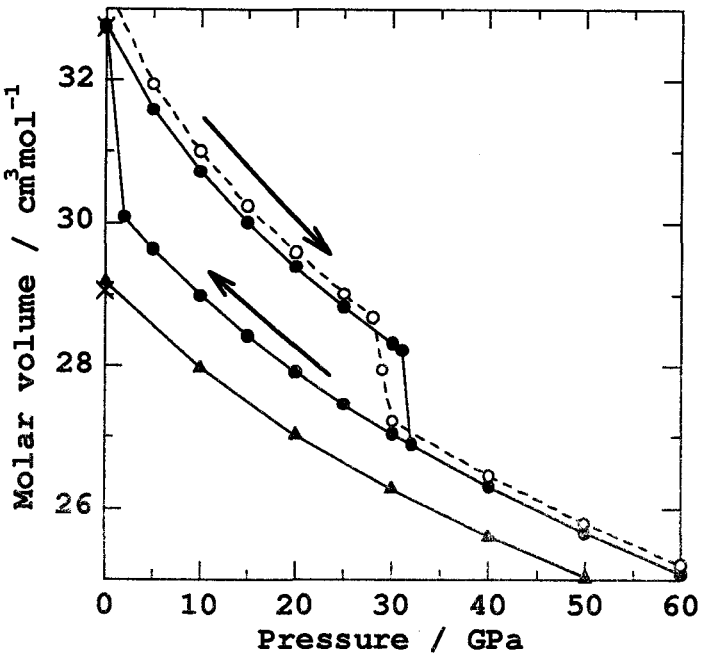

Figure 3.4 The calculated volume variations of HPCEn-type and Ilm-type $MgGeO_3$ as a function of pressure. The filled and open circles show volumes of the HPCEn-type phase at 300 and 650 K, respectively. The filled triangle is it of the Ilm-type phase at 300 K. Crosses are respective experimentally observed results at ambient condition.

Fig. 3.4 shows calculated pressure dependence of volume of the high-pressure-clinoenstatite-type $MgGeO_3$ at 300 and 650 K and the ilmenite-type polymorph at 300 K under hydrostatic conditions. This figure indicates that the pressure-induced transition of the high-pressure-clino-type form to an intermediate density state between clinopyroxene and ilmenite appears at 32 GPa (300 K) and 29 GPa (650 K) with abrupt volume reduction of ca. 5%. No subsequent transition occurred on more compression up to 60 GPa. A back transition to the high-pressure-clino occurred on decompression to ambient pressure. The calculated high-pressure state can not be identified as any of experimentally reported phases and then is called "X_1" in the thesis. This transition is interesting in the following respect. By the previous high-pressure *in situ* X-ray experiment of $MgGeO_3$ under room temperature using the diamond-anvil cell, it was observed that high-pressure-clinoenstatite transformed to an undetermined phase at ca. 23 GPa (Nagai 1995). The observed high-pressure state was also unquenchable to ambient pressure as well as X_1

though the transition pressure was somewhat lower. The structure of X_1 and its transition mechanism are worth investigating since the experimentally observed unknown phase is likely to have some relations to X_1.

At 650 K, the transition pressure to X_1 decreased about 3 GPa and the direct transition to the ilmenite-type phase also never appeared. It is noted that the transition pressure decreases with increasing temperature. This result suggests that temperature activates the transition as well as the case of the B1-B2 transition.

3.1.2 Structural changes with transitions

In Fig. 3.5, the schematic picture of the atomic configurational changes at the B1-B2 transition of CaO is depicted. From this figure, it is clear that the transition can be performed by only a rhombohedral distortion of lattices along [1 1 1] and with no atomic diffusion. Then the crystallographic lattice orientation relations between the two phases in the transition can be represented as

$$[1\ 0\ 0\ ]_{B1} \rightarrow [1\ 1\ 0]_{B2},\ [1\ 1\ 0\ ]_{B1} \rightarrow [1\ 0\ 0]_{B2} \text{ and } [1\ 1\ 1\ ]_{B1} \rightarrow [1\ 1\ 1]_{B2}.$$

The ion packing changes from face-centered cubic (fcc) in B1 to simple cubic (sc) in B2. In spite of the high-pressure structure, the B2 structure has no longer the closed-packing of ions. This indicates that the hard-sphere model in which ions are treated as rigid-body is not valid and the coordination increase is dominant for volume reduction in the B1-B2 transition.

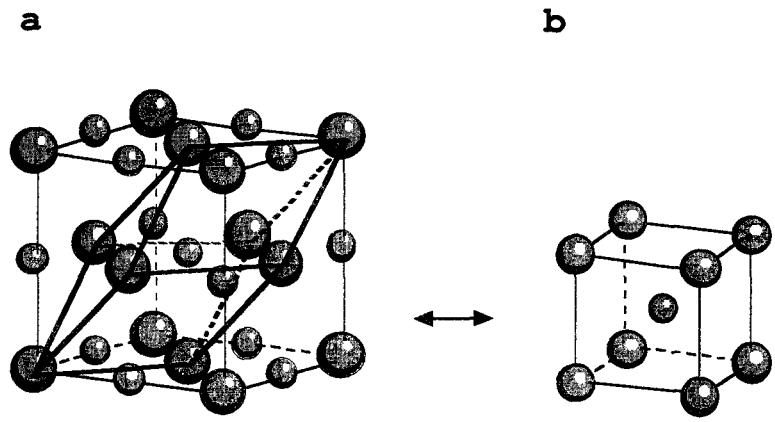

Figure 3.5 The schematic picture of the structural change in the B1-B2 transition. **a** and **b** show the B1 and B2-type structure, respectively. *Thin lines* are unit cells of each lattice and *thick lines* in **a** indicate the B2-type cell. In these figures, The *large* and *small spheres* mean oxygen ions and cations, respectively.

A snapshot of the high-pressure structure of quartz-type GeO_2 obtained after very long structural relaxation of 131000 steps (262 ps) at 7.4 GPa and 300 K is shown in Fig. 3.6. This structure seems to be poorly crystallized. Nevertheless, during the long calculation of the extremely large number of iterations, this structure was unlikely to relax to other crystal structures. As seen from Fig. 3.6, the disordered structure seems to be attributed to the cation configuration. The oxygen anions arrangement seems fairly ordered. (Moreover, the quartz periodicity along c direction was preserved in the transition.) The running coordination numbers shown in Fig. 3.7 were calculated from Eq. (2.20) to investigate the local structure and the particle distribution in the high-pressure state. It can be seen that the fourfold Ge-O coordination in quartz increases to

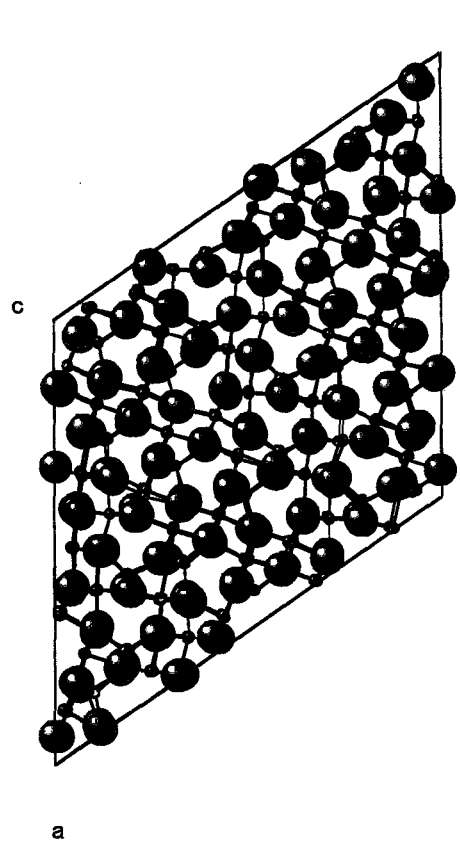

Figure 3.6 The snapshot of the calculated pressure-induced structure of Qz at 7.4 GPa. This figure is a projection along the quartz a axis. The *small* and the *large spheres* indicate germanium and oxygen atoms, respectively.

the intermediate coordination number about 5.3 (solid lines in Fig. 3.7). This indicates that some fourfold-coordinated germanium ions moved to highly sixfold-coordinated sites with the transition. The EXAFS measurement by Itie et al. (1989) and Kawasaki (1996) also indicated the coordination increase of germaniun ion with the amorphization transition. The coincidences of the transition pressure, the cation coordination change, and the quenchable character are quite interesting since these results suggest that the calculated transition of quartz has a strong relation to the experimentally observed pressure-induced amorphization transition.

The O-O RCNs (dashed lines in Fig. 3.7) indicate that the O-O coordination becomes more regular with the transition and almost 12-fold, which is characteristic of a face-centered cubic (fcc) sublattice. The formation of the oxygen fcc sublattice with the transition is similar to the result of Binggeli et al. (1994), although they reported that a body-centered-cubic (bcc) sublattice appeared with the transformation, in which the O-O coordination should be eightfold. It is noted that octahedral cation sites form near tetrahedral sites in the fcc cell (Fig. 3.8). The change in cation coordination from the fourfold to the sixfold site in the fcc cell needs only a subtle displacement of cation with no atomic diffusion process. The mechanism of the structural changes containing the increase cation coordination with pressure-induced transition can be understood by the following sequential processes. (1) Transformation of oxygen packing to the fcc arrangement by some instability of the quartz-type framework. (2) Partial displacements of germanium ions to newly formed sixfold-coordinated sites in the oxygen fcc sublattice. It was reported by the high-pressure X-ray measurement (Sowa 1988) that oxygen atoms tended to arrange themselves in the bcc sublattice upon compression of quartz. It can be therefore considered that the calculated transition corresponds to the discrete change of compression mechanism of the oxygen sublattice. The bcc lattice can be connect to the fcc lattice by the tetrahedral elongation to fulfill $a' = \sqrt{2}a$.

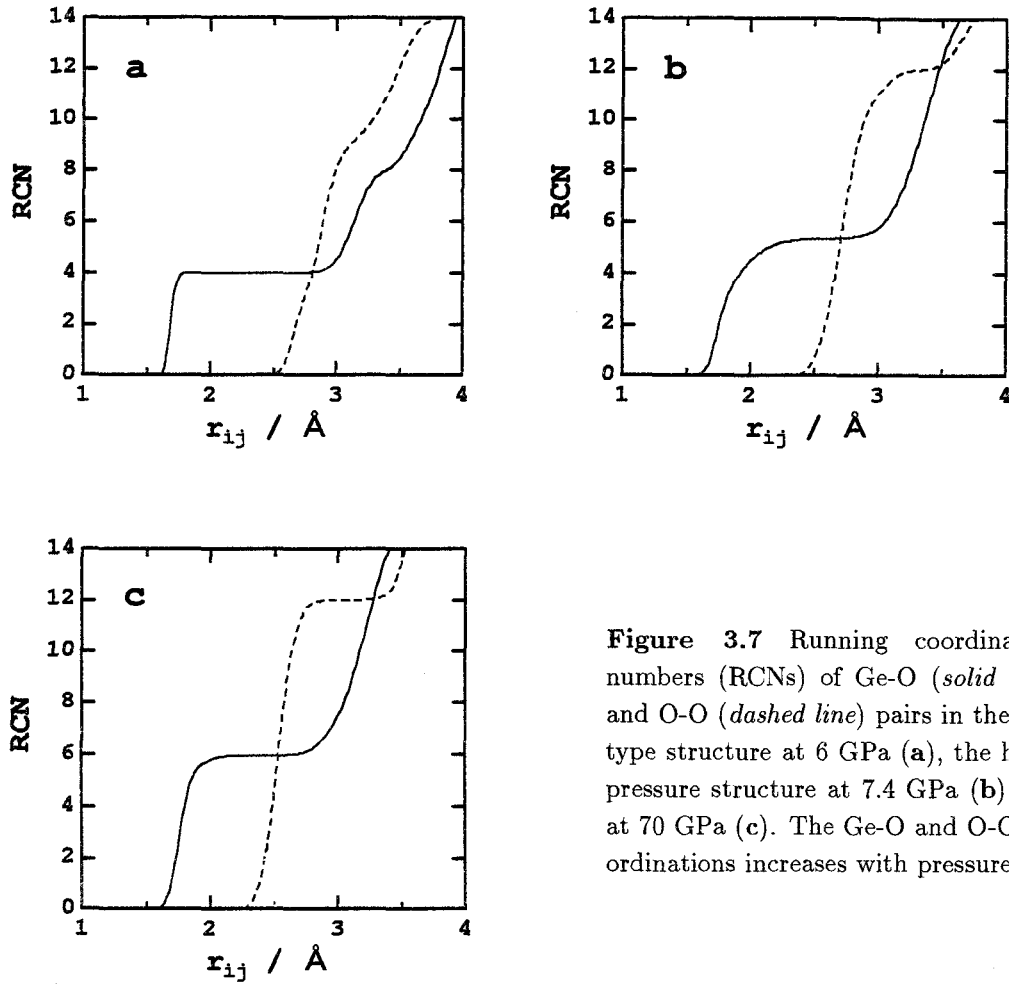

Figure 3.7 Running coordination numbers (RCNs) of Ge-O (*solid line*) and O-O (*dashed line*) pairs in the Qz-type structure at 6 GPa (**a**), the high-pressure structure at 7.4 GPa (**b**) and at 70 GPa (**c**). The Ge-O and O-O coordinations increases with pressure.

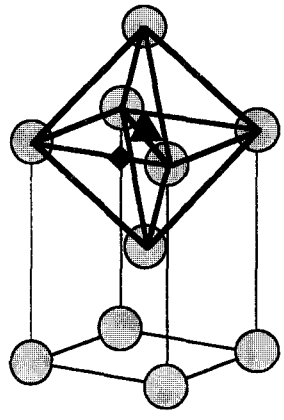

Figure 3.8 The schematic picture of a half of the fcc lattice. The circle is oxygen ion. The diamond and triangle are the fourfold- and sixfold-coordination cation sites in the bct cell, respectively. Thick lines indicate corresponding tetrahedral and octahedral coordination polyhedra.

From the viewpoint of regularity of the oxygen arrangement, the structure obtained after the transition should not be regarded as amorphous phase. These states may be related to an intermediate crystalline phase just before amorphization of SiO_2 previously discovered by Kingma et al. (1993) or a local structure of the amorphous phase. In the latter case, the "amorphous" character must originate in disorder of a much larger-scale structure.

The subsequent increase in coordination number of germanium ions depends not on the calculated duration but on pressure. Almost all cations finally displaced to the sixfold-coordination site and the oxygen sublattice became more regularly at 70 GPa (Fig. 3.7c). This structure may be recognized as the crystalline structure of alternating α-PbO_2 slabs proposed by Binggeli et al. However, this state was never denser than the rutile-type phase and returned to the intermediate coordination state on decompression. Therefore, it is unreasonable to recognize the state at 70 GPa as a high-pressure stable phase. During further compression up to 100 GPa, no transition to the other structure appeared. This result indicates that the calculated high-pressure structure is comparatively stable with respect to pressurization, and consistent with the previous observation. Yamanaka et al. (1992) reported that after amorphization transition, any crystallization seemed to be prohibited kinetically or to progress very slowly even if more compression up to 30 GPa was applied.

The structure of X_1 which is the calculated high-pressure state of high-pressure-clinoenstatite-type $MgGeO_3$ is shown in Fig. 3.9. The impressive structural property of X_1 is that the oxygen packing manner changes from ccp toward the hcp by the slips of the oxygen dense planes every other layer (see Fig. 5.5). The ccp stacking direction in high-pressure-clinoenstatite which is along [1 0 0] in high-pressure-clinoenstatite, and hcp-like stacking direction in X_1 are shown by gray and black arrows, respectively. By this modification,

the germanium coordination number in X_1 shown in Fig. 3.10 increases from fourfold to sixfold and consequently, the two types of the spacing between oxygen dense planes in the clinopyroxene become almost equal in X_1. It is considered that the first-order volume reduction results from the germanium coordination increase. However, the intermediate oxygen packing in X_1 seems mechanically not so stable since large void bands and adjacent cation densely packed bands along [1 1 0] must make the lattice severely distorted. It can be considered that this is the origin of the unquenchable nature of X_1.

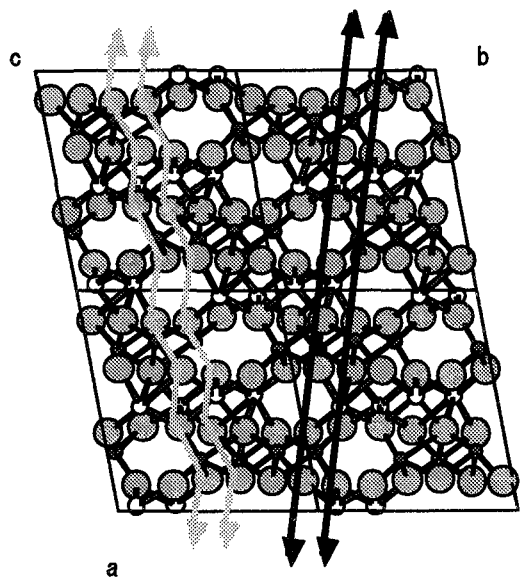

Figure 3.9 The snapshot of the calculated structure of the high-pressure phase X_1. The *large circle* indicates oxygen anion, and the *small gray* and *white circles* are germanium and magnesium cations, respectively. Arrows mean stacking orientations of the dense plane of oxygen ions; the ccp stacking in CPx (*gray*) and near the hcp stacking (*black*). The figure is projection along [0 0 1] of the HPCEn-type structure.

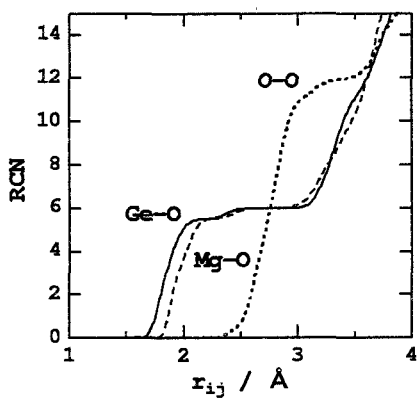

Figure 3.10 Running coordination numbers (RCNs) of Ge-O (*solid line*), Mg-O (*dashed line*) and O-O (*dotted line*) pairs in X_1. The value of Ge-O coordination in X_1 increases to 6-fold.

3.2 Transition without coordination change

To investigate the post rutile transitions of GeO_2, MD calculation was carried out with increasing pressure to 125 GPa at 300 and 1000 K. The calculated variations of the lattice parameters shown in Fig. 3.11 indicate that a pressure-induced transition from the tetragonal rutile-type to a new orthorhombic structure takes place at ca. 80 GPa without discontinuous volume change. The calculated high-pressure phase has the $CaCl_2$-type structure ($Pnnm$). As shown in Fig. 3.12, this rutile-to-$CaCl_2$ transition is described by small orthorhombic distortion of the lattice accompanied by a slight rotation of the columns of octahedra with no coordination change of ions. In other word, the optic B_{1g} phonon mode corresponding to the libration of the columns of octahedra about their

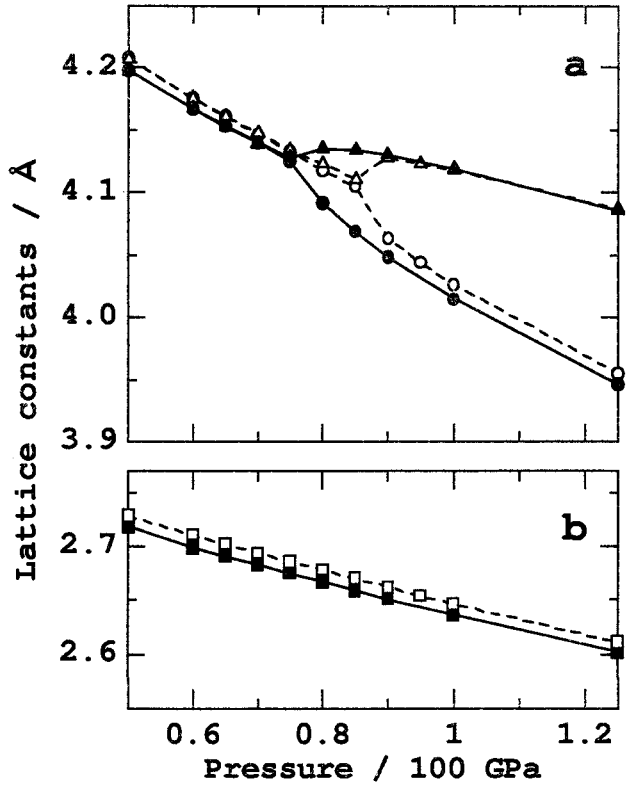

Figure 3.11 Pressure dependence of the lattice parameters of the Rt-type polymorph of GeO_2 at 300 K (filled figures) and 1000 K (open ones). In **a**, the circles and triangles indicate a and newly formed b axis, respectively. In **b**, c axis is depicted.

twofold axes along c direction condenses in the $CaCl_2$ phase. During decompression, therefore, the $CaCl_2$-type phase fully returns to rutile with no pressure hysteresis. And the high-pressure phase is unquenchable. These results indicate that the rutile-to-$CaCl_2$ transition is the second-order transition and the calculated transition pressure is exactly thermodynamical phase boundary. As shown in Fig. 3.11, at 1000 K, the transition pressure increases about 10 GPa. This means the Clapeyron slope (dT/dP of the phase boundary) is positive.

In general, based on systematics of AX_2-type compounds, it has been believed that rutile structure may directly transform into an eightfold-coordinated fluorite structure as found in some fluoride. However, the calculated results demonstrate that GeO_2 will exist in the $CaCl_2$-type structure at high pressure before the fluorite-type transition. It is interesting in respect of correspondence to the in situ X-ray diffraction experiment (Tsuchida and Yagi 1989) and theoretical calculations (Cohen 1992; Matsui and Tsuneyuki 1992). Furthermore, by recent in-situ Raman spectroscopic measurements of SiO_2 and GeO_2 by Kingma et al. (1995) and Haines et al. (1998), respectively, it was found that the B_{1g} optic phonon mode of the rutile-type phase softened up to the transition pressure and then became a hard A_g mode of $CaCl_2$-type phase.

In the rutile-type structure, oxygen ion occupies the position $(x, x, 0)$ and $x = 0.302$ at ambient pressure. If $x = 0.25$, the oxygen packing would form an ideal body-center-cubic sublattice. The pressure variation of the oxygen atomic position x schematically displayed in Fig. 3.13 decreased with pressure up to 0.299. Whereas in the $CaCl_2$-type structure, the oxygen position is $(x, y, 0)$ and x further decreased but y increased with pressure. From viewpoint of the variation of the oxygen packing, the compression mechanism of the rutile-type structure can be regarded as a change toward the bcc sublattice. In contrast, that of the $CaCl_2$-type structure is a change toward the hexagonal-closed-packing (hcp). This result seems to be reasonable since, in general, hcp is denser than

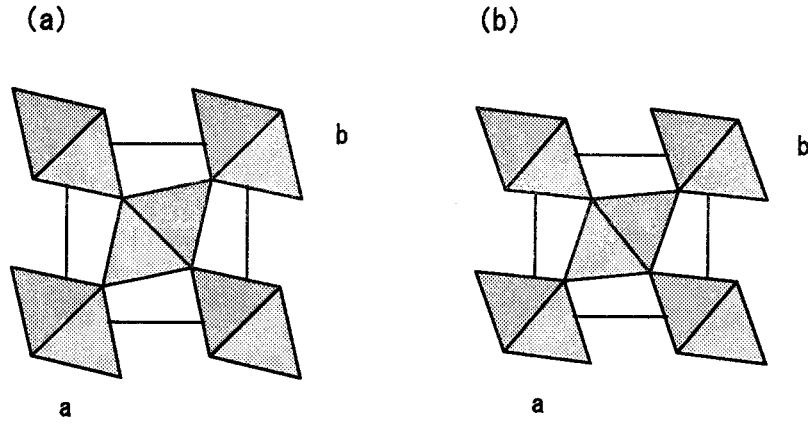

Figure 3.12 The schematic picture of the transition mechanism from the Rt-type structure to the $CaCl_2$-type structure: (a) Rutile structure ($P4_2/mnm$) and (b) $CaCl_2$ structure ($Pnnm$).

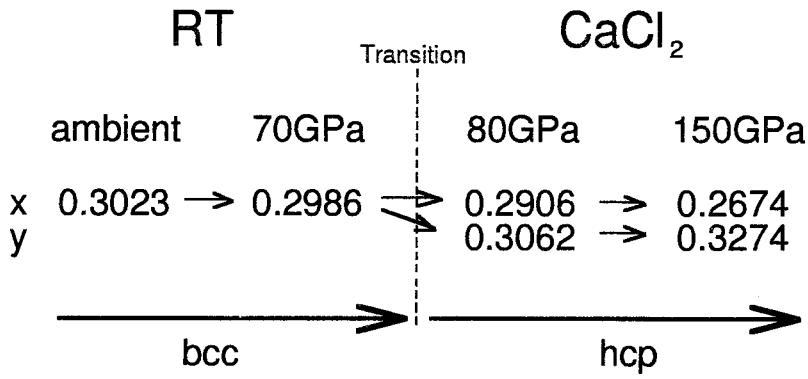

Figure 3.13 The diagram of the pressure variation of the oxygen atomic position $(x, y, 0)$ in Rt-type and $CaCl_2$-type phases.

bcc packing.

Comparison with another post-rutile transition

On the other hand, it has been known by a high-pressure experimental study (Yagi et al. 1979) that MnF_2 which is the rutile-type structure at ambient condition undergoes a first-order pressure-induced structural transition to a cubic fluorite-type phase at 3 GPa differing from the case of GeO_2 and SiO_2. The fluorite-type structure has a cubic symmetry and a space group $Fm\bar{3}m$. In this structure, the configurations of cations and anions form the face-centered cubic (fcc) and the simple cubic packing, respectively, and the coordination number of cations increases from six to eight. MD calculations of MnF_2 were carried out using a potential model previously proposed by Cormack et al. (1989), of which validity was reported in their paper. In Fig. 3.14, the variations of the volume and the lattice parameters of rutile-type MnF_2 with pressure at 300 and 600 K are described. At 7 GPa and 300 K, the rutile-type phase transformed to a high-pressure structure that could be identified as the fluorite-type structure. It can be confirmed that this model potentials for MnF_2 could reproduce the observed phase relations to the fluorite-type structure although the transition pressure was overestimated about 4 GPa. In the case of MnF_2, the post-rutile transition occurred with a sadden volume reduction, and the transition pressure decreased with heating. These results indicate that differing from GeO_2, the rutile-to-fluorite transition has the first-order character and suggest that the transition has a negative Clapeyron slope. Moreover, upon decompression to zero pressure, a reverse transition had never occurred. Therefore, the calculated fluorite-type phase is quenchable. It is quite interesting that these results are fully consistent with experimental observations.

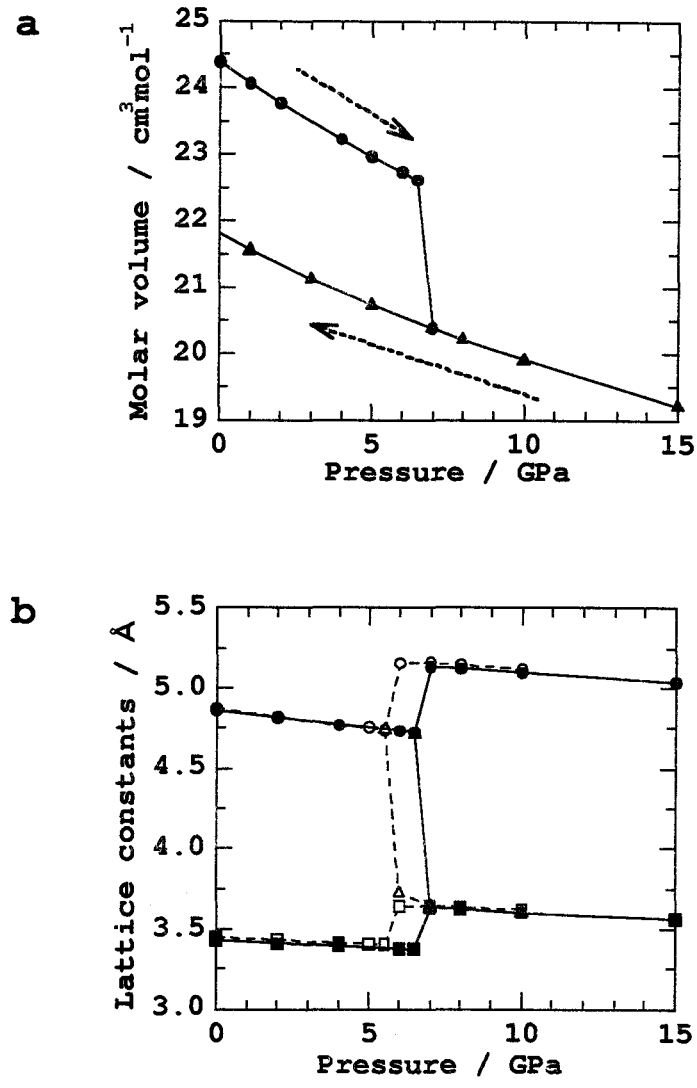

Figure 3.14 Pressure dependence of the volume at 300 K (**a**) and the lattice parameters (**b**) of the Rt-type polymorph of MnF_2 at 300 K (filled figures) and 600 K (open ones). In **a**, the circle and triangle indicate the rutile-type and the fluorite-type structure, respectively, and the volume changes under both compression and decompression are depicted. In **b**, the results on only compression is shown, and the circles, triangles and squares indicate *a*, newly formed *b* and *c* axis, respectively.

The calculated atomic displacement with the transition is schematically shown in Fig. 3.15. In this transition, manganese cations did not move from their position in the rutile-type cell as well as the rutile-$CaCl_2$ transition, but the migration of fluorine anions is quite different from that in the rutile-$CaCl_2$ transition. The waving arrangement of fluorine anions in the (0 0 1) plane of the rutile-type structure was spread out on a straight line by the transition, as shown by thick lines in figure. It is appropriate that

the migration of fluorine anions is described by the anion packing change rather than the rigid rotation of coordination polyhedra. From viewpoints of the ion packing, the bct-sublattice of cations in the rutile-type structure changed into fcc-sublattice that is a supergroup of bct lattice, with only cell elongation. The packing of fluorine anions changed from the intermediate rutile-type packing to the simple cubic packing with the transition. These results seems reasonable since the denser packings realized with the transition. Consequently, a axis of the rutile-type phase corresponds one of three lattice orientation of the fluorite-type structure (c' in Fig. 3.15) with a relation of cell length $a = 2c'$. Then the (1 0 0) and the (0 0 1) plane of the rutile-type structure change to the (1 0 0) and the (1 1 0) plane of the fluorite-type, respectively. Through the transition, there was no atomic diffusion.

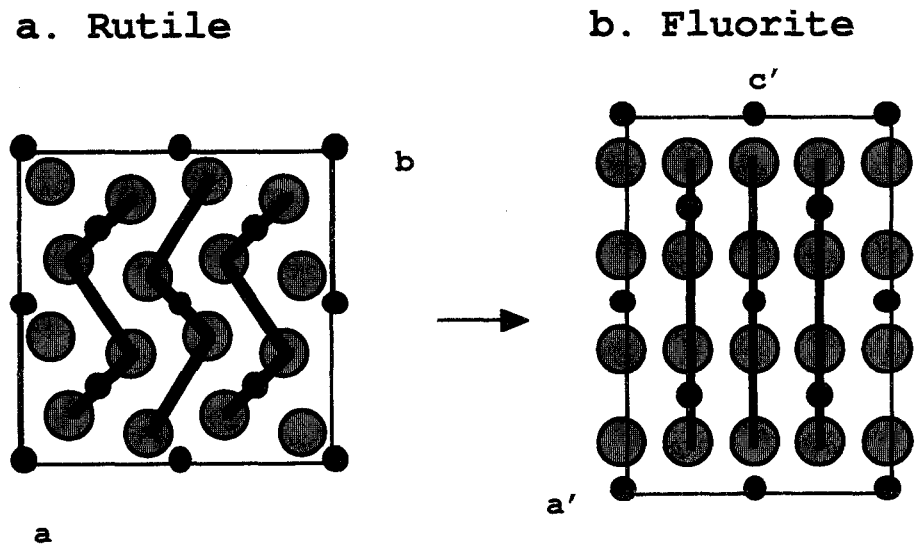

Figure 3.15 The schematic picture of the atomic configuration change in the rutile-to-fluorite transition. a and b (=a) plotted in **a** are the crystallographic lattice orientations of the rutile-type structure, and a', b' (=a') and c' (=a') plotted in **b** are those of the fluorite-type structure. The *large* and *small* circles indicate fluorine and manganese ions, respectively.

3.3 Summary and discussion

- By newly developed QEq-MD method and traditional empirical MD method, the several observed pressure-induced structural transitions are successfully reproduced. The compression mechanisms and the structural changes with the transitions are described in detail. Especially, it is considerably interesting that QEq-MD can reproduce the equations of state of MgO and CaO in very wide pressure range. This is owing to the large flexibility of the multiple exponential repulsion potentials, which never cause serious increase in difficulty in the optimization of parameters if using *ab initio* energy surface.

- The calculated systems can be recognized as pure infinite single crystals. Therefore some transitions occur with large pressure hysteresis. In the case of the transitions accompanied by coordination change, first-orderly discrete volume changes and pressure hysteresis exist, and the oxygen packing manner dramatically changes with the transitions. In the case of the transitions without coordination change, no discrete volume change and no pressure hysteresis exist. The oxygen packing manner hardly changes with the transitions and the transitions have second-order type features.

- In both cases, the calculated transitions occur by only deformation of lattices without atomic diffusion processes. This is owing to limited kinetics in the perfect crystals. Therefore some topotactic relationships exists between the high- and low-pressure structure.

The properties of the transitions are summarized as the following table.

transition	type	lattice	packing		coordination	
			cation	anion	cation	anion
B1-B2	1st-order (sluggish)	C→C	fcc→sc	fcc→sc	6→8	6→8
Qz-OFCC	1st-order (sluggish)	H→TC	–	f.w.→fcc (bct)	4→5.5	2→2.7
HPCEn-X_1	1st-order (sluggish)	M→M	–	fcc→hcp-like	4→6 (Ge)	3,4→4
			–		6→6 (Mg)	
Rt-Fl	1st-order (sluggish)	T→C	bct→fcc	bct-like→sc	6→8	3→4
Rt-$CaCl_2$	2nd-order	T→O	bct→bco	bct-like→hcp	6→6	3→3

OFCC:calculated high-pressure state of Qz containing the oxygen fcc sublattice, f.w.:framework
C:cubic, T:tetragonal, O:orthorhombic, H:hexagonal, M:monoclinic, TC:triclinic

In these six cases of pressure-induced transitions, the first-order transitions occur with coordination increase and reconstruction of anion packing. The second-order transition has no reconstructive changes of ions and their coordinations. This suggests that the anion packing change is inevitable for pressure-induced polymorphic transition with coordination change. For other example, in the ilmenite (hcp)-perovskite (fcc-like) transition of $MgSiO_3$, magnesium ion changes from 6-fold to 8-fold state. In ionic materials, the anion packing is generally one of most dominant factors to influence density. Crystal structures of many minerals can be understood by combination of the anion sublattice and the cation distribution in it. From the crystallographic point of view, fcc and hcp is known as denser packings than sc and bct since these are the closest configuration of a stack of hard spheres, and high-pressure phases are likely to have denser ion packings than low-pressure phases have. (In the rutile-fluorite transition, the cation packing changes to closest.) However, the fact that the B2 structure has the looser anion packing than low-pressure phase clearly indicates a failure of the hard sphere model at high-pressure transitions. From this, it is likely to the coordination increase is more important for

increase in density at high-pressure transition.

In the case of the reproduced first-order transitions (B1-B2, Rt-Fl transition), it can be considered that the calculated large supercompression/decompression is needed as thermodynamical driving force for the transition or that the energy barrier for the transition itself changes to zero at the calculated transition pressure. The latter case can be called as "mechanical lattice instability." The elastic properties will be discussed on the basis of the concept of elastic stability conditions of the ideal lattice in the next chapter.

Chapter 4

Elastic instability at transition

4.1 Born's elastic stability condition

Mechanical stability of cubic lattice is represented by Eq. (1.5) based on the elastic lattice theory. In Fig. 4.1a, the pressure and temperature dependence of elastic constants of the B1 phase of CaO are described. The figure demonstrates that at 300 K, the modulus c_{44} related to shear stability decreases with pressure and vanishes at ca. 130 GPa (indicated by an arrow). This pressure is the same as the calculated B1-B2 transition pressure (ca. 130 GPa) shown in Fig. 3.2. This result indicates that c_{44} softens up with increase pressure and the B1-type lattice becomes elastically unstable at the transition pressure. In Fig. 4.1b, the pressure and temperature dependence of elastic constants of the B2 phase of CaO are described. This figure means that at the back transition pressure (ca. 0 GPa) in Fig. 3.2, the value of c_{44} of the B2 lattice vanishes. Namely, the B2-type lattice becomes elastically unstable at this pressure. From these results, it can be considered that in MD calculations, the B1-B2 transitions occur with the elastic shear instabilities without thermal environmental change. In Fig. 4.1c, the pressure and temperature dependence of elastic constants of the B1 phase of MgO are described with the recent Brillouin scattering result. Pressure derivatives of c_{11} and c_{12} were reproduced quite accurately, although the value of c_{44} was somewhat underestimated. Even though there is the small underestimation, this result indicates that to the contrary to CaO, all stability conditions

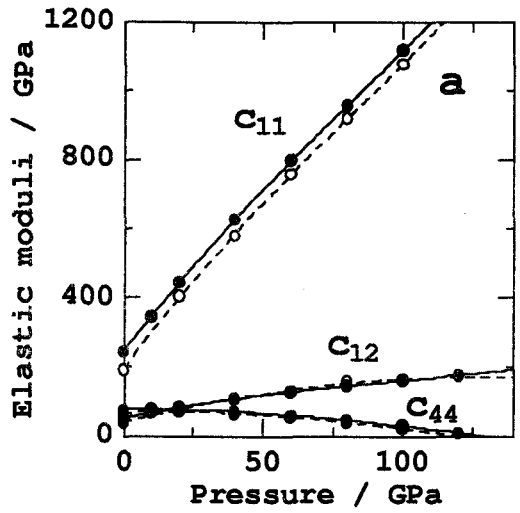

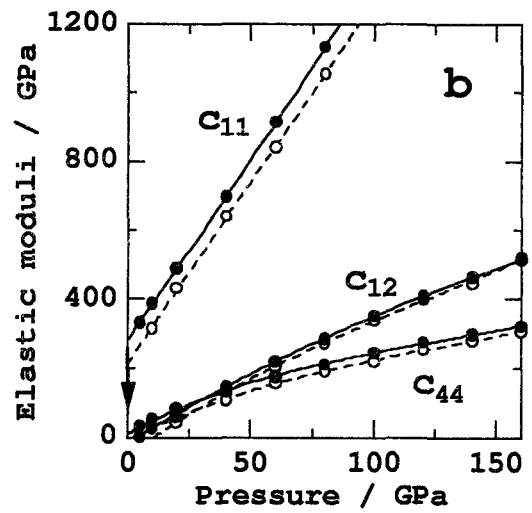

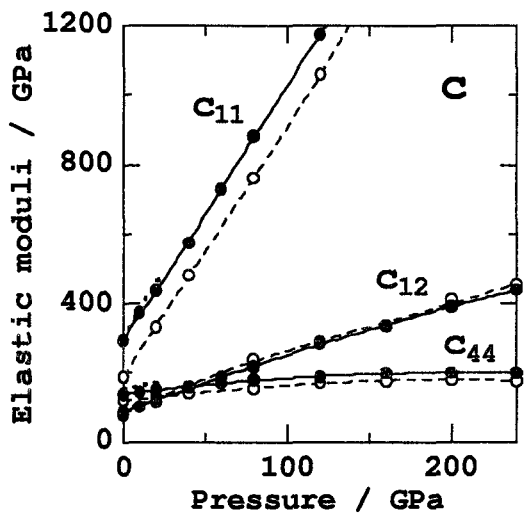

Figure 4.1 The calculated elastic constants of the B1-type (**a**) and the B2-type (**b**) lattice of CaO and the B1-type of MgO (**c**) as a function of pressure. In **a** and **b**, the filled and open circles are the results at 300 and 1000 K, respectively. In **c**, the filled and open circles are the results at 300 and 2000 K, respectively. The dotted lines in c are the observed results by Sinogeikin and Bass (1999).

are fulfilled in the calculated pressure range for MgO. It is reasonable since no high-pressure transition has occurred (Fig. 3.1) in this pressure range in agreement with the experimental result.

As shown in Fig. 4.1ab, although at 1000 K, the pressures at which the stability condition vanishes change toward the observed transition pressure so that the hysteresis decreases, the temperature effect on c_{44} is not so large as to change the pressure at which the stability condition vanishes dramatically. This indicates that in the real system, therefore, more complicated factors (lattice defect, impurity, grain boundary, temperature and pressure heterogeneity and so on) which may significantly contribute the kinetics of the transition, should narrow the hysteresis of the transition down. However even if in the ideal static lattice, the instability must occur at the pressure when $c_{44} = 0$ because of elastic instability. These critical pressures can therefore be considered as spinodal points of the transition and an upper or lower limit of the transition pressure. This concept is consistent with the structural changes at the B1-B2 transition shown in Fig. 3.5. It can be considered that the B1-B2 transition is fundamentally driven by instability in c_{44} rather than by thermal activation.

These results suggest that we can regard the decrease in c_{44} as a precursor phenomenon of the mechanical instability of the B1 lattice. In comparison with alkali halides and other alkaline-earth oxides, the B1-B2 transition is also expected for MgO. The transition pressure is of interest from the geophysical point of view. From Fig. 4.1c, the pressure-induced elastic instability in B1-type MgO hardly appears in the Earth's pressure range. By second-order extrapolation, c_{44} decreases to zero at ca. 540 GPa even under 2000 K. Considering this pressure as the upper limit of the transition pressure, the thermodynamical phase boundary of the B1 and B2 phases may lie at lower pressure than 540 GPa. Previous first-principle total energy calculations predicted it was at 451 (pseudopotential: Karki et al. 1997) and 510 GPa (LAPW: Mehl and Cohen 1988).

The high-pressure Cauchy relation for hydrostatic conditions (Eq. (1.8)) will be fulfilled when interatomic forces are purely central. Fig. 4.2 shows the deviations from the Cauchy relation of B1-type MgO and B1 and B2-type CaO, and these results indicate the presence of highly noncentral forces in all cases. Moreover the deviations increase with increasing pressure, indicating that noncentral nature of the bonding becomes greater at high pressures. This trend agrees with the experimental result of MgO of Sinogeikin and Bass (1999) although QEq-MD underestimates pressure dependence as well as the previous pseudopotential calculations (Karki et al. 1997). The differences between the experimental and calculated values of the Cauchy violation are due primary to c_{44} being underestimated in the QEq-MD (Fig. 4.1c). Noncentral nature of the bonding is smaller in CaO than in MgO, and it is smaller in B1 than in B2. It moreover becomes smaller at high-temperature except B2-type CaO at low-pressure.

These materials can not be thought of as materials composed of rigid ions. Calculated band structures indicate that B1-type MgO and CaO remain wide-gap insulator to pressure beyond those in the mantle (Appendix D). It seems that covalent and metallic bonding are not important in these materials. The relevant many-body force is strain-induced variations in the Madelung potentials.

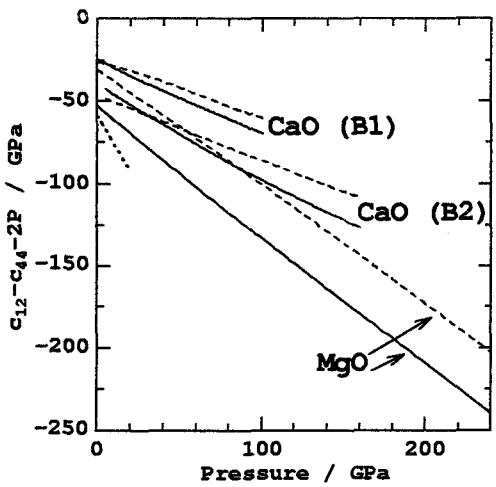

Figure 4.2 Deviations from the Cauchy relation as a function of pressure. The solid lines are at 300 K. The dashed lines are at 2000 K (MgO) and 1000 K (CaO). The dotted line is the experimental result of Sinogeikin and Bass (1999).

Next, the mechanical stability of quartz is presented. According to Born and Huang (1954), the mechanical stability of a trigonal lattice can be estimated from their stability conditions Eq. (1.6). In this thesis, we call the first, second and third moduli in Eq. (1.6) B_1, B_2 and B_3, respectively. The lattice is elastically stable if all of these conditions of elastic moduli are satisfied under a given pressure and temperature. The six elastic moduli of quartz were calculated under compression from ambient to 7 GPa that was slightly lower than that of the transition pressure. Only the value of c_{44} had a negative correlation to pressure.

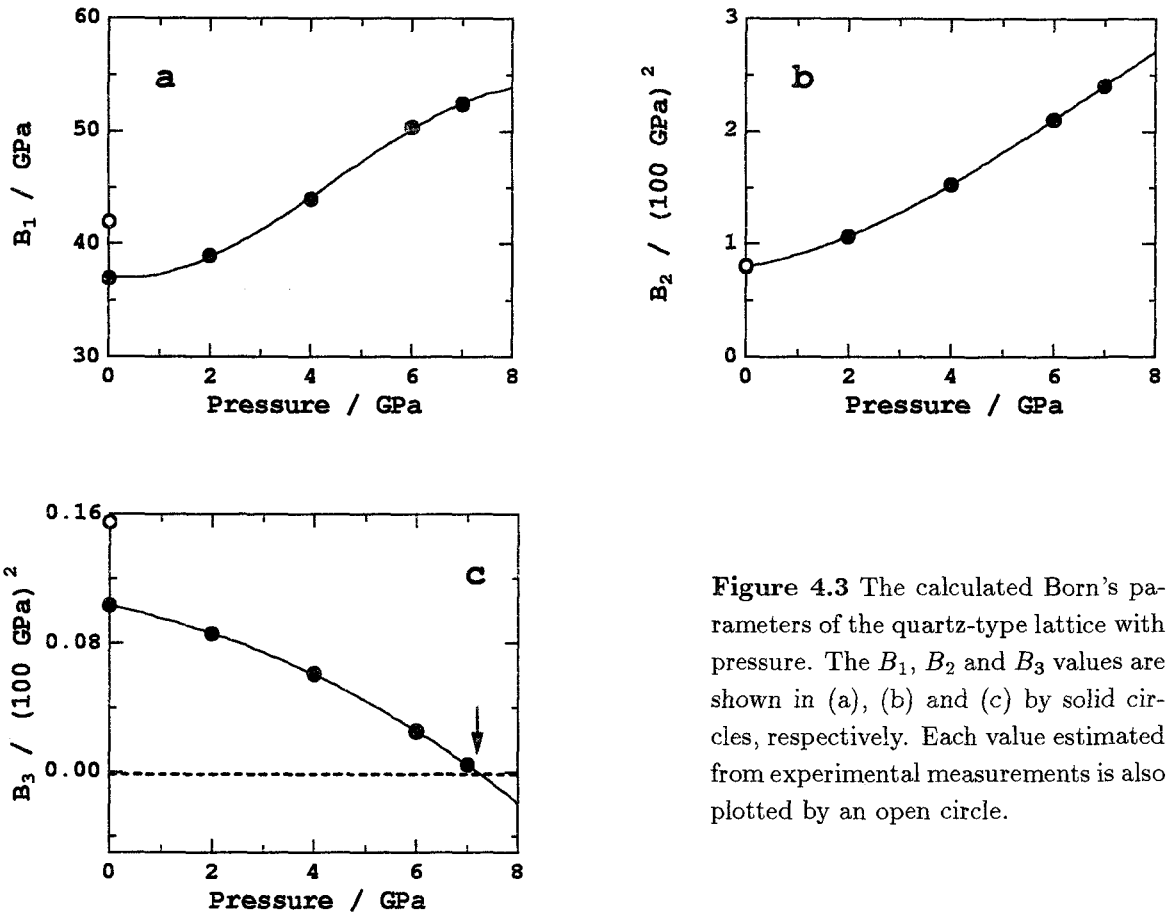

Figure 4.3 The calculated Born's parameters of the quartz-type lattice with pressure. The B_1, B_2 and B_3 values are shown in (a), (b) and (c) by solid circles, respectively. Each value estimated from experimental measurements is also plotted by an open circle.

The variations of three moduli as a function pressure are indicated in Fig. 4.3. Experimental values calculated from data of Grimsditch et al. (1998) at ambient pressure are also plotted. Both B_1 and B_2 parameters increase regularly with pressure and are positive in all pressure range up to the transition. Therefore, values of these two parameters satisfy stability conditions, and these modes are not involved in instability in the quartz-type lattice. However B_3, which indicates the shear stability of the lattice, decreases with pressure and vanishes at ca. 7 GPa which is near the transition pressure, as a result of decrease of c_{44} with pressure. This indicates that the lattice shear instability is induced by pressure and it causes the volume collapse with the transition. This calculated result is similar to the case of SiO_2 α-quartz (Binggeli et al. 1994). It is considered that the amorphization transition is an observable phenomenon of elastic instability under a thermally underactive state, and this process is different from the mode of the thermodynamical nucleation and growth.

Tse and Klug (1991) reported the sudden decrease in the modulus B_2 as a function of time at the critical pressure. For a trigonal structure, B_2 can be related to the stability of the volume compressibility which is given by $(c_{11} + c_{12} - 4c_{13} + 2c_{33})/B_2$. This result indicates that a discontinuous volume reduction occurred at the first-order transformation because the decrease in B_2 to zero corresponds to the divergence in compressibility. The violation of the condition $B_2 > 0$ displayed here should be considered as the result of the transformation rather than its cause.

The rutile-to-$CaCl_2$ phase transition lowers its crystallographic symmetry from tetragonal to orthorhombic system and the rutile-to-fluorite transition rise it to cubic system. In both cases, we can expect that transitions must be accompanied by elastic instabilities related to tetragonal instability since cell angles are invariant with transition. Calculated elastic constants and their variation as a function of pressure are plotted in Fig. 4.4. On

the basis of the Born's elastic theory, the tetragonal stability was described by the first condition in Eq. (1.7) relating its tetragonal shear modulus,

$$c_{11} - c_{12} > 0. \tag{4.1}$$

The pressure variations of this modulus of rutile-type GeO_2 and MnF_2 at ambient and high temperature are shown in filled and open circles in Fig. 4.5a and b, respectively. In both cases, the modulus $c_{11} - c_{12}$ softens up with increasing pressure and becomes zero at the transition pressure. These results mean that the pressure-induced transitions calculated in this study originate the tetragonal elastic instability. After the transition to the $CaCl_2$-type phase, this modulus turned to increase continuously from zero (Fig. 4.5a). On the other hand, in the case of MnF_2, this modulus discontinuously increased at the transition to the fluorite-type phase. Other stability conditions of tetragonal lattices increase on compression and then are always fulfilled. These results indicate that both the rutile-to-$CaCl_2$ and the rutile-to-fluorite transition are followed by elastic instability of the tetragonal modulus as expected and the orthorhombic or cubic structure becomes elastically stable with increasing pressure after the transition.

Upon decompression, in the case of $CaCl_2$-type GeO_2, the modulus went on the fully same line as the case of compression. The tetragonal modulus decreased with decreasing pressure and then vanished at the same pressure as the case of compression. At this pressure, the $CaCl_2$-type phase became unstable and reversed to the rutile-type structure. And then the modulus increased with decreasing pressure. From these results, it can be considered that the reversible character of the rutile-$CaCl_2$ transition is explained by no gap between the unstable pressures of both the low- and high-pressure phases. On the other hands, the modulus was always positive (diamond in Fig. 4.5b) in fluorite-type MnF_2 although it decreased under decompression. Fluorite is still stable elastically at the

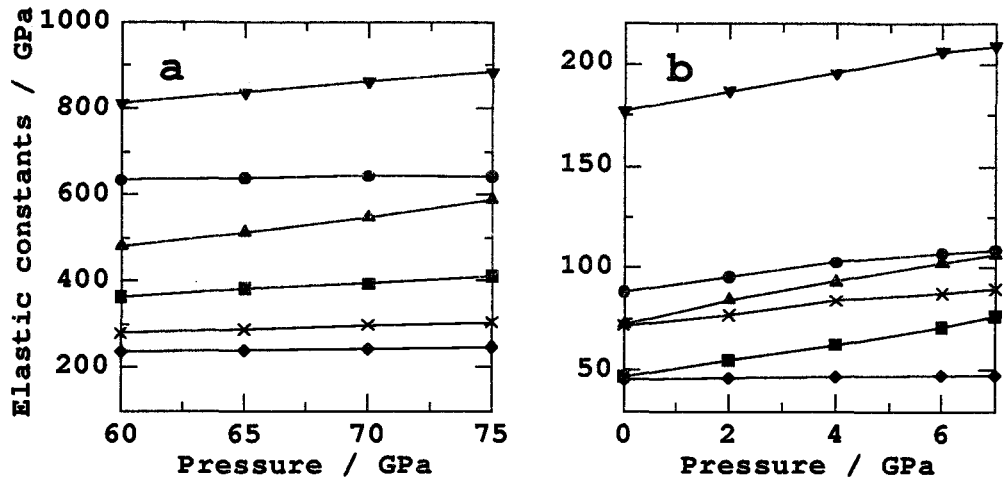

Figure 4.4 The calculated variations of elastic constants of rutile-type GeO_2(**a**) and MnF_2(**b**) with pressure at 300 K. The filled circle, triangle, inverse triangle, square, diamond and cross indicate c_{11}, c_{12}, c_{13}, c_{33}, c_{44} and c_{66}, respectively.

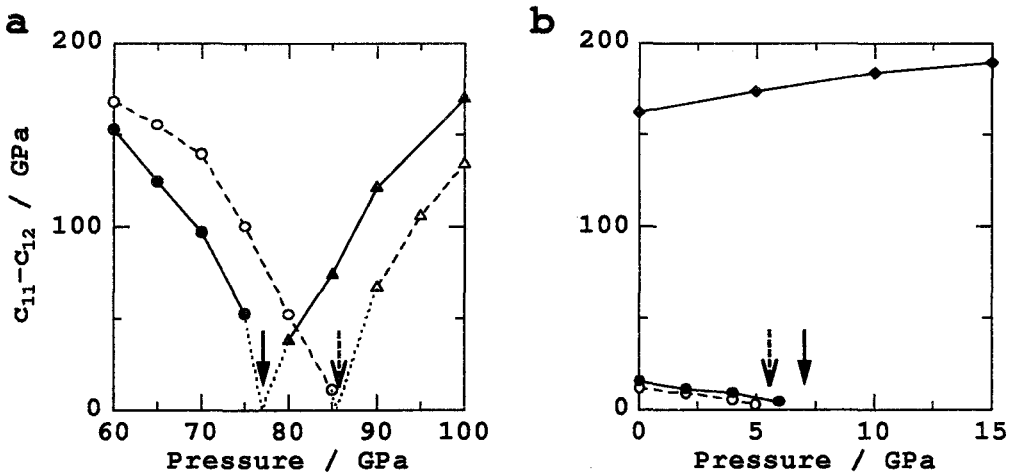

Figure 4.5 The variations of tetragonal modulus, $c_{11} - c_{12}$, of GeO_2(**a**) and MnF_2(**b**) with pressure. The filled figures are the values at 300 K and the open figures are the high-temperature values at 1000 K in **a** and 600 K in **b**. The triangle in **a** is the value of the $CaCl_2$-type structure and the diamond in **b** is the value of the CaF_2-type structure.

pressure which rutile becomes unstable. This explains no back transition under decompression and the first-order nature of the rutile-fluorite transition.

The rutile-to-$CaCl_2$ transition can be connected to the ferroelastic phase transition, in that the transition involves the creation of a reversible spontaneous strain (Dove 1993). In general, the ferroelastic transition is accompanied by the combination of elastic constants that falls to zero at transition temperature or pressure. The gradient of one of the transverse acoustic modes at zero wave vector falls to zero, since the long wave length limit of acoustic branches can be related to elastic constants. In the case of GeO_2, as reported by the high-pressure Raman spectroscopic measurement of Haines et al. (1998), the optic mode softening also accompanies the transition because the soft optic B_{1g} mode corresponds to the libration of the columns of octahedra about their twofold axes along c direction, which condenses in the $CaCl_2$ phase as noted in the previous section. The calculated mean square displacement of germanium and oxygen ions at 300 K decreased from 0.007, 0.008 $Å^2$ at ambient pressure to 0.005, 0.007 $Å^2$ at 75 GPa, respectively. The change about oxygen ion is 16% smaller than it about germanium ion. The large fluctuating behavior of oxygen ion may result from the B_{1g} softening optic mode prior to the transition.

Another quite interesting result is temperature dependence of the tetragonal moduli in Eq. (4.1). As shown in Fig. 4.5, temperature dependence of the tetragonal moduli of rutile-type GeO_2 and MnF_2 is exactly opposite. Namely, it is positive and negative correlation for GeO_2 and MnF_2, respectively. The positive temperature derivative of the moduli of GeO_2 is in concordance with the ultrasonic measurement reported by Wang and Simmons (1973). This result indicates that in the rutile-type structure, if the value of $c_{11} - c_{12}$ becomes larger at higher temperature, the transition pressure must increase, and vice versa. According to a review of Akaogi (1993), many of pressure-induced transitions of minerals with increase in cation coordination number show negative Clapeyron

slopes, whereas the transition without cation coordination change has positive one. The result in this study also satisfies this empirical relation as shown in Fig. 3.11 and 3.14. It can, therefore, be considered that the temperature dependence of the tetragonal moduli directly explain the temperature dependence of the transition pressures and the sign of the Clapeyron slopes. This result implies the following significantly interesting assumption. In a large number of rutile-type materials, it has been known from high-pressure experiments that many of them transform to the $CaCl_2$ form or the fluorite form. We can predict their high-pressure phases by only measurement of temperature dependence of elastic constants at ambient pressure without high-pressure experiments.

4.2 Time evolution of physical quantities

Next, time evolution of several observable quantities during the transition processes is focused on and interpreted from the viewpoint of elastic instability. In Fig. 4.6, the time evolution of B1-type CaO under compression from 125 to 130 GPa at 300 K is described. A sharp exothermic peak with respect to emission of latent heat is observed at ca. 7 ps after the pressure increases to 130 GPa. These results and the evolution of cell lengths mean that the transition begins at the time when the exothermic reaction occurs and has the first-order character. Compared with these quantities, the cell angles seem to change slowly. It is noted that they begin to deviate from the cubic angle 90° and become to be wobbly at ca. 3 ps before the exothermic peak with the transition. This prior behavior of the cell angles can be connected to the elastic instability resulting from the softening of the shear modulus.

In Fig. 4.7, the time evolution of rutile-type MnF_2 under compression from 6.5 to 7 GPa at 300 K is described. An exothermic peak accompanied by the rutile-to-fluorite transition is observed at 18 ps in the evolution of temperature. A peak concerning pressure reduction with the discrete volume reduction is observed at the transition in the evolution of pressure. It seems that these results mean that the transition has the first-order character and is achieved extremely quickly in the MD calculation. However the evolution of cell lengths indicates that the orthorhombic cell deformation begins gradually at 3 ps before the exothermic peak. This prior deformation can be connected to the tetragonal elastic instability and derives the large volume change with thermal reaction.

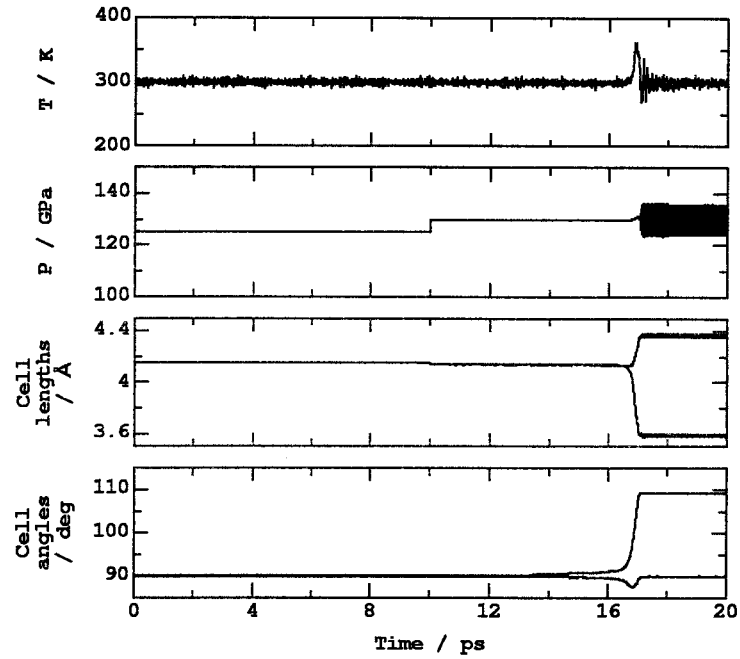

Figure 4.6 Time evolution of several physical quantities of B1-type CaO.

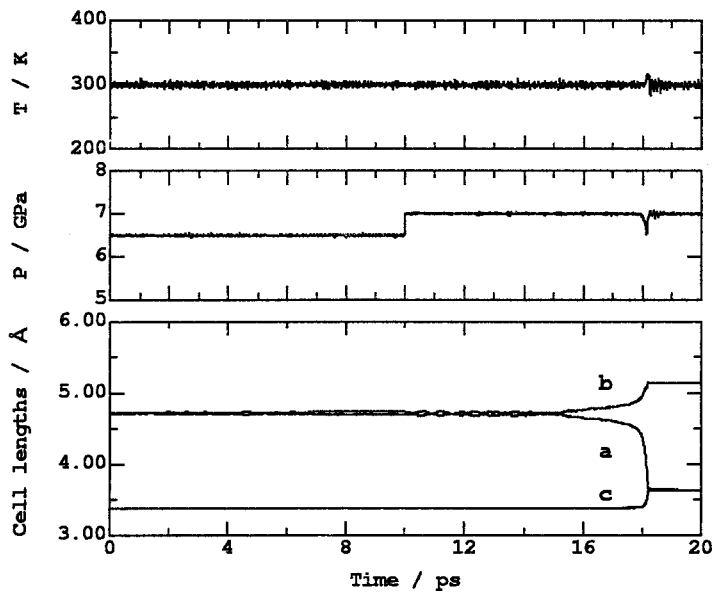

Figure 4.7 Time evolution of temperature, pressure and cell lengths of Rt-type MnF_2.

In Fig. 4.8, the time evolution of quartz-type GeO_2 under compression from 7 to 7.4 GPa at 300 K is described. The evolution of the cell lengths of a and b indicate that the transition begins at ca. 8 ps after the pressure increases to 7.4 GPa. A slight disturbance concerning pressure reduction with the volume reduction with the transition is observed at the transition in the evolution of pressure. However, no temperature fluctuation resulting from the transition is observed in the evolution of temperature. In spite that the transition results from the shear instability, the time evolution of the cell angles shows that their deviations from the hexagonal cell begin at ca. 1 ps later than those of other quantities. Because of this result, Tse and Klug (1991) misread so that the transition originates in the instability in bulk modulus. The changes of all quantities finish at ca. 3 ps after the transition begins. This duration is longer than the former two cases. It is likely that no observation of the latent heat originates in this slow transition process.

In Fig. 4.9, the time evolution of rutile-type GeO_2 under compression from 75 to 80 GPa at 300 K is described. From the evolution of the cell lengths, it is clear that the transition begins as soon as pressure increases to 80 GPa. This behavior with no time difference is different from the former three cases. Moreover, no peak concerning latent heat is observed on the evolution of temperature. These results mean that the transition has the second-order character. It is noted that quite large symmetric fluctuations of a and b lengths whose amplitude reaches 0.02 Å, appears during the transition in the evolution of the cell lengths. This behavior can be connected to the elastic instability resulting from the softening of the tetragonal modulus.

In Fig. 4.10, the time evolution of high-pressure-clinoenstatite-type GeO_2 under compression from 31 to 32 GPa at 300 K is described. An exothermic peak accompanied by the HPCEn-to-X_1 transition is observed at about 3 ps in the evolution of temperature. A peak concerning pressure reduction with the discrete volume reduction is observed at the transition in the evolution of pressure. The time evolution of cell angles indicates that the

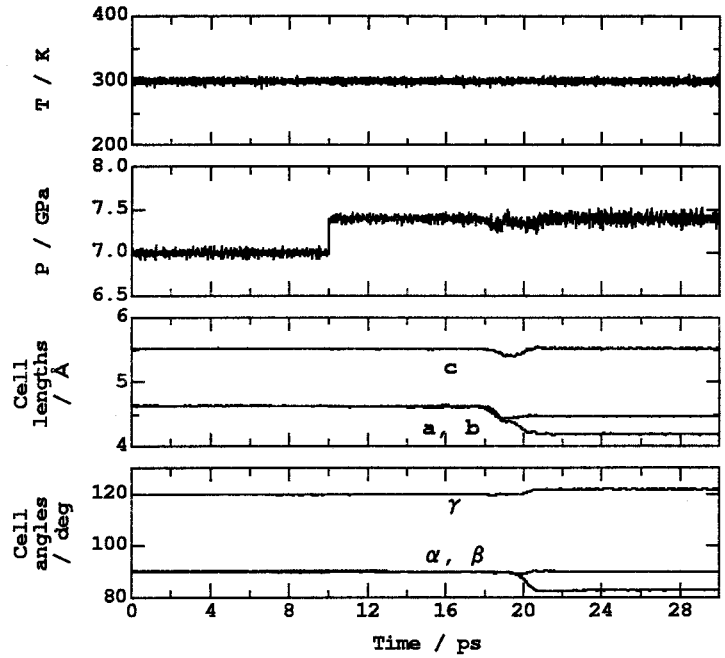

Figure 4.8 Time evolution of temperature, pressure and cell lengths of Qz-type GeO_2.

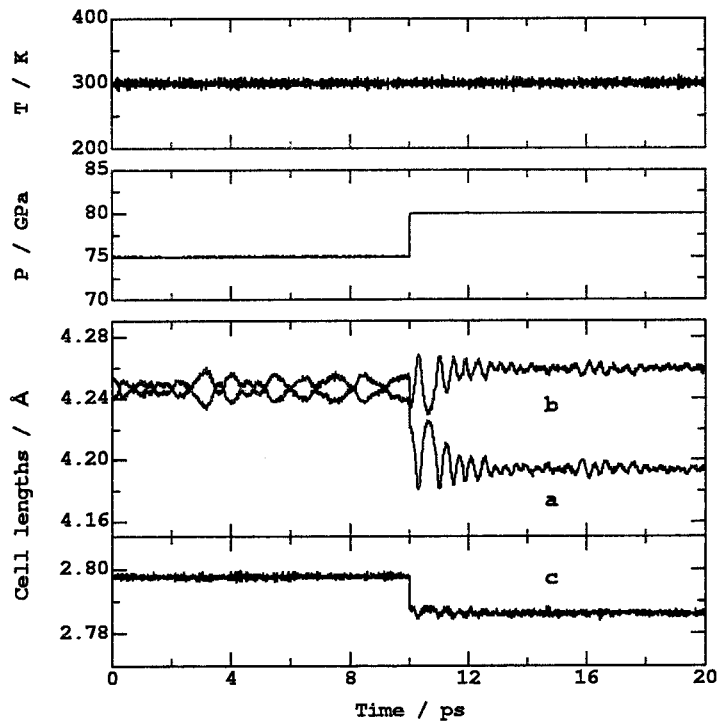

Figure 4.9 Time evolution of temperature, pressure and cell lengths of Rt-type GeO_2.

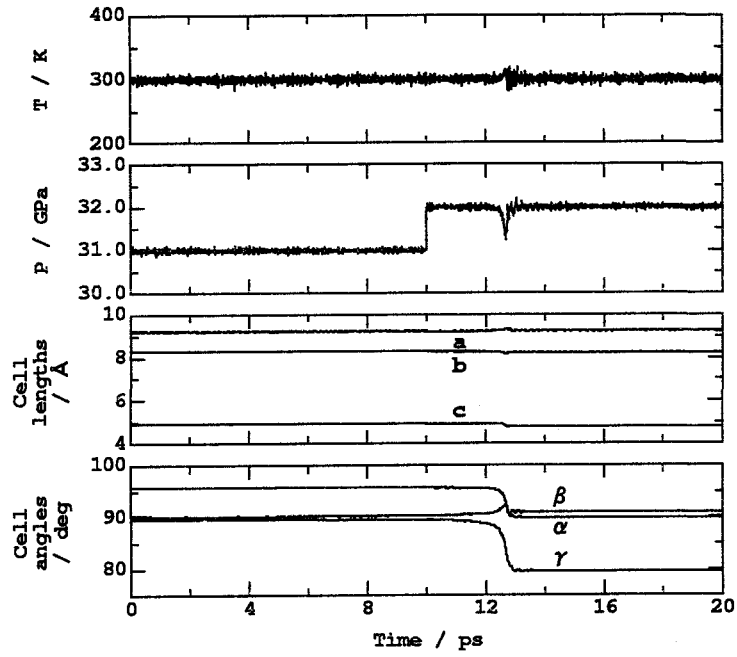

Figure 4.10 Time evolution of temperature, pressure and cell lengths of HPCEn-type $MgGeO_3$.

decrease in γ begins gradually at 2 ps before the exothermic peak. This prior shear deformation corresponds to the slip of oxygen dense planes to hcp shown in Chap. 3, which is the key mechanism in the HPCEn-to-X_1 transition. Although the elastic stability condition for high-pressure-clinoenstatite has never calculated, this indicates that the transition may result from the shear elastic instability.

4.3 Elastic anisotropy

By applying Newton's equation of motion $(\partial\sigma_{ij}/\partial x_j) = \rho(\partial^2 u_i/\partial t^2)$, substituting Hook's law, and utilizing Gauss' theorem, we obtain the so-called Christoffel equation

$$\left|c_{ijkl}n_j n_l - \rho V^2 \delta_{ik}\right| = 0, \tag{4.2}$$

where c_{ijkl}, ρ, V, $\mathbf{n}$ and δ_{ik} are the adiabatic elastic constant tensor, density, elastic wave velocity, the propagation vector of elastic wave and Kronecker delta, respectively. This equation is on the basis of the long-wave approximation used by Born to develop the elastic constants from lattice theory, and the acoustic phonon velocity can be calculated by this eigenequation. The lattice elastic instability reflects this velocity such that stability conditions secure real value of it. Fig. 4.11 shows three elastic wave velocities in B1-type CaO depending on the crystallographic orientation at several pressure conditions. This figure demonstrates that the wave velocities have some dispersion depending on the propagation direction even in the cubic crystal. The compressional (P) wave velocity is fastest along [1 0 0] and increases with pressure, whereas shear (S) wave velocities are slowest between [1 0 0] and [1 1 0] and decrease with pressure. The decrease in S wave velocities in these directions originates in decrease in c_{44} at high-pressure. This result can be considered as another reflection of the lattice shear softening.

The dispersive behavior of wave velocities is related to elastic anisotropy. In the case of the cubic crystal, the anisotropic factor A of the elastic wave velocity can be derived from Eq. (4.2) and is represented as

$$A = \frac{2c_{44} + c_{12}}{c_{11}} - 1. \tag{4.3}$$

If $A = 0$, the lattice is fully isotropic in elasticity. The anisotropy may be connected with the anharmonicity of vibraion potentials of the atoms. Especially, the fact that the P wave velocity is slowest along [1 1 1] indicates that the vibration potential of atoms is

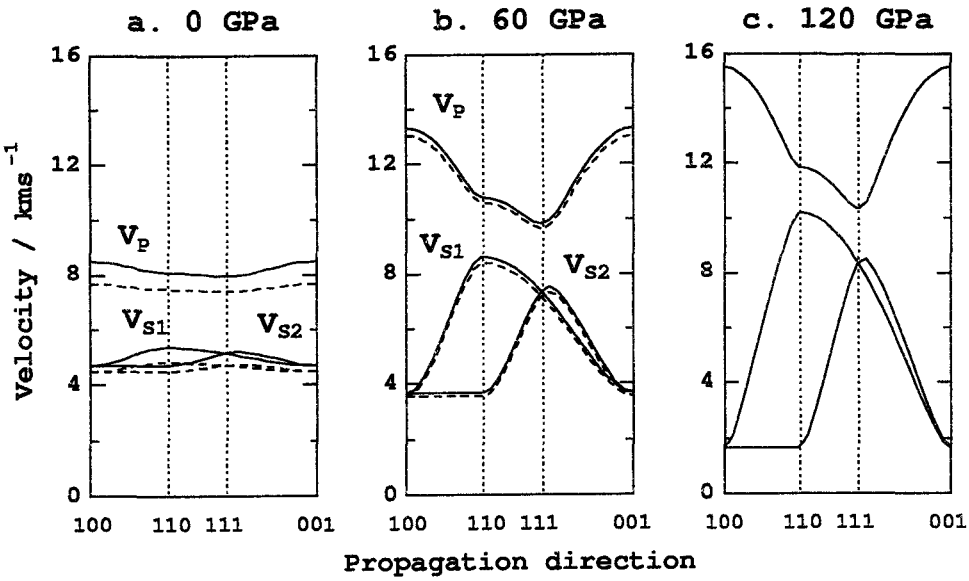

Figure 4.11 The anisotropic elastic wave velocities of B1-type CaO calculated from Eq. (4.2) at 0 (**a**), 60 (**b**) and 120 GPa (**c**). The *solid* and *dashed line* are at 300 and 1000 K, V_P, V_{S1} and V_{S2} indicate wave velocities of a compressional (longitudinal) and two polarized shear waves, respectively. These are mutually orthogonal.

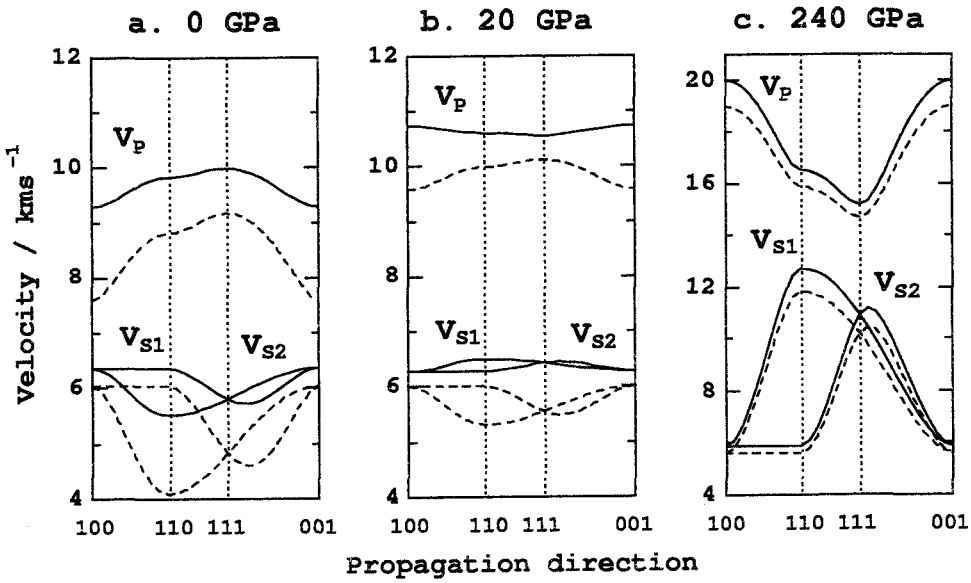

Figure 4.12 The anisotropic elastic wave velocities of B1-type MgO calculated from Eq. (4.2) at 0 (**a**), 20 (**b**) and 240 GPa (**c**). The *solid* and *dashed line* are at 300 and 2000 K, respectively. V_P, V_{S1} and V_{S2} indicate wave velocities of a compressional (longitudinal) and two polarized shear waves, respectively. These are mutually orthogonal.

flatter along this direction compared to other directions. The estimated A of CaO at 300 K decreases from -18% at ambient pressure to -84% at 130 GPa, which means that the anisotropy at 130 GPa becomes 4.6 times larger than it at ambient pressure. From this result, it is assumed that the atomic vibration strongly elongates along [1 1 1] at high pressures. This dynamical picture is completely consistent with the structural changes at the B1-B2 transition shown in Fig. 3.5. As shown by the dashed lines in Fig. 4.11, temperature functions as decreasing anisotropy although its effect seems not to be large.

The calculated elastic wave velocities of MgO at 300 and 2000 K are shown in Fig. 4.12. Although the P wave velocity along [1 0 0] increases with pressure as well as CaO, S wave velocities along [1 0 0] are insensitive to pressure owing to insensitivity of c_{44}. It is noted that in contrast to CaO, the P wave is fastest along [1 1 1] (positive A) at 0 GPa (Fig. 4.12a). With increase pressure under 300 K, anisotropy decreases and almost vanishes at 20 GPa (Fig. 4.12b). Upon further compression, the A changes to negative and its magnitude becomes large (Fig. 4.12c). This interesting result is in agreement with the very recent high-pressure Brillouin scattering measurement by Sinogeikin and Bass (1999). They reported that the acoustic anisotropy decreased with pressure, with MgO becoming isotropic at ca. 21.5 GPa. The result also agree well with the pseudopotential calculation by Karki et al. (1997). The change of sign of A can be connected to the variation of the anharmonicity of the atomic vibrations. We can expect that at ambient pressure, MgO has also macroscopically different dynamical or mechanical properties (e.g. rheology, deformation) from CaO.

Fig. 4.12 indicates that temperature effect enlarges A at 0 GPa, whereas it reduces A at 240 GPa. Temperature effect on elasticity reverses itself with pressure, although it becomes smaller with pressure. Namely, with increasing temperature, the anisotropy increases in the positive A region and decreases in the negative A region. The pressure variation of A are shown in Fig. 4.13. These results have potentially important impli-

cation for the interpretation of seismological observations of the anisotropy in terms of flow in the upper and lower mantle (Tanimoto and Anderson 1984, Dziewonski and Anderson 1981). Karki et al. stated from their static calculations that MgO itself was not relevant for interpreting observation of upper mantle anisotropy since MgO is relatively isotropic in the upper mantle pressure region (~25 GPa). However, the present results indicate in this pressure region, anisotropy considerably depends on not only pressure but also temperature such that $|dA/dP|$ becomes larger at high temperature. Therefore, the anisotropy of MgO is considerably large under high temperature and low pressure condition. These means MgO is not unsuitable for a possible candidate of the upper mantle anisotropy. However, it is unlikely that MgO is the origin of the lower mantle isotropy since the anisotropy rapidly increases under lower mantle pressure (25~135 GPa) even at 2000 K. Anyway, these results clearly demonstrate that the anisotropy of minerals under mantle conditions may differ qualitatively from that an ambient conditions.

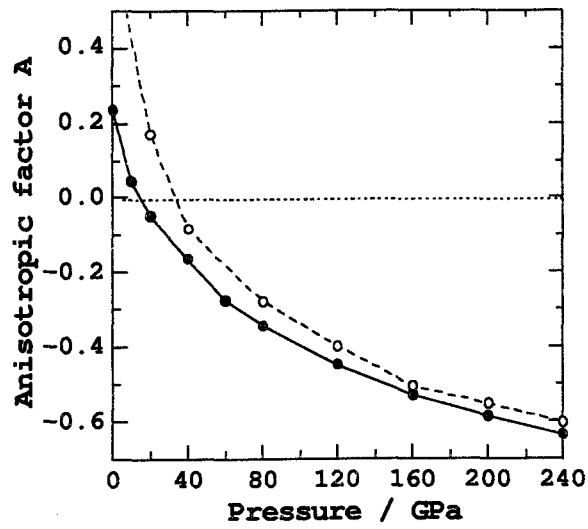

Figure 4.13 The pressure variation of the anisotropic factor of MgO. The *filled* and *open circles* are at 300 and 2000 K, respectively.

In Fig. 4.14, orientation depending wave velocities of rutile-type GeO_2 are indicated. The anisotropy is relatively small at ambient pressure and grows up to the positive direction with pressure. Especially it along [1 1 0] has largest pressure dependence and the S_2 wave velocity along [1 1 0] decreases toward zero with respect to the transition to the $CaCl_2$-type phase. Reduction of velocity of this wave may include condensation of the B_{1g} libration of the octahedra columns. Elastic instability can also be connected to anomaly of the shear wave velocity in the case of rutile. In addition, the P wave is fastest along [1 1 0] under high pressure although it is fastest along [1 0 0] at ambient pressure. This change of the elastic property with pressure is also interesting.

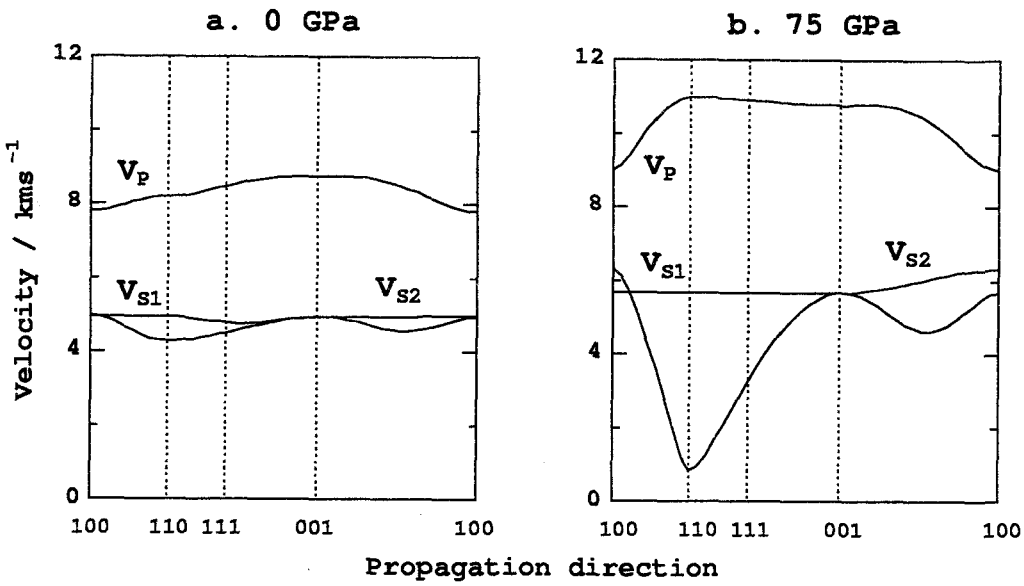

Figure 4.14 The anisotropic elastic wave velocities of rutile-type GeO_2 calculated from Eq. (4.2) at 0 (**a**) and 75 GPa (**b**). V_P, V_{S1} and V_{S2} indicate wave velocities of a compressional (londitudinal) and two polarized shear waves, respectively.

Isotropic wave velocities of MgO

Temperature and pressure dependence of density and isotropic wave velocities of MgO is substantially important for direct comparison with the seismological observations of the

Earth's lower mantle. Isotropic wave velocities which correspond to velocities in isotropic aggregate of crystals can be evaluated using density ρ, bulk K and shear G moduli as follows,

$$v_P = \sqrt{\frac{K + (4/3)G}{\rho}} \quad \text{and} \quad v_S = \sqrt{\frac{G}{\rho}}, \tag{4.4}$$

where v_P and v_S are isotropic P and S wave velocities, respectively. In Fig. 4.15, the calculated density and velocities of MgO are shown as a function of depth of the Earth compared with the seismologically derived ones of the lower mantle (Dziewonski and Anderson 1981) and the experimentally observed velocities at ambient condition (Sinogeikin and Bass 1999). This figure indicates that the velocities at ambient condition agree well with the experimental results, and the temperature dependence of the gradient of the velocities seems not to be negligible up to about 1500 km depth. The gradients of the calculated quantities at 2000 K which is the typical geotherm assumed in the lower mantle agree quite well with the seismological observations although absolute values are smaller. This discrepancy may result from existence of heavy Fe ion. If substituting Mg of 10% for Fe, density will become about 1.1 times larger.

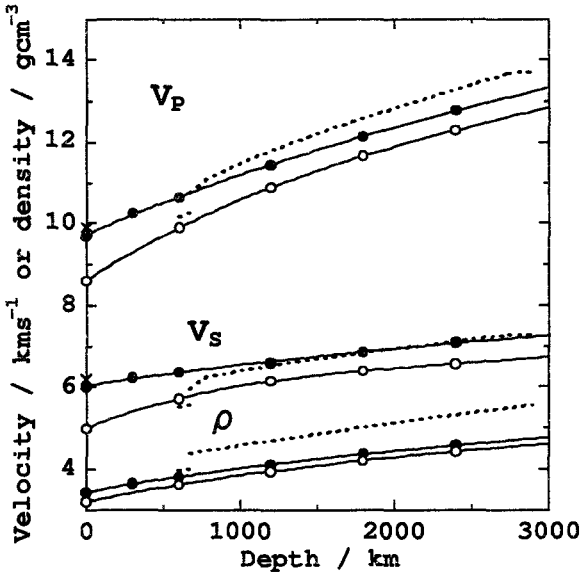

Figure 4.15 The density and velocities of MgO at 300 K (*filled circles*) and 2000 K (*open circles*) compared with the seismologically derived ones (*dotted curves*). The observed velocities of MgO at ambient condition are additionally plotted by *crosses*.

4.4 Summary and discussion

- On the basis of the elastic lattice theory, elastic stability conditions are calculated. It is likely that the pressure-induced transitions appeared in the MD calculations of perfect defect-free crystals must be accompanied by elastic instability. The calculated time evolution of physical quantities can be interpreted by corresponding instability. Elastic instability can be considered as the limit of metastability in supercompression/decompression. This indicates that the energy barrier for the transition itself decreases toward zero at the calculated transition pressure. It can be called the spinodal.

- The successful reproductions of the B1-B2 and the rutile-fluorite transition with no atomic diffusion indicate that elastic instability is fundamentally important mechanisms of the transitions although other thermodynamical factors (defect, impurity, temperature and pressure heterogeneity, etc.) clearly contribute to decrease the hysteresis. If under thermally underactive condition, the pressure-induced elastic instability must be observed in the real system. The pressure-induced amorphization of quartz is considered as one of the examples.

- The second-order rutile-$CaCl_2$ transition is also accompanied by the elastic instability. It may be a typical case that the elastic instability is actually observable, and can be connected with the pressure-induced ferroelastic transition.

- The elastic anisotropy strongly depends on pressure even in cubic crystals. The growth of the anisotropy with pressure leads to anomaly of the shear wave velocity. This shear wave anomaly corresponds to elastic instability. The anisotropy may be related to the anharmonic thermal vibration of atoms

and then the atomic pathway in the transition. By means of MD method, mechanism of high-pressure transitions can be studied from not only structural but also dynamical points of view.

Chapter 5

Effect of nonhydrostaticity on elasticity and transitions

5.1 Effect of nonhydrostaticity on transitions

TABLE XI Calculated structures in several hydrostatic and nonhydrostatic runs with RCNs of Ge-O and O-O pairs. The pressures at 0 GPa correspond to a system decompressed from 7 GPa with the indicated shear stress. In the *second column*, shear stresses given as *three figures in parentheses* represent the σ_4, σ_5 and σ_6 component of the stress, respectively. The *last column* lists the system's phase in the corresponding pressure condition, where O-FCC means the structure having oxygen fcc sublattice.

P (GPa)	σ (GPa)	Ge-O coordination	O-O coordination	Phase
7.4	(0,0,0)	5.3	12	O-FCC
70	(0,0,0)	6	12	O-FCC
6	(2,0,0)	5.3	12	O-FCC
	(−2,0,0)	5.3	12	O-FCC
	(0,2,0)	5.3	12	O-FCC
	(0,−2,0)	5.6	12	O-FCC
	(0,0,2)	5.3	12	O-FCC
	(0,0,−2)	5.4	12	O-FCC
0	(0,0,6)	6	11.4	Rt+defects

It is desirable to eliminate, to reduce or to control the pressure anisotropy and inhomogeneity in high-pressure experiment. However, these are quite difficult from technological aspects. Therefore effect of nonhydrostaticity on the transition has been hardly studied experimentally in spite of its importance. The nonhydrostaticity related to elastic instability is likely to affect the corresponding transition. By means of the constant stress MD, each component in the stress tensor calculated from Eq. (2.19), can be controlled

independently at an arbitrary value. Firstly, nonhydrostatic effect on the transition of quartz is discussed. Badro et al. (1996) studied the transition of quartz under uniaxial nonhydrostatic conditions using MD method, whereas effect of shear stressed condition is more interesting since the shear instability causes the transition of quartz. The results calculated under several shear stressed conditions are listed in Table XI. When shear stress reached 2 GPa, regardless of any shear stress component, the transition of quartz appeared. This result indicates that the transition pressure can be effectively lowered under shear nonhydrostatic conditions. Here any shear stress can cause instability since three types of orientation exist in structural modification with respect to the threefold axis of the quartz lattice. In the case of quartz and CaO, it can be considered that shear stress lowers the transition pressure since the shear elastic instability causes their transitions.

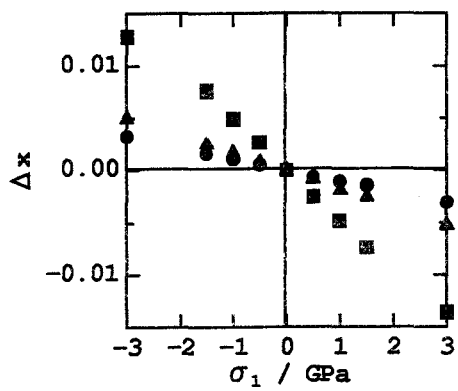

Figure 5.1 σ_1 dependence of the difference between x and y coordinates of the oxygen atom position Δx. The *circle*, *triangle* and *square* indicate the result at 0, 30 and 60 GPa, respectively.

Since the rutile-to-$CaCl_2$ transition originates from tetragonal elastic instability, uniaxal stress is likely to affect the transition. The $CaCl_2$ structure is described by the

rotation of GeO_6 octahedra column around the twofold axis of the rutile structure as noted in Chap. 3. This can be characterized by the difference between x and y coordinates of the oxygen atom position Δx, which is zero in the rutile structure. In Fig. 5.1, the relation between added σ_1 and corresponding Δx at several pressures are plotted. This figure shows that Δx linearly correlates to σ_1 and the orthorhombic distortion must be accompanied by rotation of the octahedra column. The transition can therefore occur even at zero pressure by uniaxial stress, and the effect of nonhydrostaticity on the transition becomes larger under higher pressure. This indicates that uniaxial nonhydrostatic conditions effectively lowers the transition pressure of the rutile-$CaCl_2$ transition. Moreover this transition is quite sensitive to uniaxial nonhydrostaticity.

Haines et al. (1998) estimated the transition pressure at 26.7 GPa, which is quite lower pressure than the calculated result, 80 GPa (Chap. 3). They used helium as a pressure-transmitting medium to keep hydrostaticity under high pressure. Helium is considered as good hydrostatic medium since it remains a very weak solid up to 120 GPa after solidification at 11 GPa (Loubeyre 1996). In spite of that, since the transition is considerably sensitive to hydrostaticity, it is no wonder that they would have underestimated the transition pressure. However, the discrepancy of the transition pressures is too large to be attributed to nonhydrostaticity in the experiment. This rather originates from the lack of quantitative reproducibility of the used interatomic potential for their elasticity of rutile-type GeO_2. The calculated tetragonal modulus at ambient condition, 230 GPa is quite larger than the observed value, 149 GPa. As noted in Chap. 2, the interatomic potential of GeO_2 was determined by the traditional empirical procedure. By this procedure, it is difficult to construct the effective potential having not only qualitative but also quantitative reproducibility of elastic constants. It is clear that the more sophisticated way using *ab initio* calculations as well as for alkaline-earth oxides is necessary. Although such approach is in principle desirable, there are computational difficulties left for the low

symmetric structures.

5.2 Stress-induced transitions

Structural changes in α-quartz under uniaxially stressed nonhydrostaic compression was simulated by Badro et al. (1996), who reported that a new crystalline phase, where all silicon atoms were in fivefold-coordination, appeared under a positive uniaxial stress along the c axis. However behaviors under shear stressed compression is more interesting because of the shear instabilization of quartz with pressure. An interesting result was observed in the case of decompression on imposition of positive and negative σ_6 from 7 GPa. The quartz-type structure transformed to a particular structure that is quite similar to the rutile-type structure (Table XI). A snapshot of this structure and calculated RCNs of Ge-O and O-O pairs in the structure are shown in Fig. 5.2 and Fig. 5.3, respectively. The germanium coordination and the anion-anion coordination is 6- and 11-fold, respectively, which is characteristic of the rutile structure. This structure contains the

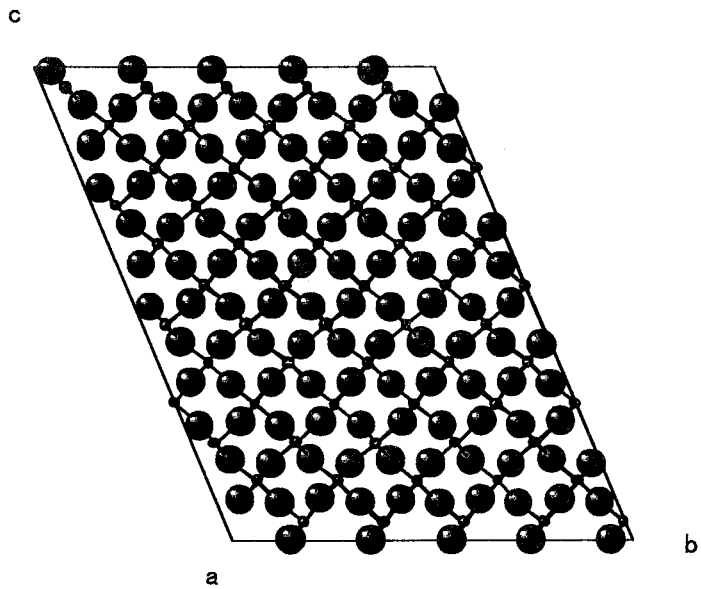

Figure 5.2 Snapshots of the calculated rutile-like structure at ambient condition after decompression with positive σ_{xy} from 7 GPa (**b**). This figure is a projection along the quartz a axis and extremely similar to the rutile-type structure. The *small* and the *large spheres* indicate germanium and oxygen atoms, respectively.

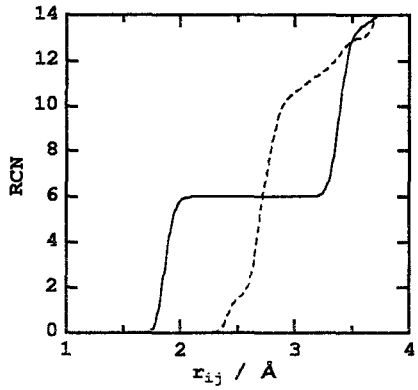

Figure 5.3 Running coordination number of Ge-O (*solid line*) and O-O (*dashed line*) pairs in the rutile-like structure after decompression with $\sigma_6 = 6$ GPa from 7 GPa.

corner-linked GeO_6 octahedra and the edge-sharing octahedra chain as well as the rutile structure. However, the broader RCN of the O-O pair indicates that the oxygen arrangement is somewhat disorder and this rutile-like structure shows some error in the periodicity of corner-linkage and cannot therefore be recognized as the perfect rutile-type crystal. No transition from this structure occurred on eliminating the stress. This is fully quenchable as to pressure and stress.

In Fig 5.4, the formation process of GeO_6 octahedron is extracted. The formation process of GeO_6 octahedron in this transition is different from the transitions under the hydrostatic and other nonhydrostatic conditions given above, namely the fcc oxygen sublattice is not formed. It is, however, noted that this transformation process contains only no atomic diffusion. Although it is generally believed that the quartz-to-rutile transition is the so-called reconstructive transition accompanied by atomic diffusions, if the transition is subjected to the path shown above, the main part of the quartz-to-rutile transition can be achieved with smaller displacement of ions than is associated with the word "reconstructive". However, to construct the perfect rutile-type structure from this half-finished stage, other processes are needed.

Another interesting point of these calculations is a special crystallographic orientation relation between the original quartz-type lattice and the newly appeared rutile-like

structure. Fig. 5.2 shows projections to a normal plane to the quartz-type a axis. Therefore, a topotaxial relation such that $(100)_{Qz}$ // $(001)_{Rt}$ exists between two structure.

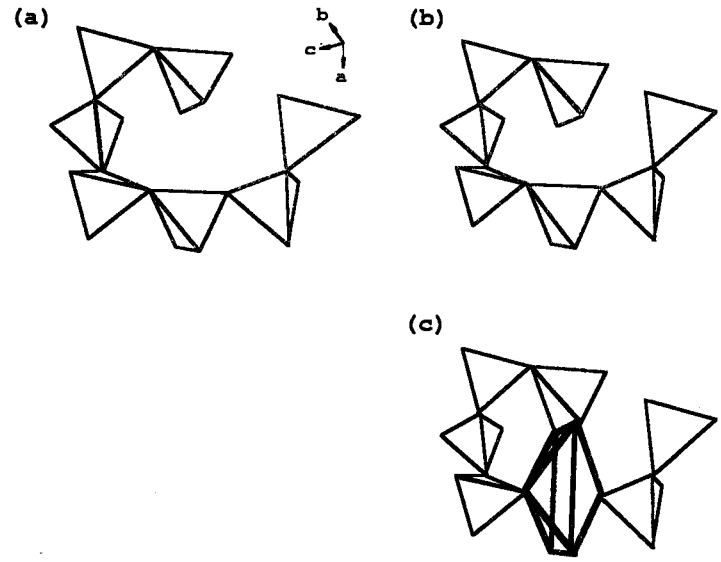

Figure 5.4 The schematic pictures of the formation of the distorted GeO_6 octahedron from quartz-type GeO_4 network by shear stress σ_{xy}. The quartz-type network of GeO_4 tetrahedra at ambient pressure (**a**), the deformed network by application of σ_{xy} (**b**) and the same network as **b** except for the *bold line* indicating a newly formed octahedron (**c**). The quartz-type lattice vectors indicated in **a** shows that the a direction of quartz corresponds to the chain direction of GeO_6 octahedra which is c direction of the rutile-type.

We can interpret that the calculated path of displacements of ions in this transition indicates a possible mechanism of nucleation of the rutile-type phase at the quartz-to-rutile transition. Wolf et al. (1992), using the high-resolution electron microscope, observed that the rutile-type structured crystallite existed in a recovered sample of pressure-induced amorphous GeO_2. Their observation implies that the quartz-to-rutile transition is not always prohibited under thermally underactive condition such as room temperature. If generating some internal stresses during compression and decompression, the proposed quartz-to-rutile transition process might take place in the real system. Once the transition

occurs in a locally stress concentrated part of a sample, stresses around this part may be released. Therefore the crystallite of the rutile-type phase can not grow up to an X-ray coherent size. Only one stress component was applied in each run of the present study. The value of stress needed for the transformation would change under more complicated nonhydrostatic conditions.

As discussed in Chap. 3, the calculated high-pressure state of high-pressure-clinoenstatite-type $MgGeO_3$, X_1 has the incomplete oxygen packing between fcc and hcp. If the black arrow in Fig. 3.9 becomes perpendicular to the (1 0 0) plane of the HPCEn lattice, the oxygen packing becomes hcp. From the figure, this modification is expected by the slips of the oxygen dense planes every other layer (Fig. 5.5). Such lattice deformation can be

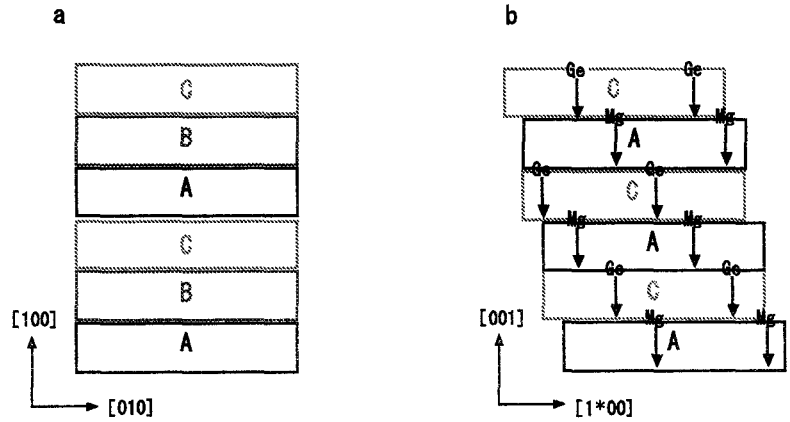

Figure 5.5 The schematic picture of the transition mechanism of the oxygen packing from ccp (**a**) to hcp (**b**). The crystallographic orientation of HPCEn and Ilm are described in **a** and **b**, respectively. Arrows in **b** indicates the cation diffusion path in the calculated X_1-to-X_2 transition.

achieved by external shear stress σ_4. Over σ_4 = 14 GPa, the shear-induced transition from X_1 to a quenchable state occurred at 300 K and 32 GPa with oxygen packing change to hcp as expected. In this process, cooperative diffusions of some cations to adjacent void space occurred. The cation diffusion path is shown in Fig. 5.5b. The result that the stress needed for the transition is comparably large may originate in the high energy barrier of the diffusion.

The calculated product could not identified with any known structure and then this structure is called X_2 whose structure is shown in Fig. 5.6. However, this structure is quite interesting with respect to similarity to the known corundum, ilmenite and $LiNbO_3$ structures and its quenchable character. The comparison of the X_2 with other sesquioxide ABO_3 structures is shown in Fig. 5.7. The basic structure contains the almost ideal hcp oxygen sublattice with cations defining octahedral layers. The occupancy of each layer is identical in the corundum structure ($R\bar{3}c$) (Fig. 5.7b). When two different ions form a ternary ABO_3 structure such as that of the ilmenite structure ($R\bar{3}$), they order in alternate layers (Fig. 5.7c). A different pattern of occupancy of octahedral sites in an hcp

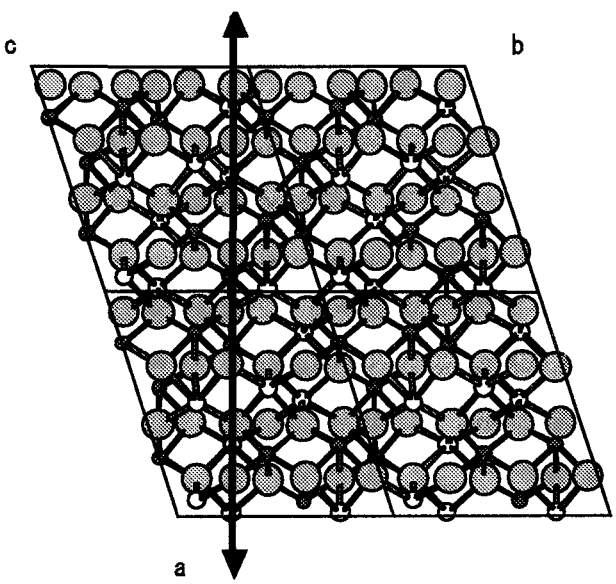

Figure 5.6 The structure of the calculated shear-induced products under σ_4 applied conditions. The *large circle* indicates oxygen anion, and the *small gray* and *white* circles are germanium and magnesium cations, respectively. The arrow means stacking orientations of the dense plane of oxygen ions; the hcp packing. The cation-oxygen bonds are drawn for guides to eye. These figures are projections along [0 0 1] of the HPCEn-type structure.

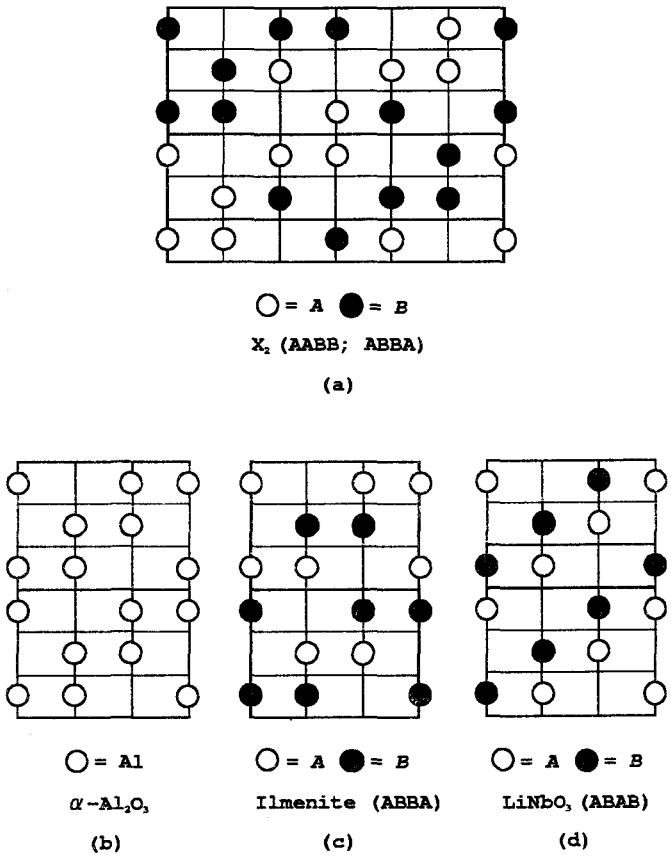

Figure 5.7 The comparison of the structure of X_2 (**a**) with other sesquioxide ABO_3 structures showing the disordered (corundum) ($R\bar{3}c$) (**b**) and the two ordered subfamilies of structures: ilmenite ($R\bar{3}$) (**c**) and lithium niobate ($R3c$) (**d**). The horizontal lines represent the close-packed oxygen planes. The cations occupy the octahedral holes in them.

oxygen array is the lithium niobate structure ($R3c$) (Fig. 5.7d). Although X_2 has the hcp oxygen packing, the cation ordering pattern in it is not the same as the other two ABO_3 structure. X_2 is also be quenchable up to ambient pressure as well as ilmenite and $LiNbO_3$. The large void bands and adjacent cation densely packed bands which cause to severely distort the oxygen lattice in X_1 vanish by the cations diffusion. It can be considered that this is the origin of the quenchable nature of X_2.

In spite of the mistake in the cation distribution in X_2, the transition to X_2 is quite interesting concerning the following respect. If X_2 is forcibly recognized as corundum or ilmenite, the crystallographic orientation relation between high-pressure-clinoenstatite

and X_2 can be represented as

$$[1\ 0\ 0\ ]_{\mathrm{HPCEn}} \rightarrow [0\ 0\ 1]_{\mathrm{Ilm}} \text{ and } [0\ 1\ 0\ ]_{\mathrm{HPCEn}} \rightarrow [1^*\ 0\ 0]_{\mathrm{Ilm}}.$$

Therefore, $(0\ 0\ 0\ 1)_{\mathrm{Ilm}}$ and $(1\ 0\ \bar{1}\ 0)_{\mathrm{Ilm}}$ are parallel to $(1\ 0\ 0)_{\mathrm{HPCEn}}$ and $(0\ 1\ 0)_{\mathrm{HPCEn}}$, respectively. This relation is in completely agreement with an observation in a meteorite by Tomioka and Fujino (1999). They discovered the same crystallographic orientation relation between silicate clinoenstatite and akimotoite in the shock-metamorphosed Tenham chondrite, where akimotoite is a mineralogical name of a kind of iron-bearing silicate ilmenite. Actually, the shock-metamorphic rock must have undergone a large stress field and high temperature. Tomioka and Fujino inferred that peak temperature generated by shock events in Tenham was higher than 2000°C. In Table XII, the calculated result of the temperature effect on the pressure and stress needed for the X_1-to-X_2 transition. This table indicates thermal energy significantly reduces the transition pressure and stress, and the needed nonhydrostaticity decreases with heating. This may result from thermal energy activates the cation motion for the diffusion. Therefore, it is not curious that the clinoenstatite transforms to ilmenite along this mechanism at high temperature. Although X_2 has no complete cation distribution, the successive clinoenstatite-X_1-X_2 transition is likely to be strongly related to the observed clinoenstyatite-to-akimotoite transition.

TABLE XII Calculated products under σ_4 applied nonhydrostatic runs at several temperature and pressure conditions. X_2 indicates the new shear-induced structure.

T (K)	P (GPa)	σ_4 (GPa)	σ_4/P	product
300	32	12	0.375	X_1
		14	0.438	X_2
650	30	8	0.267	X_1
		10	0.333	X_2
1000	27	4	0.148	X_1
		6	0.222	X_2

Conclusions

In this thesis, it has been shown that the compressional mechanisms and pressure-induced structural transitions of several oxide minerals are correctly reproduced by means of computational methods based on molecular dynamics.

To calculate elastic properties of cubic crystals accurately, new computation techniques QEq-MD have been developed. And to construct model interatomic potentials having high reliability in the wide pressure range, sophisticated techniques using energy surfaces of FP-LMTO based on density-functional theory have been applied for alkaline-earth oxides. Quite high efficiency of these techniques has been shown. Interatomic potentials for other materials can reproduce crystal structures of many polymorphs although they were simple empirical two-body potentials.

The elastic stability conditions have been calculated on the basis of Born's stability conditions. It is remarkable that the elastic instability performs a fundamental role in the B1-B2, pressure-induced amorphization, rutile-$CaCl_2$ and rutile-fluorite transitions although in fact, thermodynamical factors contribute their kinetics. Moreover it has been shown that the dynamics of the transitions such as the transition pressures can be sensitively influenced by nonhydrostaticity imposed stresses related to instability.

It has been shown that the transitions which do not reproduce on hydrostatic compression appear under sher stressed conditions. The structural relations between low- and high-pressure phases seems to be comparably simple even in the case of the reconstructive transitions. We can consider that the changes of oxygen packing with coordination

increase are important in high-pressure structural transitions and stresses which help the slip of atom dense planes sensitively influence the dynamics of the transitions.

Appendix A

Summary of the Earth's interior

seismic discontinuity	phase	chemical discontinuity
	CRUST olivine, pyroxene, plagioclase, quartz, carbonates, hydrous phases	Si-rich
10-50 km, 1.5-2.5 GPa	⇓	Mohorovicic discontinuity (Moho)
	UPPER MANTLE pyroxene, olivine, garnet, $MgAl_2SiO_4$-based spinel, amphibole	Mg,Fe-rich
400 km 15 GPa	⇓ **TRANSITION ZONE** $(Mg,Fe)_2SiO_4$ spinel, garnet, minor phases	
660 km 25 GPa	⇓ **LOWER MANTLE** $(Mg,Fe)SiO_3$, $CaSiO_3$ perovskite, $(Mg,Fe)O$ magesiowüstite, SiO_2 stishovite, minor phases	
2900 km 130 GPa	⇓ **OUTER CORE** liquid Fe, Ni alloy with light element	Definite chemical discontinuity Fe alloy
5200 km 300 GPa	⇓ **INNER CORE** solid Fe, Ni alloy with light element	
6400 km 360 GPa		

Appendix B

Phase diagrams

Experimentally constructed T-P phase equilibrium diagrams of GeO_2 and $MgGeO_3$ are represented. Those of MgO and CaO are not represented since no observations about phase diagrams of MgO and CaO exist.

GeO_2 :

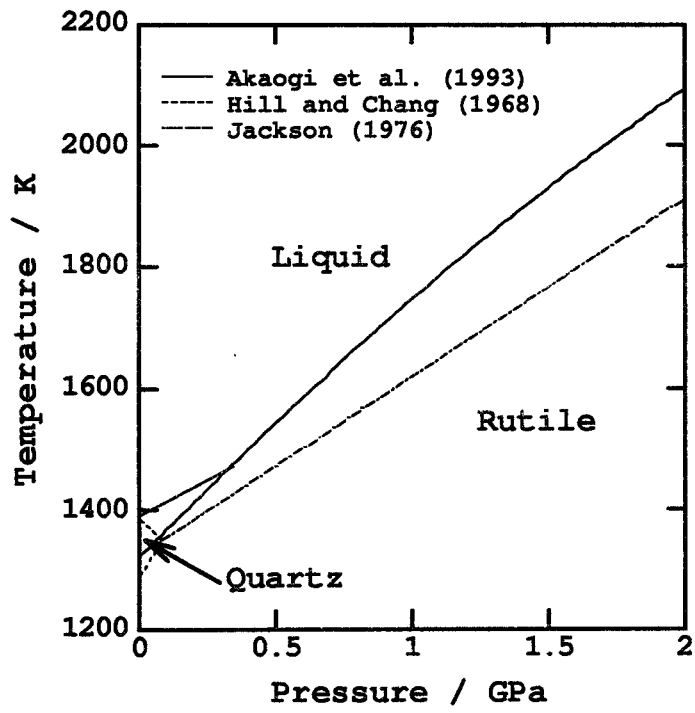

Figure B.1 The phase diagram of GeO_2 extracted from several experimental results.

$MgGeO_3$:

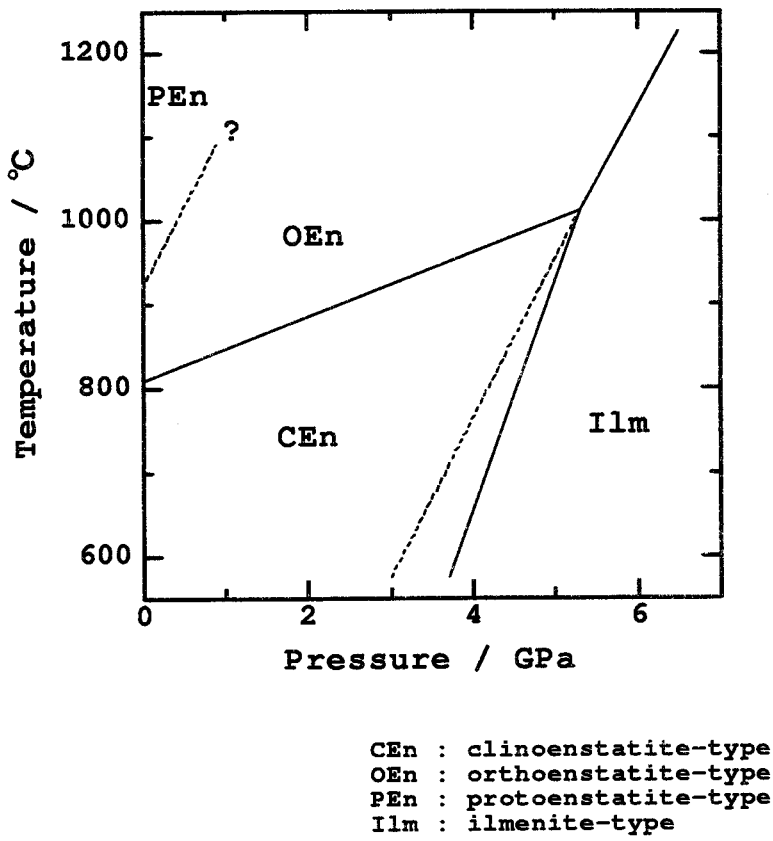

Figure B.2 The phase diagram of $MgGeO_3$ extracted from Ozima and Akimoto (1983).

Appendix C

Dynamical fluctuating charge model

QEq-MD method needs computational time in proportin to N^3 order. To avoid this difficulty, the following dynamical fluctuation model proposed by Rick et al. (1994) may be useful within the molecular dynamics. The way to treat the charge neutrality constraint is to use the method of undetermined multipliers to enforce the constraint. The Lagrangian is

$$L = \sum_i^N \frac{1}{2} m_i \dot{r}_i^2 + \sum_i^N \frac{1}{2} M_q \dot{q}_i^2 - U(\mathbf{r}, \mathbf{q}) - \lambda \sum_i q_i, \tag{C.1}$$

where m_i is the mass of i-th atom and M_i is a fictitious charge "mass," which has an unit of energy time^2/charge^2, the λ are Lagrange multipliers and U is total potential energy. The nuclear degrees of freedom evolve according to Newton's equation

$$m_i \ddot{r}_i = -\frac{\partial U(\mathbf{r}, \mathbf{q})}{\partial r_i} \tag{C.2}$$

and the set of charges evolve in time according to

$$M_i \ddot{q}_i = -\frac{\partial U(\mathbf{r}, \mathbf{q})}{\partial q_i} - \lambda = -\chi_i - \lambda, \tag{C.3}$$

where λ is given by the charge neutrality constraint $\sum_i^N q_i = 0$ and χ_i is the electronegativity of atom i defined by Eq. (2.23). It should be noted that if the total charge is a constant of the motion, then

$$\sum_i^N \ddot{q} = 0. \tag{C.4}$$

Substitution of Eq. (C.3) into the above equation yields,

$$\lambda = -\frac{1}{N} \sum_i^N \chi_i, \tag{C.5}$$

where λ is equal to the negative of the average of the system's total electronegativity. Substitution of Eq. (C.5) into the equation of motion for the charges gives

$$M_i\ddot{q}_i = -\frac{1}{N}\sum_j^N(\chi_i - \chi_j). \tag{C.6}$$

The force on the charge is simply the difference between the average electronegativity and the instantaneous electronegativity at a site. For example, if the electronegativity is greater than the average, then the force acts to decrease the charge until the electronegativities are all equal. This can be done by simply using the extended Lagrangian method to derive the equations of motion for Hamiltonians which depend on auxiliary degrees of freedom (Parrinello and Rahman 1980, 1981).

The charge mass M_q, a fictitious quantity, should be chosen to be small enough to guarantee that the charges readjust very rapidly to changes in the nuclear degrees of freedom. This is equivalent to the Born-Oppenheimer adiabatic separation between the electronic and nuclear degrees of freedom. The charge kinetic energies should remain at low temperature, since they are to be near the values which minimize the electrostatic energy. This can be achieved by Nosé's thermostat. A simplified version of this method using the scaling method can be also easily achieved.

Appendix D

Pressure dependence of band gaps in MgO and CaO

Pressure effect on the electronic properties has been long interesting. In Table XIII, energy gaps for B1-type MgO and CaO at several pressures calculated by FP-LMTO method are listed. The energy gap increases with pressure in MgO, whereas it decreases with pressure in CaO. However, as well-known, the local-density approximation largely underestimates energy gap about 40% owing to underestimation of the exchange potential for occupied bands and increase in their eigenvalues. There is no guarantee that even position of band gap is reproduced correctly (Kotani 1994).

	Pressure	Direct gap			Indirect gap
Method	(GPa)	Γ	X	L	Γ-X
MgO					
Exp[a]	0	7.833			
FPLMTO-GGA	2.7	4.73	10.39	8.55	
(This study)	104.4	8.55	11.08	11.23	
	222.9	11.29	11.26	12.89	9.21
FLAPW-LDA[b]	0	4.68	9.78	8.50	
TBLMTO-EXX[c]	0	7.77	17.56	12.56	
Hartree-Fock[d]	0	25.3	17.0	21.4	
CaO					
Exp[a]	0	7.09			
FPLMTO-GGA	0.2	5.25	4.38	8.83	3.97
(This study)	69.0	7.40	3.88	10.89	3.61
	160.5	7.53	3.29	12.17	3.22
FLAPW-LDA[b]	1	5.20	3.82	8.59	3.58
TBLMTO-EXX[c]	0	7.72	9.32	11.4	9.08
Hartree-Fock[d]	0	15.8	19.9	21.9	18.7

TABLE XIII Energy gaps at high-symmetry points for B1-type MgO and CaO at several pressures. TBLMTO-EXX stands for tight-binding LMTO method with the exact exchange potential. Unit of the values of energy gaps is given in eV.

[a] Whited et al. (1973)
[b] Mehl et al. (1988)
[c] Kotani (1994)
[c] Pandey et al. (1991)

Acknowledgements

I am indebted to Professor Takamitsu Yamanaka for continual guidance and supervising the present thesis. First of all I would like to thank him. I wish to express my sincere gratitude to Professor Akira Yoshiasa who continues to give me quite impressive and exciting discussions. I am grateful to Professor Katsuyuki Kawamura for helpful discussions, guidance and encouragement and for providing me with the original MD code. The QEq-MD code is developed by modifying it. I also thank Professor Masanori Matsui who guided me carefully in the use of the static-lattice-energy-minimization program WMIN. He also gives me continuasly impressive and helpful comments. I wish to thank Dr. Takao Kotani who not only helped me use the FP-LMTO electronic structure calculation, but always encouraged me. Furthermore I am grateful to Dr. Ken'ichi Ota and Dr. Akihiko Nakatsuka for illuminative and fruitful discussion, suggestions and encouragement, both scientific and not, throughout my grduate school days. They introduced me to the research field of this thesis.

I aslo thank Dr. S. Yu. Savrasov in Max-Plank-Institute for providing the original FP-LMTO programs package. I wish to express my gratitude to Dr. T. Nagai, Miss H. Otaki, Miss A. Kojima, Miss Y. Okuda and Miss J. Mimaki for their kind support for my research. Thanks are also due to all of the other members of research group under Professor F. Takei, Professor T. Sunamura, Professor K. Kawamura and Professor T. Yamanaka.

The study in the present thesis was supported by Research Fellowships of the Japan Society for the Promotion of Science (JSPS) for Young Scientists. The facilities for computation were equipped by this fund.

I am very indebted to many people that it is impossible to give here an explicit acknowledgement to all of them. Thus I apologize for any omission. Last but not least, I would like to thank my parents and my old friends for many encouragements.

Publications

"Molecular dynamics study of the crystal structure and phase relation of the GeO_2 polymorphs," Physics and Chemistry of Minerals (1998) 25:94-100.

"Molecular dynamics study of pressure-induced transformation of quartz-type GeO_2," Physics and Chemistry of Minerals (in press).

"Atomistic discussion of metastable states from viewpoints of MD simulations and experiments," Koubutsugaku-zasshi (in Japanese) (1998) 27:137-145.

"MD of high-pressure transition of GeO_2," Gekkan Chikyu (in Japanese) (1999) 21:116-121.

Bibliography

Akaogi M (1993) High-pressure transitions and thermodynamic properties of mantle minerals. J Mineral Soc Jpn 22:201-206 (in Japanese)

Akaogi M, Suzuki T, Kojima R, Honda T, Ito E (1993) In Special issue of the review of high pressure science and technology (in Japanese)

Allan NL, Mackrodt WC (1994) Density functional theory and interatomic potentials. Philos Mag B 5:871-878

Anders, Grevesse (1989) Abundances of the elements: Meteoritic and solar. Geochim Cosmochim Acta 53:197-214

Angel RJ, Chopelas A, Ross NL (1992) Stability of high-density clinoenstatite at upper-mantle pressures. Nature 358:322-324

Ashida T, Miyamoto Y, Kume S (1985) Heat capacity, compressibility and thermal expansion coefficient of ilmenite-type $MgGeO_3$. Phys Chem Minerals 12:129-131

Badro J, Barrat JL, Gillet P (1996) Numerical simulation of α-quartz under nonhydrostatic compression: memory glass and five-coordinated crystalline phases. Phys Rev Lett 76:772-775

Binggeli N, Chelikowsky JR, Wentzcovitch RM (1994) Simulating the amorphization of α-quartz under pressure. Phys Rev B 49:9336-9340

Blöchl PE, Jepsen O, Andersen OK (1994) Improved tetrahedron method for Brillouin-zone integrations. Phys Rev B 49:16233

Born M, Huang K (1954) Dynamical theory of crystal lattices. Oxford Univ Press, Oxford, pp 142

Brazhkin VV, Lyapin AG (1997) Comment on "Cauchy relation in dense H_2O ice VII." Phys Rev B 78:2493

Car R, Parrinello M (1985) Unified approach for molecular dynamics and density-functional theory. Phys Rev Lett 55:2471-2474

Carlsson AE (1990) Beyond pair potentials in elemental transition metals and semiconductors. Solid State Phys 43:1-91

Chang ZP, Graham EK (1977) Elastic properties of oxides in the NaCl-structure. J Phys Chem Solids 38:1355-1362

Chaplot SL, Sikka SK (1993) Molecular-dynamics simulation of pressure-induced crystalline-to-amorphous transition in some corner-linked polyhedral compounds. Phys Rev B 47:5710-5714

Chopelas (1996) The fluorescence sideband method for obtaining acoustic velocities at high compressions: Application to MgO and $MgAl_2O_4$. Phys Chem Minerals 23:25-37

Cormack AN, Catlow CR, Ling S (1989) Defects and mass transport in rutile-structured fluorides. II. Computer simulation. Phys Rev B 40:3278-3284

Dziewonski AM, Anderson OL (1981) Preliminary reference earth model. Phys Earth Planet Int 25:297-356

Demiralp E, Çağin T, Goddard III WA (1999) Morse stretch potential charge equilibrium force field for ceramics: Application to the quartz-stishovite phase transition and to silica glass. Phys Rev Lett 82:1708-1711

Dove MT, Heilmann IU, Kjems JK, Kurittu J, Pawley GS (1983) Neutron scattering of phonons in per-deuterated s-triazine. Phys Stat Sol 120b:173-181

Dove MT (1993) Introduction to lattice dynamics. Cambridge Univ Press, Cambridge, p. 115

Duffy TS, Hemley RJ, Mao HK (1995) Equation of state and shear strength at multimegabar pressures. Phys Rev Lett 74:1371-1374

Ercolessi F, Parrinello M, Tosatti E (1988) Simulation of gold in the glue model. Philos Mag A 58:213-226

Ewald PP (1921) Die Berechnung optischer und elektrostatischer Gitterpotentiale. Ann Phys 64:253-287

Fiquet G, Richet P, Montagnac G (1999) High-temperature thermal expansion of lime, periclase, corundum and spinel. Phys Chem Minerals 27:103-111

Gale JD, Catlow CRA, Mackrodt WC (1992) Periodic *ab initio* determination of interatomic potentials for alumina. Model Simul Mater Sci Eng 1:73-81

Gillet P, Badro J, Varrel B, McMillan PF (1995) High-pressure behavior in α-$AlPO_4$: amorphization and the memory-glass effect. Phys Rev B 51:11262-11269

Glinnemann J, King Jr HE, Shulz H, hahn T, Placa SJL Dacol F (1992) Crystal structures of the low-temperature quartz-type phases of SiO_2 and GeO_2 at elevated pressure. Z Kristallogr 198:177-212

Grimsditch M, Loubeyre P, Polian A (1986) Brillouin scattering and three-body forces in argon at high pressures. Phys Rev B 33:7192-7200

Grimsditch M, Brazhkin V, Balitskii D (1998) Elastic constants of α-GeO_2. J Appl Phys 83:3018-3020

Haines J, Léger JM, Chateau C, Bini R, Ulivi L (1998) Ferroelastic phase transition in rutile-type germanium dioxide at high pressure. Phys Rev B 58:R2909-R2912

Hemley RJ, Jephcoat AP, Mao HK, Ming LC, Manghnani MH (1988) Pressure-induced amorphization of crystalline silica. Nature 334:52-54

Hill VG, Chang LLY (1968) Hydrothermal investigation of GeO_2. Am Mineral 53:1744-1748

Hohenberg P, Kohn W (1964) In homogeneous electron gas. Phys Rev 136:B864-871

Hoover WG (1985) Canonical dynamics: Equilibrium phase-space distribution. Phys Rev A 31:1695-1697

Isaak DG, Anderson OL, Goto T (1989) Measured elastic moduli of single-crystal MgO up to 1800 K. Phys Chem Minerals 16:704-713

Itie JP, Polian A, Calas G, Petiau J, Fontaine A, Tolentino H (1989) Pressure-induced coordination changes in crystalline and vitreous GeO_2. Phys Rev Lett 63:398-401

Ito E, Matsui Y (1979) High-pressure transformations in silicates, germanates, and titanates with ABO_3 stoichiometry. Phys Chem Minerals 4:265-273

Jackson I (1976) Melting of the silica isotypes SiO_2, BeF_2 and GeO_2 at elevated pressures. Phys Earth and Planet Inter 13:218-231

Karki BB, Stixrude L, Clark SJ, Warren MC, Ackland GJ Crain J (1997) Structure and elasticity of MgO at high pressure. Am Mineral 82:51-60

Kamiya T (1996) Determination of interatomic potential by *ab initio* periodic calculation for MgO. Jpn J Appl Phys 35:3688-3694

Kawamura K (1996) Japan Chemistry Program Exchange (JCPE) Newsletter 7:71

Kawasaki S, Ohtaka O, Yamanaka T (1994) Structural change of GeO_2 under pressure. Phys Chem Minerals 20:531-535

Kawasaki S (1996) XAFS study of pressure-amorphized GeO_2. J Materials Sci Lett 15:1860-1862

Kingma KJ, Hemley RJ, Mao HK, Veblen DR (1993) New high-pressure transformation in α-quartz. Phys Rev Lett 70:3927-3930

Kirfel A, Hinze E, Will G (1978) The rhombohedral high pressure phase of $MgGeO_3$ (ilmenite): Synthesis and crystal structure analysis. Z Kristallogr 148:305-317

Kramer GJ, Farragher NP, van Beest BWH, van Santen RA (1991) Interatomic force fields for silicas, aluminophosphates, and zeolites: Derivation based on *ab initio* calculations. Phys Rev B 43:5068-5079

Kohn W, Sham LJ (1965) Self-consistent equations including exchange and correlation effects. Phys Rev 140:A1133-1138

Lassaga AC, Gibbs GV (1987) Applications of quantum mechanical potential surfaces to mineral physics calculations. Phys Chem Minerals 14:107-117

Leinenweber K, Wang Y, Yagi T, Yusa H (1994) An quenchable perovskite phase of $MgGeO_3$ and comparison with $MgSiO_3$ perovskite. Am Mineral 79:197-199

Liu LG, Bassett WA (1973) Changes of the crystal structure and the lattice parameter of SrO at high pressure. J Geophys Res 78:8470-8473

Loubeyre P, LeToullec R, Hausermann D, Hanfland M, Hemley RJ, Mao HK, Finger LW (1996) X-ray diffraction and equation of state of hydrogen at megabar pressures. Nature 383:702-704

MaKenzie DR (1975) Neutron and Raman study of the lattice dynamics of deuterated thiourea. J Phys C: Sol State Phys 8:2003-2010

Matsui M (1989) Molecular dynamics study of the structural and thermodynamic properties of MgO crystal with quantum correction. J Chem Phys 91:489-494

Matsui M (1998) Breathing shell model in molecular dynamics simulation: Application to MgO and CaO. J Chem Phys 91:3304-3309

Matsui Y, Kawamura K (1987) Computer-experimental synthesis of silica with α-PbO_2 structure. In: Manghnani MH, Syono Y (eds) High-Pressure Research. TERRAPUB (Tokyo), pp 305-311

Mehl MJ, Cohen RE (1988) Linearized augmented plane wave electronic structure calculations for MgO and CaO. J Geophys Res 93:8009-8022

Mehta A, Navrotsky A, Kumada N, Kinomura N (1993) Structural transition in $LiNbO_3$ and $NaNbO_3$. J Solid State Chem 102:213-225

Methfessel M, Rodriguez CO, Andersen OK (1989) Fast full-potential calculations with a converged basis of atom-centered linear muffin-tin orbitals: Structural and dynamic properties of silicon. Phys Rev B 40:2009-2012

Mizushima K, Yip S, Kaxiras E (1994) Ideal crystal stability and pressure-induced phase transition in silicon. Phys Rev B 50:14952-14959

Mortier WJ, Ghosh SK, Shankar S (1986) Electronegativity equalization method for the calculation of atomic charges in molecules. J Am Chem Soc 108:4315-4320

Newton MD, O'Keefe M, Gibbs GV (1980) *Ab initio* calculation of interatomic force constants in $H_6Si_2O_7$ and bulk modulus of α quartz and α cristbalite. Phys Chem Minerals 6:305-312

Nagai T (1995) doctral thesis.

Nose S (1984) A unified formulation of the constant temperature molecular dynamics methods. J Chem Phys 81:511-519

Oda H, Anderson OL, Isaak DG, Suzuki I (1992) Measurement of elastic properties of single-crystal CaO up to 1200 K. Phys Chem Minerals 19:96-105

Ozima M, Akimoto S (1983) Flux growth of single crystals of $MgGeO_3$ polymorphs (orthopyroxene, clinopyroxene, and ilmenite) and their phase relations and crystal structures. Am Mineral 68:1199-1205

Pandey RP, Jaffe JE, Kunz AB (1991) *Ab initio* band-structure calculations for alkaline-earth oxides and sulfides. Phys Rev B 43:9228-9237

Parr RG, Donnelly RA, Levy M, Palke WE (1978) Electronegativity: The density functional viewpoint. J Chem Phys 68:3801-3807

Parrinello M, Rahman A (1980) Crystal structure and pair potentials: A molecular-dynamics study. Phys Rev Lett 45:1196-1199

Parrinello M, Rahman A (1981) Polymorphic transitions in single crystals: A new molecular dynamics method. J Appl Phys 52:7182-7190

Pavone (1991) doctral thesis.

Perdew JP, Burke K, Ernzerhof M (1996) Generallized gradient approximation made simple. Phys Rev Lett 77:3865-3868

Perdew JP, Chevary JA, Vosko SH (1992) Atoms, molecules, solids, and surfaces: Applications of the generallized gradient approximation for exchange and correlation. Phys Rev B 46:6671-6687

Rao KVK, Naidu SVN, Iyengar L (1968) Thermal expansion of rutile-type GeO_2 by the X-ray method. J Am Ceram Soc 51:467-468

Rappé AK, Goddard III WA (1991) Charge equilibration for molecular dynamics simulations. J Phys Chem 95:3358-3363

Ray JR, Rahman A (1985) Statistical ensembles and molecular dynamics studies of anisotropic solids. II. J Chem Phys 82:4243-4247

Richet P, Mao HK, Bell PM (1988) Static compression and equation of state of CaO to 1.35 Mbar. J Geophys Res 93:15279-15288

Rick SW, Stuart SJ, Berne BJ (1994) Dynamical fluctuating charge force fields: Application to liquid water. J Chem Phys 101:6141-6156

Ringwood AE (1991) Phase transformations and their bearing on the constitution and dynamics of the mantle. Geochim Cosmochim Acta 55:2083-2110

Ross NL, Navrotsky A (1988) Study of the $MgGeO_3$ polymorphs (orthopyroxene, clinopyroxene, and ilmenite structures) by calorimetry, spectroscopy, and phase equibria. Am Mineral 73:1355-1365

Sanderson RT (1951) An interpretation of bond length and a classification of bonds. Science 114:670-672

Sinogeikin SV, Bass JD (1999) Single-crystal elasticity of MgO at high pressure. Phys Rev B 59:14141-14144

Smith GS, Isaacs PB (1964) The crystal structure of quartz-like GeO_2. Acta Crystallogr 17:842-846

Sowa H (1988) The oxygen packings of low-quartz and ReO_3 under high pressure. Z Kristallogr 184:257-268

Tanimoto T, Anderson DL (1984) Mapping convection in the mantle. Geophys Res Lett 11:287-290

Tse JS, Klug DD (1991) Mechanical instability of α-quartz: a molecular-dynamics study. Phys Rev Lett 67:3559-3562

Tsuneyuki S, Matsui Y, Aoki H, Tsukada M (1989) New pressure-induced structural transformations in silica obtained by computer simulation. Nature 339:209-211

Tsuchida Y, Yagi T (1989) A new, post-stishovite high-pressure polymorph of silica. Nature 340:217-220

Tsuchiya T, Yamanaka T, Matsui M (1998) Molecular dynamics study of the crystal structure and phase relation of the GeO_2 polymorphs. Phys Chem Minerals 25:94-100

Tsuchiya T, Yamanaka T, Matsui M (1999) Molecular dynamics study of pressure-induced transformation of quartz-type GeO_2. Phys Chem Minerals (in press)

Upadhyay SP, Kumar M (1995) Thermal expansion and compression of alkaline earth oxides and cesium halides at high temperature and high pressure. Phys Stat Sol B 191:299-305

Verlet L (1967) Computer "experiments" in classical fluids. I. Thermodynamical properties of Lennard-Jones Molecules. Phys Rev 159:98-103

Wang H, Simmons G (1973) Elasticity of some mantle crystal structures. 2. Rutile GeO_2. J Geophys Res 78:1262-1273

Watson JW, Parker SC (1995) Quartz amorphization: a dynamical instability. Philos Mag Lett 71:59-64

Weyrich KH (1988) Full-potential linear muffin-tin-orbital method. Phys. Rev. B 37:10269-10282

Wolf GH, Wang S, Herbst CA, Durben DJ (1992) Pressure induced collapse of the tetrahedral framework in crystalline and amorphous GeO_2 In: Syono Y, Manghnani MH (eds) High-Pressure Research. TERRAPUB (Tokyo), pp 503-517

Yagi T, Jamieson JC, Moore PB (1979) Polymorphism in MnF_2 (rutile type) at high pressures. J Geophys Res 84:1113-1115

Yamanaka T, Hirano M, Takéuchi Y (1985) A high temperature transition in $MgGeO_3$ from clinopyroxene ($C2/c$) type to orthopyroxene ($Pbca$) type. Am Mineral 70:365-374

Yamanaka T, Nagai T, Tsuchiya T (1997) Mechanism of pressure-induced amorphization. Z Kristallogr 212:401-410

Yamanaka T, Shibata T, Kawasaki S, Kume S (1992) Pressure induced amorphization of hexagonal GeO_2. In: Syono Y, Manghnani MH (eds) High-Pressure Research. TERRAPUB (Tokyo), pp 493-501

Yin MT, Cohen ML (1980) Microscopic theory of the phase transformation and lattice dynamics of Si. Phys Rev Lett 45:1004-1007